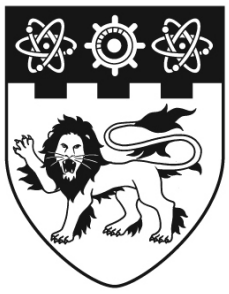

NANYANG TECHNOLOGICAL UNIVERSITY

Morphologies, Structures and Properties of Electrospun PVDF-based Materials

Yee Wu-Aik

School of Materials Science and Engineering

2012

Morphologies, Structures and Properties of Electrospun PVDF-based Materials

Yee Wu-Aik

School of Materials Science and Engineering

A thesis submitted to the Nanyang Technological University in fulfillment of the requirement for the degree of

Doctor of Philosophy

2012

Acknowledgements

First and foremost, the author would like to thank his academic supervisor, Associate Professor Lu Xuehong (NTU), for the advice, guidance and support that she has continuously provided throughout this graduate work. The author would also like to thank his project co-supervisor Dr Liu Ye (IMRE) and to Dr Masaya Kotaki (Kyoto Insitute of Technology) for providing the knowledge and know-how on research and development.

The author would also like to express his gratitude to Ms Joan Toh, Dr Herman Teo, Dr Ricky Chua, Ms Ming Liu, Dr Peng Tao Jia, Mr Bai Yu, Dr Peisi Keg, Mr Junyan Lek, Mr Junhua Kong, Dr Liping Yang, Ms Silei Phua, Dr Jia Wei, Mr Alok Chaurasia and Dr Ahn Chien Nyguen for the constructive discussions, emotional and mental support throughout the course of this research work. The author would also like to extend his thanks to the Institute of Materials Science and Engineering (IMRE) for the use of its facilities and to the staff of Organic Materials Service Lab (NTU), for the kind help and support rendered.

Lastly, the author would like to thank his family, especially his wife, Ms Andrea Chin Yimei, for their continuous support and encouragement. The author will also like to delicate this work to his elder son, Julian as well as his younger daughter, Jillian, for providing him the motivation to finish this thesis.

Table of Contents

List of Figures & Tables

Figure

Table

List of Abbreviations & Acronyms

Poly(vinylidene diflufloride)	PVDF
Trans	T
Gauche	G
Alpha	α
Beta	β
Gamma	γ
Sigma	δ
Trifluoroethylene	TrFE
Tetrafluoroethylene	TeFE
Hexafluoropropylene	HFP
Polyethylene	PE
Polytetrafluoroethylene	PTFE
Carbon nanotubes	CNTs
Single-walled Carbon Nanotubes (Hydrolyzed)	SWCNTs
Multi-walled Carbon Nanotubes (Hydrolyzed)	MWCNTs
Extended-chain crystals	ECCs
Tetraethyl orthosilicate	TEOS

Two dimensional	2D
Dimethylformamide	DMF
Indium tin oxide	ITO
Scanning Electron Microscope	SEM
Field emission scanning electron microscope	FESEM
Wide angle x-ray diffraction	WAXD
Attenuated fourier transform infrared spectroscopy	AT-FTIR
Attenuated Total Reflection	ATR
Differential scanning calorimetry	DSC
Piezoresponse Force Microscopy	PFM
Transmission electron microscopy	TEM
Esterified single-walled carbon nanotubes	e-SWCNT
Polystyrene	PS
Thermogravimetric analysis	TGA
Supercritical fluid	SCF
Supercritical carbon dioxide	$SCCO_2$
Glass Transition Temperature	T_g
Carbon Dioxide	CO_2
1-Butyl-3-methylimidazolium hexafluorophosphate	$[BMIM]PF_6$
Ionic liquid	IL

Abstract

Electrospinning is a technique that can be used to produce nanofibers, and it is discovered that it is able to enhance the *β*-phase of poly(vinylidene difluoride), PVDF. Owing to its highest polarization per unit cell, the *β*-phase of PVDF exhibits the maximum electroactive properties, i.e., ferro-, pyro- and piezo-electric properties, in comparison with other phases of PVDF. Although researches have shown that the *β*-phase of PVDF can be improved by (1) alteration of the chemical structure, (2) usage of additives, (3) application of a stretching force and (4) the use of high temperature and pressure treatments, the synergistic effects among (2), (3) and (4) on polymorphism behaviors and electro-active of PVDF have not been studied. Thus, this work was undertaken to study polymorphism behaviors, morphologies and electro-active properties of electrospun poly(vinylidene fluoride-co-hexafluoropropene) (P(VDF-HFP)) nanofibers and P(VDF-HFP)/carbon nanotube (CNT) composite nanofibers, which experienced high extensional forces in the electrospinning and collection processes, as well as high temperature and pressure treatments in supercritical carbon dioxide ($SCCO_2$).

Firstly, a modified rotating disk collector is used in electrospinning to provide stronger stretching force to the electrospun P(VDF-HFP) nanofibers. By attaching seperate, parallel electrodes onto a rotating disk collector, well aligned nanofibers of P(VDF-HFP)) and P(VDF-HFP)/CNT nanocomposites can be directly deposited onto flat substrates forming uniform and compact nanofibrous mats. The attachment alters the electric-field distribution on the rotating disk while providing an additional stretching force during the fanning of the fibers. This additional stretching force exerted by the modified rotating disk prevents the relaxation of the polymer chains during solvent evaporation, and hence results in the formation of extended-chain *β*-chain crystallites with a slightly reduced inter-chain distance, as evidenced by wide angle X-ray diffraction (WAXD) patterns and Fourier transform infrared (FTIR) spectra of the samples.

Further work was conducted to improve the *β*-phase content of P(VDF-HFP) by the addition of CNTs and to understand the synergistic effect of the stretching force and the interfacial

interactions of the CNTs with P(VDF-HFP) on the crystallization behavior of the composite nanofibers. With low concentrations of single-walled carbon nanotubers (SWCNTs), it is shown that the interfacial interactions and the extensional force experienced by the nanofibers during the fiber collection can work synergistically to induce the formation of extended-chain *β*-chain crystallites extensively. In contrast, multi-walled carbon nanotubers (MWCNTs) could not be well-aligned along the nanofiber axis, which leads to lower degree of crystal orientation, and the extended-chain β-phase is not significantly promoted. Additionally, it is also found that hydroxyl groups on the CNTs' surface help to enhance the interfacial interactions, facilitating the synergistic enhancement of the extended-chain *β*-phase crystallites.

To further enhance the electro-active properties of the electrospun P(VDF-HFP) membranes, a novel post-treatment technique utilizing $SCCO_2$ was explored. The treatment leads to further enhancement of the extended-chain *β*-form crystallites owing to the high pressure applied on the well aligned polymer chains. It also leads to the formation of inter-fiber junctions, resulting in a mark improvement in mechanical properties of the electrospun membranes and hence allowed the practical demonstration of their functionality as an ionic liquid host for electrochemical applications and as a piezoelectric force sensor. Strain sensors were fabricated by sandwiching aligned electrospun P(VDF-HFP)/SWCNT fibrous membranes between electrodes with all layers bonded through the use of $SCCO_2$ treatment. The measured piezoelectric response from the electrospun P(VDF-HFP)/SWCNT membrane shows a impressive improvement of approximately ten times, as compared to the electrospun P(VDF-HFP) counterpart.

Overall, the results from this work suggest that the additional stretching force provided by the modified rotation disk collector, the incorporation of surface-hydroxylated SWCNTs and post $SCCO_2$ treatment can work synergistically to promote the formation of well oriented extended-chain β-phase crystallites in P(VDF-HFP). The alignment and post treatment can also make the nanofibrous mats more compact, enabling the demonstration of the electro-active properties of the electrospun nanofibers.

1 Introduction

1.1 Background

Polyvinylidene difluoride (PVDF) and its co-polymers are attractive materials for many functional applications owing to its significant electroactive properties, i.e. ferroelectricity, piezoelectricity and pyroelectricity, as well as its light weight, flexibility and good electrochemical stability. Depending on processing conditions, PVDF can exhibit at least four distinct polymorphs, which involve three different chain conformations, namely (1) slightly twisted all-*trans* zigzag (*TTTT*, *T* denotes *trans*) for β phase, (2) *TGTG'* (*G* denotes *gauche*) for α and δ (α_p) phases and (3) *TTTGTTTG'* for γ phase [1,2]. When PVDF chains are packed into crystal lattices, their dipoles are either additive, which leads to a net dipole as in β, γ and δ phases, or subtractive, resulting in no net dipole as in α phase. Among the three polar polymorphs, the β form has the largest spontaneous polarization per unit cell and exhibits the highest piezo- and ferroelectric properties [1]. In order to maximize the β form, numerous approaches have been attempted by researchers, which can be summarized into four large categories: (1) modification of the chemical structures, (2) application of stretching forces, (3) incorporation of additives and (4) the use of high temperature and pressure treatments.

A key requirement for PVDF-based piezoelectric and ferroelectric thin film devices is that the active material should have a high β-phase content. In addition, in such devices, the direction of the polarizing electric field is normally perpendicular to the film surface. If the *c*-axis of the β crystallites are oriented parallel to the film surface, the dipoles of the all-*trans* conformers will be

in the *b*-axis direction of the orthorhombic lattice, which can be easily aligned along the normal of the thin film by the applied electric field. Relatively high β-phase contents and preferred crystal orientation in PVDF can be achieved via processes involving stretching forces long the chain direction, such as melt spinning [3], extrusion [4] and mechanical drawing [5] and other processes [6-8]. An alternative route is electrospinning. Electrospinning has received great attention in the past few years owing to its simplicity, low cost and versatility for fabrication of nanofibers. For PVDF and its copolymers, this technique can help to promote all *trans*-conformers and hence enhance the formation of the *β*-phase while promoting the formation of oriented crystallites [9-11]. Such crystal orientation and *β*-phase enhancement are extremely beneficial in improving the electroactive properties of PVDF and its co-polymers, which may lead to light-weight novel devices based on PVDF nanofibers.

In electrospinning process, not only the electrostatic force exerted on polymer jets help to stretch the polymer chains, rotating collection apparatus can also impart a stretching force due to the centripetal force created during the rotation [12-14]. Although PVDF-based nanofibers have been fabricated using different rotating apparatus, the influences of the collecting processes on (1) the crystalline structures, especially polymorphism behavior, of PVDF-based polymers, (2) the crystal orientation of the polymers and (3) the electroactive properties of the polymers have yet been systematically studied. More importantly, to further enhance the stretching force, there is a need to design a modified rotating collector that allows the nanofibers to experience a stronger extensional force during the collection. Our hypothesis is that with the use of a modified rotating collector that can combine electrostatic force with mechanical force, the β-phase contents and preferred crystal orientation in PVDF-based polymers may be further enhanced, leading to improved electroactive properties. It may even effectively restrict the relaxation of

polymer chains during the collection process and promote the formation of extended-chain *β*-phase crystallites in the electrospun nanofibers.

Although there are many reports detailing the effects of additives on polymorphism behaviors of PVDF-based polymers, such as the enhancement of *β*-phase of PVDF by the addition of hydrated salts [43], organoclay [44] and carbon nanotubes (CNTs) [17,18], the impact of the additives on the crystallization of electrospun PVDF, especially the synergistic effects between the stretching force applied and the additive-polymer interactions are not well investigated. Among various additives, CNTs are of particular interest because of their high aspect ratios. The hypothesis is that the stretching force experienced by the electrospun nanofibers may work synergistically with the chemical/physical interactions between the CNTs and PVDF chains to alter the polymorphism behaviors of PVDF-based polymers since the orientation of the CNTs is also affected by the strong stretching force applied owing to their high aspect ratios. The synergistic effect may lead to further enhancement of polar phases in the electrospun nanofibers.

Owing to the porous nature of the as-spun electrospun nanofibrous mats, these mats need suitable post-treatments to improve their compactness before they can be readily used in fabrication of ferroelectric and piezoelectric devices. The collection of electrospun nanofibers in aligned manner using rotating collectors can help to improve the compactness of the nanofibrous mats to some extent. Although a simple hot pressing process can be employed to improve compactness of the electrospun nanofibrous films significantly [114], the high temperatures required for effective compressing would convert some of the *β*-phase crystallites into the *α*-phase ones as the latter is the more thermodynamically stable phase. Some studies on high-pressure crystallization of PVDF-based polymers at high temperatures have shown that the high

pressure applied can lead to the formation of extended-chain β-phase crystallites [51]. This strategy may be applied to electrospun PVDF membranes to improve the crystal structures and morphology of the aligned electrospun PVDF nanofibrous mats simultaneously. A good alternative to conventional high-pressure crystallization, which requires expensive equipment, is the crystallization in super critical carbon dioxide ($SCCO_2$). We hypothesized that the post treatment of aligned electrospun PVDF nanofibrous membrane with $SCCO_2$ at moderate pressures may enhance extended-chain β-phase crystallites formed in well aligned electrospun PVDF nanofibers as well as the compactness of the mats, enabling the demonstration of the electro-active properties of the electrospun PVDF nanofibers.

The effects of modification of chemical structures of PVDF, such as copolymerization, on polymorphism behaviors of PVDF-based polymers have been extensively studied in the past few decades. It is found that PVDF homopolymer can exhibit the highest crystallinity, while PVDF copolymers such as poly(vinylidene fluoride-co-trifluroethylene) (P(VDF-TrFE)) and poly(vinylidene fluoride-co-hexafluoropropene) (P(VDF-HFP)) have a higher tendency to crystallize into β phase owing to the steric hindrance induced by larger F atoms that made *trans* conformation to be favored over the *gauche* conformation [1], although their crystalinities are lower. In this work, P(VDF-HFP), instead of PVDF homopolymer, is chosen as the main material system because of its ease of processing in solution form as compared with PVDF, while a low HFP content (10 mol.%) is chosen to ensure a relatively high crystallinity can be achieved, allowing us to effectively study the crystallization behaviors of the polymer. More importantly, the use of the same polymer throughout this work allows us to have a better understanding of the effects of the other three parameters, i.e., stretching force, interactions with

CNTs and $SCCO_2$ treatments, on the polymorphism behaviors and morphology of the electrospun nanofibrous mats.

1.2 Objectives

The major motivation for this study stems from the increasing demand for the use of nano-structured materials to improve the performance of PVDF-based ferroelectric and piezoelectric devices**.** A good understanding on how the P(VDF-HFP) copolymer crystallizes under a set of external stimuli induced by electrospinning, the collection process and post treatment, and internal stimuli given by the additives, as well as their interplays would provide useful information for design of novel devices with improved performance. Thus the major objectives of my PhD study are to realize the functionality of electrospun P(VDF-HFP) through manipulation of its morphology and crystalline structures, and more importantly, to understand the underlying mechanisms, especially the synergistic effects between the external and internal stimuli. The aforementioned hypotheses will be investigated and verified. Functionalities of the electrospun PVDF will be demonstrated but they are not the focuses of the work.

1.3 Organization of Thesis

The thesis will be presented in the following order. A literature review on the polymorphism of PVDF and its co-polymers, how their molecular structures influence their polymorphism behaviors, techniques used to increase their β-phase content and the theory of electrospinning will be presented in Chapter 2. The modification of the rotating disk collector, its impact on the polymorphism of P(VDF-HFP) and demonstration of the switching of dipoles within the

electrospun fibers will be presented in Chapter 3. In Chapter 4, the effects of the addition of CNTs on structures and morphology of the P(VDF-HFP)/CNTs electrospun nanocomposite fibers collected using the modified rotating disk collector are discussed. A novel approach utilizing supercritical carbon dioxide to further process the nanofibrous thin films and its effects on crystalline structures and morphology will be discussed in chapter 5, and the testing of the piezoelectric properties of these films will also be presented in the same chapter. Chapter 6 is a summary of all the significant findings, and the recommendations for future work will be presented in Chapter 7.

2 Literature Review

In this chapter, the structures and electroactive properties of the materials, poly(vinylidene difluoride) (PVDF) and its co-polymers that are the focus of this study, will be introduced. As PVDF can exhibit different polymorphism behaviors under different conditions, the structures induced by various processing/treatment conditions and additives, as well as the underlying principles, will be discussed. As the major processing technique used in this work is electrospinning, the theories of electrospinning, its influences on the polymorphism of PVDF and potential applications of PVDF electrospun nanofibers and membranes are also discussed.

2.1 Conformations of PVDF

PVDF, a commercially available polymer, has drawn great attention in recent years due to its many attractive properties such as flexibility, light weight, processibility and most important of all, its electroactive properties including ferro-, pyro- and piezoelectricity. Although many other polymers like the co-polymers of PVDF with trifluoroethylene (TrFE), tetrafluoroethylene (TeFE) or hexafluoropropylene (HFP) [1], odd repeating units of nylon like nylon 5, 7 or 11 [22,23], poly vinyl chloride (PVC) [24], cellulose [25] and even liquid crystals [26] have been shown to possess both ferro- and piezo-electricity properties, PVDF has been found to exhibit one of the highest electroactive responses among semi-crystalline polymers. However, PVDF exhibits

many polymorphs. The reason lies behind its simplistic structure, $-CH_2-CF_2-$, which lies between polyethylene (PE) $-CH_2-CH_2-$, and polytetrafluoroethylene (PTFE) $-CF_2-CF_2-$. These allow PVDF to be highly flexible (close to PE) while having stereochemical constraints (as in PTFE), resulting in PVDF to be able to crystallize into four different polymorphs [1,19,20,27]. In the case of PTFE, due to stereochemical repulsion between the neighbouring $-CF_2-$ along the main chain, it takes a helical conformation that deviates slightly (c.a. 169°) from the *trans*-rotational state of 180° of PE [1]. This makes PTFE more rigid than PE, where the all-*trans* zig zag conformations are observed predominantly in the crystalline state [28] while the *gauche* conformation can also appear partially at the temperature close to the melting point as it is thermodynamically stable as well [1]. In PVDF, the $–CH_2-$ group plays a diluting role due to its presence between two $–CF_2-$ groups, allowing both the *trans* and *gauche* conformations to co-exist in a stable state [1]. This results in PVDF (and its co-polymers) to crystallize into different forms/phases, comprising of a variety of molecular conformations. These molecular conformations when packed in a unit cell, determines the electroactive properties.

The known crystal forms of PVDF mainly involve three different chain conformations, namely *TGTG'*, *TTTT*, and *TTTGTTTG',* each possessing a net dipole moment perpendicular to the polymer chain [1,19,20]. These chain conformations can pack in a total of four ways in a unit cell, which has been identified as β-phase (Form I), α-phase (Form II), δ-phase (Form II_p) and γ-phase (Form IV), shown in Figure 2.1 [1,19,20,21]. The manner in which they pack in the unit cell can cause addition or cancellation of dipoles from the individual molecular chains in the unit cell, resulting in a stronger or no net dipole in the crystal [1,29]. The polar forms of PVDF possess distinct electroactive properties while the non-polar forms do not.

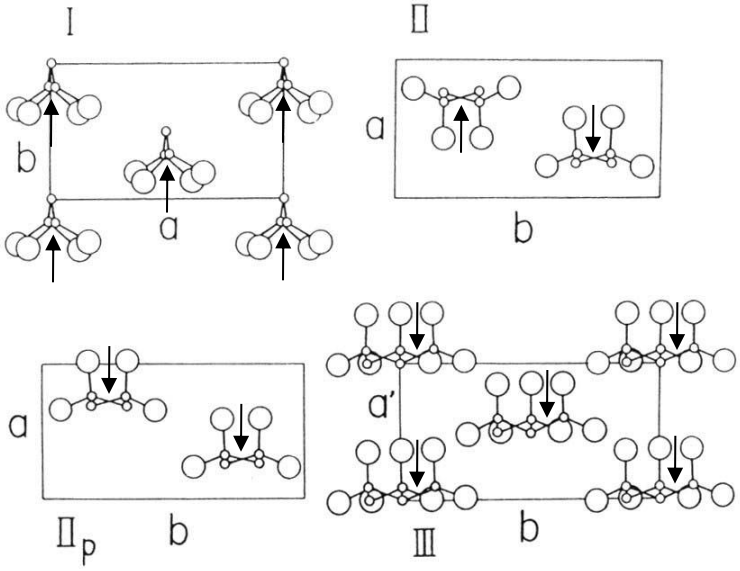

Figure 2.1 Projections of carbon (small circles) and fluorine (big circles) atoms of PVDF onto the ab planes of the known crystal forms of PVDF [20]. The arrow depicts the direction of the polar moment caused by the conformations of the polymer chain of PVDF.

It can be clearly seen from Figure 2.1 that α-phase is non-polar while the rest of the other forms of PVDF are polar in nature. Under normal processing conditions of PVDF where it is cooled from the melt, the α-phase is obtained because it is the most thermodynamically stable phase [1]. In the α-phase, the chain adopts the *TGTG'* conformation and pack in an anti-parallel array, resulting in the dipoles that exist to cancel out each other. This causes the α-phase to lose its net polarity in the crystal, as shown in Figure 2.2b and d.

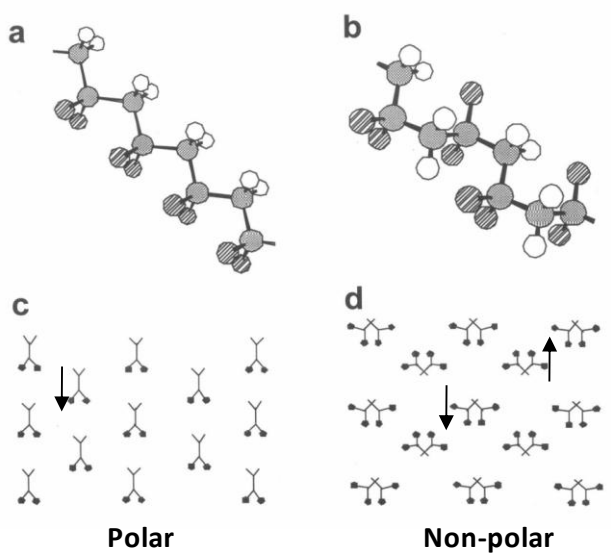

Figure 2.2 2D Schematic representation of the (a) TTTT conformation of the β-phase, (b) TGTG' conformation of the α-phase. The crystal structures of the (c) β-phase and (d) α-phase of PVDF are also shown; Carbon atoms are grey, hydrogen atoms are white and fluorine atoms are striped [19].

The δ-phase of PVDF, which is polar, can be obtained by subjecting the polymer to a strong electric field on the order of 1.2 MV/cm at room temperature, which converts the α-phase to the δ-phase [20,30,31]. The γ-phase, another polar phase of PVDF, can be obtained by high temperature crystallization or annealing the α-phase at high temperatures [20]. During the study of the solid state transformation of the α-phase to the γ-phase, another polar crystal form was discovered and was named the ε-phase. However, the ε-phase was only present in small amounts and extremely difficult to retain [32], making this phase insignificant in the contribution to PVDF's electroactive properties. Although the δ-phase and γ-phase are polar, due to its conformation, the dipole moment associated with these 2 phases still experiences slight cancellation of the dipoles within

the molecular chains resulting in a diminished net dipole within the crystal. These will result in decreaseded electroactivity in PVDF when stimulated. Out of the three polar phase of PVDF, only the *β*-phase will not pose this problem due to its all-*trans* zig-zag conformation as shown in Figure 2.2a and c, resulting in the ability of the polarization to be switched between opposite but energetically equivalent directions along the ***b***-axis of the unit cell (Figure 2.2 Form I unit cell). This allows the *β*-phase to exhibit the strongest electroactive response when stimulated, as compared to the other polymorphs of PVDF. With this in mind, the next section will look at how the *β*-phase of PVDF can be promoted by different processing techniques involving different chemical or physical methods.

2.2 Methods to promote the *β*-phase of PVDF

As the *β*-phase of PVDF exhibits the strongest electroactivity among all the polymorphs, many methods that can help to promote this phase have been discovered, which are summarized in Figure 2.3.

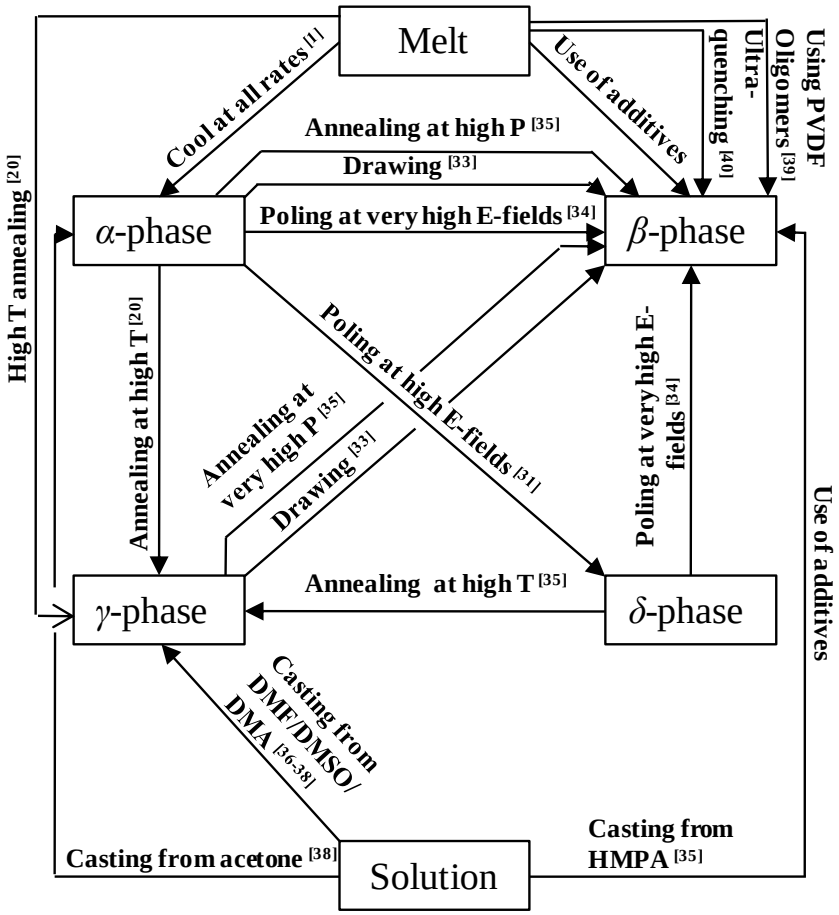

Figure 2.3 Interrelations among the four polymorphs of PVDF by processing. P denotes Pressure and T denotes Temperature. Adapted and modified from ref. [20].

Although many chemical or physical methods can be utilized to enhance the β-phase of PVDF, four techniques have been discovered to consistently provide high β-phase content in PVDF and these techniques will be discussed in detail in the following sections.

2.2.1 Copolymerization

Due to the difficulty in making PVDF to fully crystallize into the pure *β*-phase as well as the processing difficulties experienced while making PVDF thin films as a result of its high crystallinity, researchers have looked into co-polymerizing PVDF with TrFE (-CHF-CF_2-), TeFE (-CF_2-CF_2-) and HFP (-CF_2-CF(CF_3)-) respectively. These monomer units are randomly added into the main chain of PVDF and thus may be added in the reverse fashion unavoidably. These reverse monomers thus serve as defects, resulting in lower melting points as well as lower ferroelectric transition temperatures [1]. However, distinct advantages can be obtained with the addition of each monomer.

Monomers of TrFE and TeFE were able to draw the attention of researchers because when these monomers are co-polymerized with PVDF at significant concentrations, the resulting co-polymer was able to crystallize directly into the polar all-*trans* conformation, similar to the *β*-phase of PVDF, as shown in Figure 2.2a and c, without the need of mechanical drawing or other processes. As the fluorine atom is significantly larger than the hydrogen, when the monomer is inserted into the main chain, sterical hindrance will occur. This will result in the *trans* conformation to be favored over the *gauche* conformation. A slightly larger unit cell as compared to pure PVDF will then occur within the crystals resulting in weaker average dipole moment. The cause of the weaker dipole moment is due to the replacement of some hydrogen atoms by the fluorine atoms, reducing the availability of the dipole moment forming between hydrogen and fluorine. This is also the reason for the decreased electroactivity of the co-polymers in the following order: PVDF-TrFE > PVDF-TeFE > PVDF-HFP. However, when low concentrations of monomers are polymerized with PVDF, crystallization behavior of the copolymers of PVDF will not be significantly affected (mainly *α*-phase when cooled from the

melt) but at low concentrations, they will act as defects and will decrease the crystallinity slightly, resulting in improved processibility. This type of copolymers of PVDF (PVDF-HFP where the concentration of HFP is 10 mol. %) is the main material used in this thesis due to the increased solubility, allowing the polymer to be processed easily. However, reduced crystallinity decreases the electroactivity of the copolymers of PVDF. Due to the ability of the copolymers to directly crystallize into the all *trans* β-phase directly from the melt, even with reduced crystallinity and electroactivity, it still offer a distinct advantage over pure PVDF due to the difficulty involved in making PVDF to crystallize into the β-form without cumbersome additives or post-processing. However, the diminished dipole moment of the co-polymers as compared to PVDF drove researchers to try alternative methods to enhance the β-phase of PVDF without sacrificing both crystallinity and the molecular dipole moment significantly. One of the easiest is through the use of additives.

2.2.2 Use of additives

In recent years, researchers have upped the ante in the research on PVDF. Through careful selection of additives summarized in Table 1, the β-phase of PVDF can be enhanced extensively, thus avoiding troublesome steps like cold/hot drawing, the use of high pressure and temperature or the use of very high voltages (500 MV/m) [41] to induce the β-phase has been realized. However, films with extensive β-phase content still require electrical poling to re-orientate the dipoles into a general direction to maximize its electroactive properties [42] as the dipoles in the as-formed β-phase are random in nature. The same applies to mechanically drawn films or films manufactured using the techniques outlined in the summary in Figure 2.3 that provide high β-phase content.

Table 2.1
Additives that can induce the *β*-Phase in PVDF

No.	Method	Comments	References
1	Addition of hydrated salts into PVDF polymer solutions prior to casting.	Able to produce films of high β- phase content.	M. Benz et. al. [43]
2	Addition of modified clay into PVDF polymer solutions prior to melt intercalation.	PVDF with nanocomposites crystallized into the *β*-phase.	L. Priya et. al. [44]
3	Blending with Carbon Nanotubes	Able to promote the *β*-phase in PVDF	N. Levi et. al. [18]

Through the use of hydrated salts as an additive to control the water content in solution casted PVDF, Benz *et al* was the first to reproducibly form high *β*-phase content thin films [43]. The author suggested that hydrogen bonding between the water molecules and the polar C-F in the polymer chains was responsible for the *β*-phase enhancement and the result was again reproduced by Yee *et al* [10] and He *et al* [45]. He *et al* was also able to demonstrate that such films produced using this technique can exhibit large remnant polarization and piezoelectric constants due to the significant *β*-phase enhancement. However, to maximize the other electroactive properties of the PVDF film, the retained water in the system must be removed as it may deteriorate its electrical properties [45].

The use of organo-modified clay has also been shown to enhance the *β*-phase of PVDF significantly but at the expense of crystallinity due to the confinement effect on the molecular chains as the clay intercalates [44,46,47]. It is suggested that the strong interaction of PVDF molecular chains and the surface of the charged organo-modified clays resulted in the

enhancement. The intercalated clay also prevents relaxation of the PVDF molecular chains. The addition of carbon nanotubes (CNTs), both single (SWCNTs) and multi-walled (MWCNTs) can bring about significant enhancement of the *β*-phase in PVDF when used as an additive and was first reported by Levi *et al* [18]. Studies [18,48,49] have shown that the interaction between the CNTs' surface and the molecular chains of PVDF is the cause of such an enhancement but fall short of identifying the exact type of interactions that exist between the CNTs' surface and PVDF molecular chains. It is again important to take note that the *β*-phase formed through the use of additives has random dipoles and poling is required to maximize the electroactive properties of PVDF.

However, how and why such additives can produce such remarkable improvements is still not very well understood. In addition, the use of additives may alter other physical properties of the resulting composite material.

2.2.3 Usage of high pressure and temperature

In 1978, Matsushige *et al* first discovered that thick lamellar crystals of extended chain *β*-phase crystals (*β*-ECCs) can be grown in PVDF under high pressure (3500 kg/cm^2) and temperature (315°C) [35]. However, the reasons for its growth were not well understood until a phase diagram (Figure 2.4) was proposed by Hattori *et al* [50]. With this phase diagram, a consistent technique to obtain such *β*-ECCs was suggested.

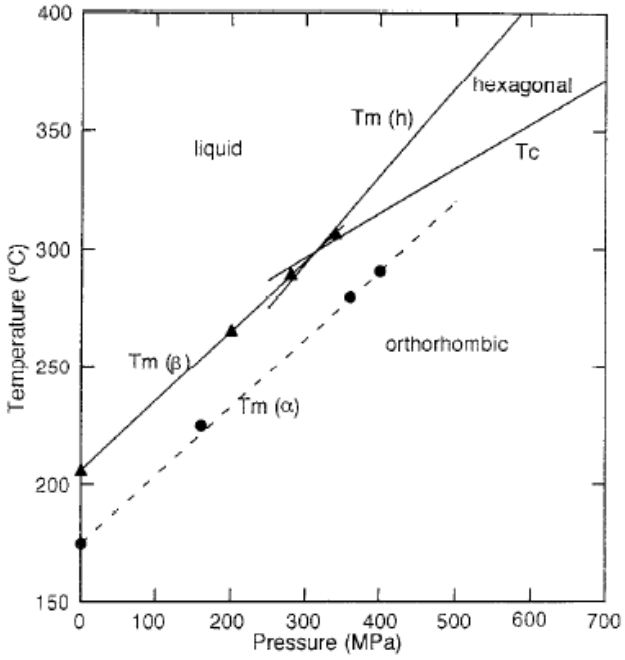

Figure 2.4 The P-T phase diagram for thick lamellar β-phase crystals of PVDF. The dotted line denotes the melting curve (Tm) of the the α-phase [41].

It was suggested that by heating PVDF to the melt state (240°C -300°C) at high pressures (~5000 kg/cm^2 or 500 MPa) below the triple point where the hexagonal phase can exist in a metastable state, thick lamellar of *β*-ECCs can be formed from the melt. Its crystallization process is similar to the crystallization of the co-polymers of PVDF-TrFE from the melt where the hexagonal metastable state can exist at atmospheric conditions [51]. Such crystal morphology has been shown to exhibit stronger electroactive responses as compared to stretched and poled PVDF [50] due to many conformational defects introduced during the stretching process and the small crystal sizes. It is important to take note that such films made at high pressure and temperature are required to be poled by applying an electric field on the order of 30 MV/cm [1] to align the dipoles in PVDF so as to maximize its electroactive properties. However, the

complexity of crystallizing PVDF under such high pressures from the melt has become its Achilles' heel in providing high *β*-content films for electroactive applications. Thus, the copolymers of PVDF, which can crystallize directly from the melt or solution into high *β*-phase content films, can provide a much easier alternative but at the expense of a diminished dipole moment. Thus, in the industry, actuators or piezoelectric sensors based on PVDF are still mainly based on one processing technique which has been extensively studied over the years to provide high *β*-phase content films. The technique is mechanical stretching and poling.

2.2.4 Mechanical stretching and electrical poling of PVDF

The *β*-phase of PVDF can be easily obtained through mechanical drawing (3-7 times its original dimension) to allow the molecular chains to unwind from its original conformation (either *α-, γ-, or δ*-phases) to the all-*trans* conformation [33]. Mechanical drawing also causes the breakdown of spherulites and allows the orientation of the molecular chains in the direction of the force applied. Additionally, electrical poling can be applied to align the dipoles of the samples simultaneously. By just applying a very high electrical field alone, the *α*- to *β*-phase transition can also be observed [52]. In order to maximize the efficiency of these two processes, high electrical fields are now being applied while stretching at elevated temperatures, to ensure the maximum amount of *β*-phase that can be obtained [53,54]. The combination of these two processes also gives rise to better crystal morphology as well as increase crystallinity [8].

In recent years, a technique called electrospinning, which produces nanofibers has been discovered to provide in-situ stretching as well as electrical poling at the same time to the as-formed nanofibers of PVDF. The process is able to enhance the *β*-phase of PVDF while forming

preferentially aligned crystals in the fiber direction [10]. The formation of such preferentially aligned β-crystals can prove to be beneficial for electroactive applications.

2.3 Electrospinning

Electrospinning has been established as a very effective method in producing fibers in the nano-dimensions from polymer solutions or melts. Unlike various methods that generate one-dimensional nano-structures [55,56], electrospinning is one of the easiest techniques to obtain long nanofibers which are uniform in dimensions, allowing a diverse composition or materials to be electrospun [12,57,58]. Electrospinning can also produce membranes of extremely high surface-to-volume ratios. The electrospinning set-up can be assembled easily, as shown in Figure 2.5. The setup consists mainly of three main components, namely a high voltage power supply, a spinneret with controllable feed rate and finally, a metallic collector which is grounded. The high voltage supply normally supplies direct voltage into the polymer solution in the spinneret but the use of an alternating voltage as the power source is also feasible [59]. The polymer solution is normally fed into the spinneret (metallic needle) through a syringe pump at a controlled rate through the use of a needle fixed onto a syringe.

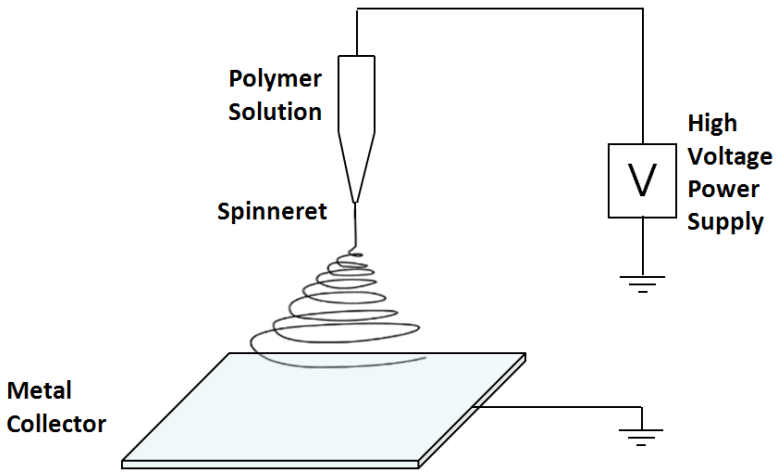

Figure 2.5 Schematic illustration of the electrospinning set-up

When a high voltage in the range of 5kV to 30kV is applied, the pendent drop of polymer solution at the needle will be instantaneously charged, due to the accumulation of like charges in the pendent drop of polymer solution. As a result, the pendent drop will experience two main forces, namely, (A) the electrostatic repulsion acting due to the accumulation of like charges against the surface tension of the pendent drop and (B) the columbic attraction between the positive charged pendent drop at the spinneret and the negative (grounded) terminal. Consequently, when the repulsive forces within the pendent drop overcomes the surface tension and coupled with the force (B), a Taylor cone will form at the spinneret [60]. A further increase on the electric field will result in the increase in the columbic force in (B), allowing a jet of polymer solution to be ejected and stretched from the Taylor cone. As the polymer solution is viscoelastic, the whipping motion of the polymer jet as it races to the collector due to the columbic force in (B) will result in the decrease in the dimensions of the polymer jet. During the whipping of the polymer jet as well as the concurrent evaporation of the solvent, a continuous

electrospun nanofiber is formed as it lands on the metallic collector. Given time, the continuous deposition of the as-spun nanofibers will form a random non-woven mat as shown in Figure 2.6. It is important to note that due to the mechanism involved in the formation of the nanofibers, molecular alignment will be induced in the as-formed nanofibers [10,61,62] as it is continuously stretched and whipped before it is deposited at the collector, similar to that seen in the extrusion of polymers.

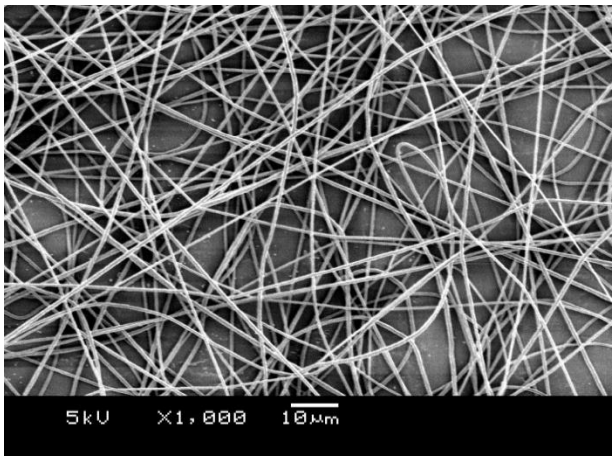

Figure 2.6 SEM micrograph of a random non-woven mat of electrospun PVDF from 20 wt.% polymer solution in 60/40 DMF/acetone.

2.3.1 Diameter control of electrospun fibers

The diameter of the electrospun nanofibers is determined by a variety of factors, namely (1) applied voltage, (2) viscosity of polymer solution which is directly related to the concentration, (3) the working distance i.e. the measurement of the distance between the spinneret and the collector, and lastly (4) polarity of the solvent used to dissolve the polymer [63-65]. Factors (1) and (4), can increase the electrical pulling force caused by the columbic attraction between the

charged pendent drop of polymer solution at the spinneret and the metallic collector, will generally cause a decrease in the fiber diameter. Factor (2) is one of the most important factor that controls both the morphology as well as the diameter of the nanofibers when electrospun and have a parallel relationship with the electrospun fiber diameter (Figure 2.7).

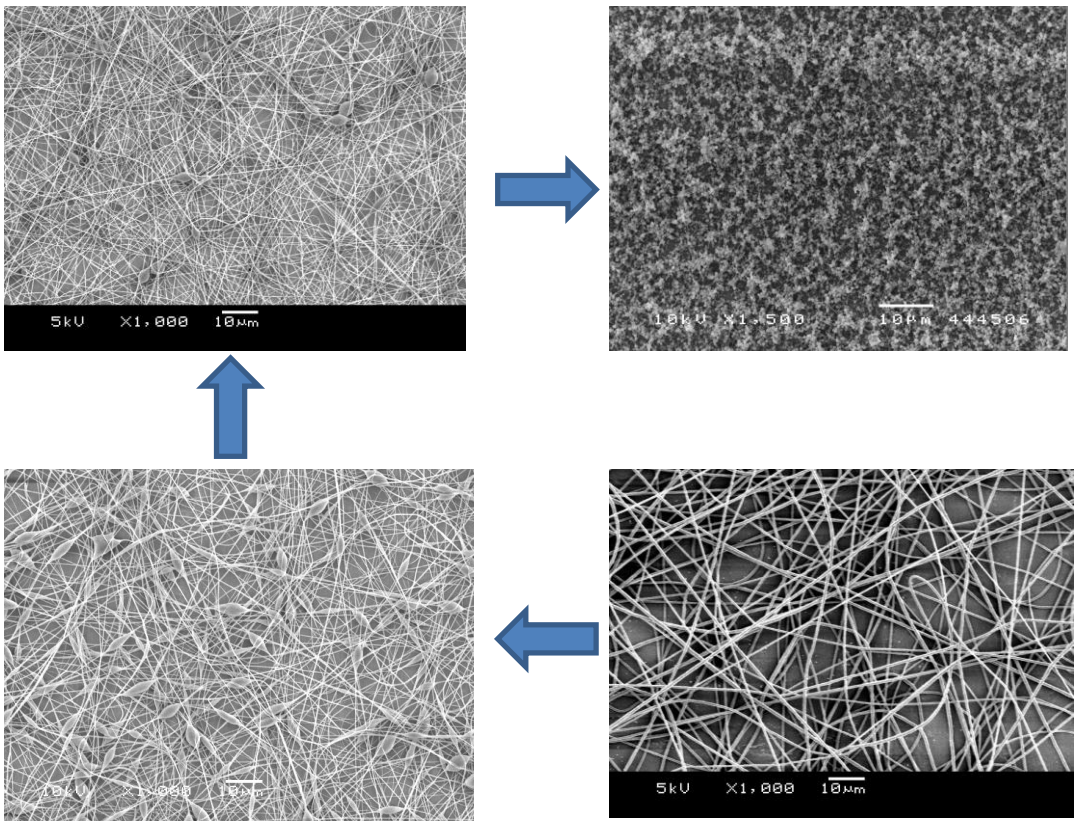

Figure 2.7 Gradual decrease in fiber diameter and the growth of beads along electrospun PVDF nanofibers (from 20 wt.%, 16 wt.%, 12 wt.% to 6 wt.%) with decreasing viscosity of polymer solution till electrospraying occurs, resulting in the formation of nanoparticles.

An increase in viscosity of the polymer solution will generally increase the diameter of the as-spun nanofibers whereas the opposite will occur when the viscosity is decreased. However, if

the viscosity decreases below a certain threshold, the visco-elastic nature of the polymer jet ejected from the Taylor cone will suffer from the effects of surface tension, resulting in the formation of beads along the fiber length, together with a general decrease in fiber diameter. This effect will continue on as viscosity of the polymer solution decreases until the viscosity is too low for the formation of fibers. Instead, electrospraying occurs, which produces nanoparticles [66].

As electrospun fibers are normally collected on a substrate as a random non-woven mat, researchers have explored different collecting methods to collect different fibrous morphology for different applications. One of the main driving forces is due to the solvent-induced relaxation of the molecular chains. When the as spun nanofiber is formed, it is still slight wet. Although the electrospinning process induces molecular alignment as well as preferentially aligned crystals along the fiber axis, due to the presence of the solvent which is still undergoing evaporation, a certain amount of molecular relaxation will occur. Thus, many researchers have looked into areas where a stretching force can be exerted during the collection of the fibers.

2.3.2 Different electrospun film morphologies by using different collectors

As explained in the previous section, the normal electrospinning process allows the user to collect nanofibers in the form of a random non-woven mat. However, by manipulating the collector used in the set-up, different film morphologies can be collected, especially in the form of aligned nanofibers.

Kim *et al* demonstrated that electrospun fibers could be aligned relatively parallel to each other when a drum rotating at high speeds was used as the collector [67], as demonstrated in

Figure 2.8. It has also been demonstrated by a few researchers [68,69] that the take up speed of the rotating drum can affect the preferred orientation of the electrospun nanofibers by a linear relationship due to the stretching forces induced by the centripetal force exerted by the collector during rotation, which prevents relaxation of the molecular chains of the polymer during collection.

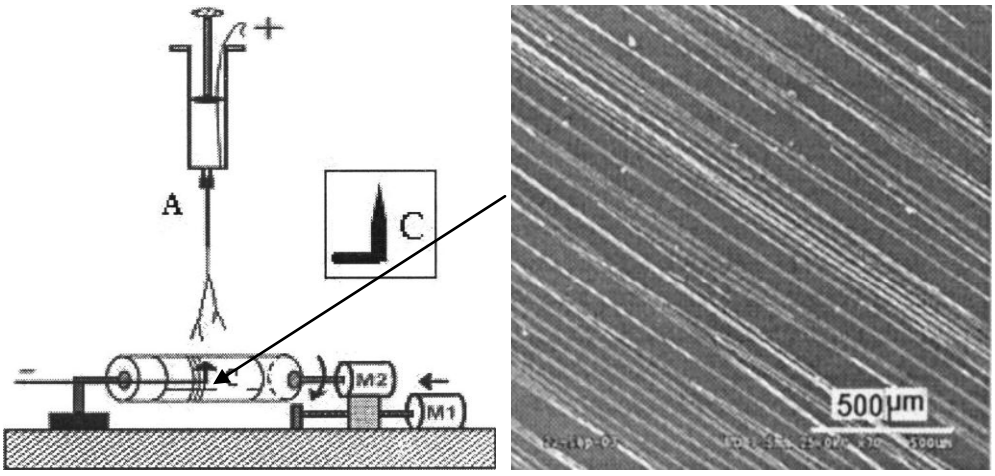

Figure 2.8 Schematic diagram of the rotating drum collector used to collect aligned nanofibers with the SEM micrograph of the aligned fibers collected attached [60].

Kameoka and Sundaray *et al* also successfully proved that through the use of high rotational speeds of the collector [70,71] aligned nanofibers can be collected. Li *et al* reported that through the use of two conducting electrodes with a gap in-between, uniaxially aligned arrays of nanofibers can be collected within the gap [15] as shown in Figure 2.9. It was discovered that by controlling the gap size between the electrodes, the molecular orientation along the fiber axis of the electrospun fiber can be controlled [72] but the control of the molecular orientation is not as significant as compared to rotating apparatus.

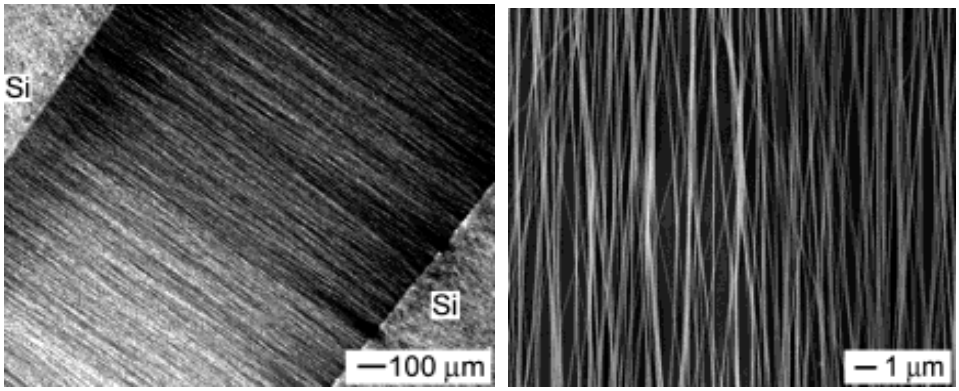

Figure 2.9 SEM micrographs of aligned nanofibers collected at the gap between 2 conducting electrodes and a SEM micrograph at higher magnification of the aligned nanofibers collected [15].

Zuessman *et al* have also achieved the collection of well-aligned nanofibers through the use of a different form of rotating collector. Using a wheel like bobbin with a sharpened edge [73,74] as shown in Figure 2.10, well aligned arrays of electrospun nanofibers can be collected. Similar to the rotating drum, the take-up velocity of this rotating disk will linearly affect the preferential molecular alignment of the crystals in the nanofibers along the fiber axis [13,75]. Although the rotating disk can collect better aligned nanofibers as compared to the rotating drum, good alignment can only be achieved near the blade but both techniques can offer a solution to control molecular orientation while collecting aligned nanofibers.

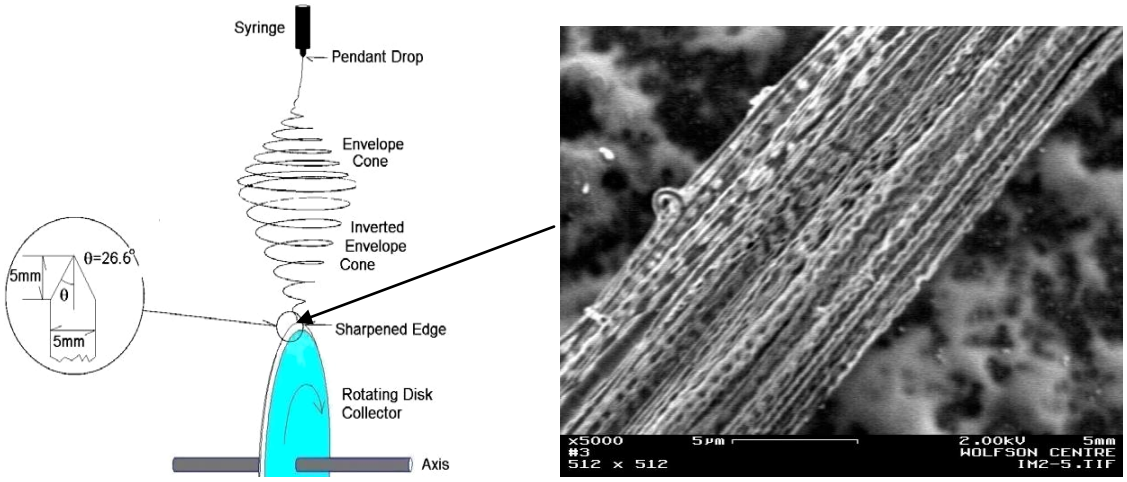

Figure 2.10 Schematic illustration of the bobbin used for the collection of well-aligned individual nanofibers [73].

2.4 Introduction to the electroactive properties of PVDF

PVDF is a electroactive polymer that exhibits a stable macroscopic polarization which can be repeatedly switched by an external electrical field between equal energy states of opposite polarization [1,19,20], meaning the existing dipole moments that arises in the material due to its structure can be switched or oriented by the application of an external electric field. This is termed as ferroelectricity.

Due to the unique properties that arise from its structure, PVDF also exhibits piezo-electric and pyro-electric properties [1]. Pyroelectricity is the property in which an electrical potential can be created when the specific material is subjected to a uniform temperature change. This is a result of the charging of the surface of the material due to the polarized or aligned poles in the molecular chains of PVDF, resulting in an electric potential to be established. The properties of both pyroelectricity and piezoelectricity are closely related, as all pyroelectric materials are also

piezoelectric. Piezoelectricity is the property in which the material can generate an electrical potential in response to an applied mechanical stress. The reverse can also occur where the electrets generate charges under an applied mechanical stress. This is called converse piezoelectricity. All these unique properties arise due to the same reason as that of pyroelectricity where the polar crystal forms of PVDF lack a center of symmetry and having polar directions when packed in the unit cell [76].

Although the piezoelectric *d*-coefficients of polymers are usually small when compared with ferroelectric ceramics [20], the dielectric constant of polymers are also small, resulting in large voltage generated per unit. Also, especially in the case of PVDF, the electromechanical coupling constant which is a measure of the conversion of mechanical energy into electrical energy is acceptably large [20]. Due to its inherent chemical toughness, resistance to sunlight, light weight, flexibility, good electrochemical stability and most importantly, the ease of fabrication as compared to other classes of materials, PVDF has been shown to act as an alternative to replace existing classes of materials in piezo and ferro-based applications.

2.4.1 Ferroelectricity in PVDF

Due to the polar forms of PVDF having a net dipole moment as a result of their packing in a unit cell within a crystal, when a PVDF film is subjected to a sinusoidal high voltage or applied electric field, the charge response yield a hysteresis (Figure 2.11).

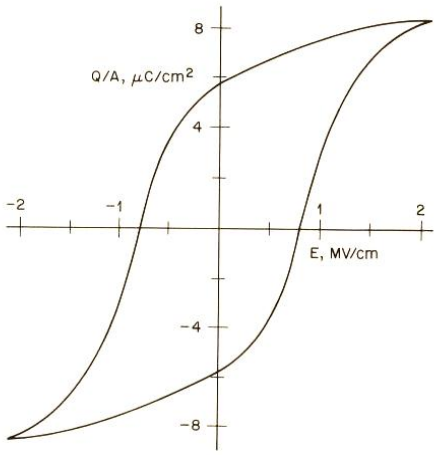

Figure 2.11 Typical hysteresis loop between electric displacement (Q/A) and electric field (E) for PVDF [19].

This is because PVDF is a non-linear dielectric. When PVDF is subjected to an increase in the applied electric field, the surface charge density increases non-linearly with the electric field as indicated in Curve 2 in Figure 2.12. However, when the applied electric field is removed, the discharge does not follow the original path but decreases smoothly as indicated in Curve 3 in Figure 2.14. This results in an appreciable surface charge that remains on the polymer film, due to the dipoles within the polar phase in the crystalline regions of PVDF becoming preferentially aligned in the direction of the applied field. The dipoles remain aligned even when the applied E-field was removed [20, 77]. The measured surface charges that remain is equal to the polarization or net dipole moment per unit volume [20]. This surface charge density is termed as the **remnent polarization** and the process whereby the net dipole introduced is termed as **poling** [19,20]. When the same electric field is applied again in the same direction, it will cause an increase in the surface charge density by Curve 4 as shown in Figure 2.12. When the applied electric field is removed, it will again follow the same path as in Curve 3.

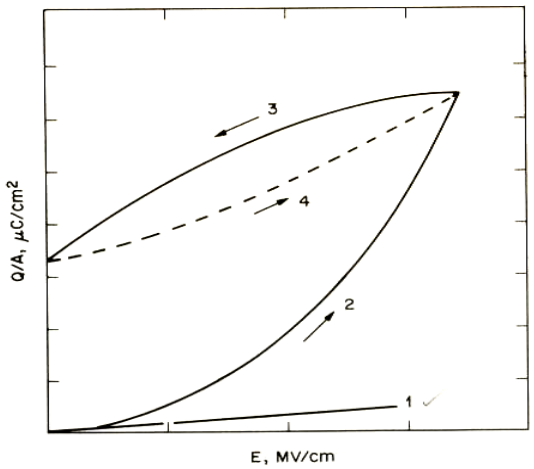

Figure 2.12 Charge per unit area (Q/A) on electrodes vs E-field(E) for linear and non-linear dielectrics [19].

For non-linear dielectrics, when the direction of the applied electric field is changed to the opposite direction, the surface charge density decreases smoothly till a critical field is reached at which the charge decreases rapidly and changes sign, as shown in Figure 2.12. This corresponds to the collective rearrangement of crystalline dipoles in the direction of the field which is now being applied on the polymer. The value of the field that the polarization pass through zero is termed as the coercive field and upon returning the field to zero, the remnant polarization is of the opposite sign [19,20]. Thus, an applied sinusoidal electrical field to PVDF can result in the repeated cycle of the hysteresis loop, allowing PVDF to exhibit ferroelectric switching [1] of dipoles. However, by applying a direct electrical field, poling [77,78] will occur whereby the dipoles within the crystalline regions will re-orientate, resulting in a strong dipole moment and large remnant polarization. This large remnant polarization is required for PVDF to fully exhibit its piezoelectricity.

2.4.2 Piezoelectricity and pyroelectricity in PVDF

When piezoelectric PVDF has been deformed by an applied force, it will result in the change in the polarization, giving rise to a direct piezoelectric effect. Many groups have studied this phenomenon in relation to PVDF through simple experiments and determined the various independent piezoelectric coefficients, namely d_{31}, d_{32}, and d_{33}. It is important to note that the first number used in the suffix 31 in relation to d_{31} refers to the direction of polarization while the second number refers to the direction in which the stress or strain is applied, as in Figure 2.13. The same goes for pyroelectric coefficients but instead of which direction is the stress/strain is applied, the suffix refers to the direction in which the measurements are taken.

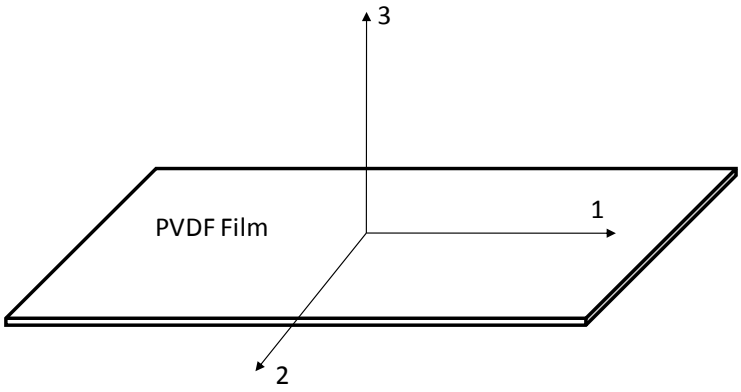

Figure 2.13 Axes on film for the naming of the different coefficients for the piezoelectric constants.

As the focus of this thesis is not on determining both the piezoelectric and pyroelectric coefficients, it is more important to note that these constants which relates to the materials' piezoelectric properties is extremely dependent on (A) the amount of polar phases in PVDF, especially the β-phase, (B) adequate poling, (C) the degree of crystallinity of PVDF and lastly

(D) the alignment of the molecular chains [25] within the crystals at room temperature and pressure. As electrospinning can enhance (A) to (D) at the same time, it can be a good processing platform to enhance the electroactive properties of PVDF. Additionally, as the rotating apparatus can prevent solvent-induced relaxation of the as-spun PVDF nanofibers during collection, it is worthwhile to explore the improvement of the collection set-up to enable the collection of a well-aligned fibrous membrane and examine the impact of additives under this extensional force and its impact on polymorphism of PVDF as well as its influence on its electroactive properties.

2.5 Potential applications of electrospun PVDF fibers

Electrospun PVDF membranes have been extensively studied and researchers have tried to find novel uses for such morphologies. One of the first reported practical use of such electrospun PVDF membranes was reported by Sun *et al*, where electrospun PVDF membranes embedded with multi-walled carbon nanotubes (MWCNT) was used to enhance the β-phase in PVDF to produce PVDF nanoweb touch sensors [79]. The device utilizes the piezoelectric properties of the PVDF nanofibers but the authors did not address the fundamentals of how and why it happens except for the demonstration of the device. A more detailed understanding of the piezoelectric properties was reported by a team led by Lin *et al* where they demonstrated the actuator properties of a single electrospun PVDF nanofiber [80,81] and a 50% increase in the piezoelectric constant, d_{33}, was achieved by a single electrospun PVDF fiber as compared to PVDF thin films. The increase is attributed to the inherent poling of the electrospinning process that aligns the dipoles within the fiber as well as molecular alignment induced during the spinning process, allowing a more efficient energy conversion from mechanical to electrical energy.

Electrospun PVDF membranes have also been studied for other applications and one such use is tissue regeneration [82,83] and it has been been proven that PVDF is biocompatible, allowing such membranes to seed cells where cells proliferate. Various groups have also used electrospun PVDF membranes in renewable energy areas. Park and Priya *et al* both demonstrated the potential of utilizing such electrospun PVDF membranes in dye-sensitized solar cells (DSSC) [84,85] where the electrospun membranes act as a polymeric host for the electrolyte layer. Such electrospun PVDF membranes have also been proven to be used as polymer electrolytes and as separators in lithium batteries [86-88].

Electrospun PVDF membranes have also been investigated for their hydrophobic properties. By adding tetraethyl orthosilicate (TEOS) directly into PVDF solutions prior to electrospinning, the resulting random nanofibrous mats formed were mechanically stronger and yield super hydrophobic surfaces [89]. Superhydrophobic electrospun PVDF fibrous mats in the non-woven form can also be made by grafting silane or fluorinated groups onto the PVDF main chain prior to electrospinning [90]. Electrospun membranes have also been demonstrated as efficient particulate filters and having anti-bacterial properties [91,92], making them suitable for use in water treatments. Thus, electrospun PVDF membranes have the potential for many applications. However, the electroactive properties of PVDF are still one of the most desirable properties for this polymer.

3 Effects of Extensional Force on Polymorphism and Morphology of Electrospun PVDF Nanofibers

3.1 Introduction

As mentioned in the previous chapter, electrospinning is a technique that allows the fabrication of molecular aligned crystallites within the polymer in the form of nanofibers. This form of crystallite arrangement is beneficial to piezoelectric and ferroelectric thin film devices, where the direction of the applied electric field is normally perpendicular to the film surface. If the c-axis of the β crystallites are oriented parallel to the film surface, the dipoles of the all-*trans* conformers will be in the b-axis direction of the orthorhombic lattice, which can be easily aligned along the normal of the thin film by the applied electric field. Additionally, it has been demonstrated that electrospinning can enhance the β-phase of P(VDF-HFP) [10]. However, the as-spun nanofibers may suffer from a certain degree of solvent induced relaxation due to the time required for the solvent to fully evaporate off from the nanofibers. This process will minimize the effectiveness of producing crystal orientation and β-phase enhancement within the nanofibers by electrospinning. One of the easiest ways to reduce such relaxation is to provide a stretching force during the evaporation of the solvent. A common approach is to use rotating apparels such as a drum or disk to collect preferentially aligned fibers in the rotating direction. With the rotating disk, highly aligned fibrous thin films can however, only be obtained in a very small area around the tip of the blade. With the rotating drum, large-area collection of preferentially

aligned electrospun fibers is possible but the quality of the alignment is not as good as that achieved with the rotating disk. Both techniques allow the application of a stretching force due to the strong centripetal force present during rotation. A certain control on the degree of crystal orientation has also been demonstrated when the fibers are collected in the air gap between two static parallel electrodes due to the residual electrostatic repulsion between the electrospun fibers, resulting in aligned fibers been collected; whereas the transfer of the nanofiber assemblies onto a solid substrate usually causes fiber breakage, especially for weak polymeric nanofibers. To overcome the aforementioned problems, the direct deposition of well aligned electrospun fibrous thin films of PVDF-based polymers uniformly onto a relatively large flat substrate (centimeter scale) using a simple set-up, i.e. a modified rotating disk collector, is attempted. The modification is similar to some modified rotating collectors in terms of utilizing both electric field and mechanical force to align the fibers [2]; however, instead of the addition of auxiliary electrodes, our modified rotating disk have separate, parallel electrodes attached on the rotating disk, which can stretch the fibers in the air gap between the separate electrodes effectively. The influences of the combined force fields on morphology, crystal structure and orientation of the polymers are investigated, and the results are presented in this chapter. Ferroelectricity of the aligned 2D nanofiber assemblies is also demonstrated.

3.2 Experimental procedures

Materials. P(VDF-HFP) powders (Solef 11008) and vinylidene fluoride-trifluoroethylene copolymer (P(VDF-TrFE), 70/30 mol% pellets (M_w = 165,000) were used as received. *N*,*N*-dimethylformamide (DMF) and acetone were supplied by Aldrich.

Electrospinning. A DMF/acetone mixture was prepared at the DMF/acetone weight ratio of 60/40. P(VDF-HFP) and P(VDF-TrFE) were then dissolved in the solvent mixture at the polymer/solvent weight ratio of 20/100. A solution was also made by mixing 0.01 wt.% functionalized MWCNT with PVDF in the solvent mixture. The polymer solutions were placed in a plastic syringe fitted with a needle of tip-diameter of 200 μm. The electrospinning was conducted at 15 kV with a high-voltage power supply at a working distance of 15cm, above the collector. A syringe pump was used to feed the polymer solutions into the needle tip at the rate of 0.25 ml/hr. The electrospun fibers were collected using the conventional (unmodified) and modified rotating disk, as shown in Fig. 1, at the rotating speed of 1500 rpm for one hour. The modified rotating disk (Fig. 1b) has separate, parallel aluminum plates with sharp edges attached on the unmodified rotating disk. Grounded flat substrates, such as indium tin oxide (ITO) glass or silicon wafer, were placed between the aluminum plates to collect the aligned electrospun fibers in the rotation direction. Static separate electrodes [15] were also used to collect the nanofibers electrospun under the same conditions to make reference samples. All electrospun fibers were dried *in vacuo* at room temperature overnight prior to characterization.

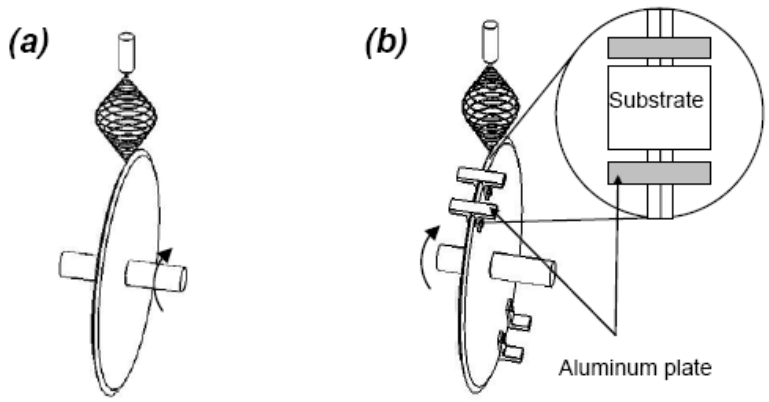

Figure 3.1 Schematics showing the electrospinning process using (a) a conventional rotating disk collector and (b) the modified rotating disk collector.

Scanning electron microscopy (SEM). The morphology of the electrospun fibers was examined using *a JEOL 5600* SEM. A thin layer of gold was sputtered on the sample surface before the examination.

Wide angle x-ray diffraction (WAXD). WAXD patterns were recorded with a Bruker GADDS x-ray diffractometer equipped with a two-dimensional (2D) area detector using CuK_{α} radiation. The random mats were rolled to make tubes of ~1 mm diameter for the x-ray measurement while the aligned samples were measured directly without rolling, as shown in Figure 3.2. For all samples, 2D diffraction patterns were collected from 15 to 50° *2θ*, and integrated to obtain azimuthal average intensity against 2θ plots using GADDS software package. To examine crystal orientation, the same GADDS software package was used to obtain the radial average intensity of equatorial reflections versus azimuthal angle (χ) plots.

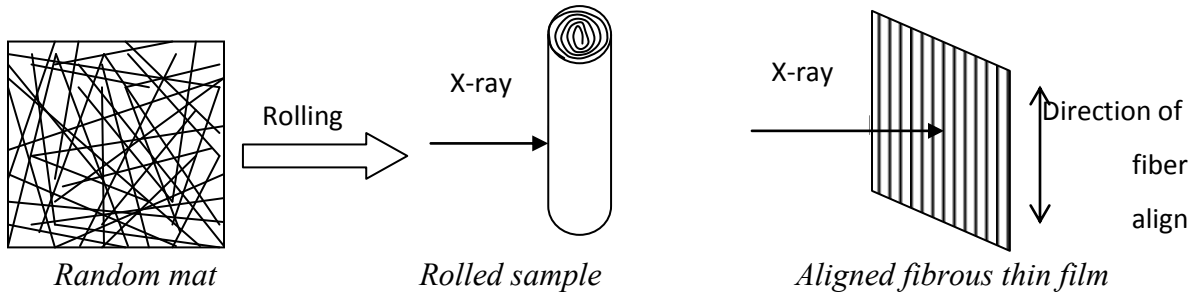

Figure 3.2. A schematic of the geometries of the WAXD experiments

Differential scanning calorimetry (DSC). The DSC curves of the materials were measured using a TA Instruments Modulated DSC 2920. The sample was heated at 20°C/min from 25 to 200°C. All experiments were performed under a nitrogen purge.

Attenuated fourier transform infrared spectroscopy (AT-FTIR). FTIR spectra were collected using a Perkin Elmer FTIR System Spectrum GX equipped with a Golden Gate Single Diamond Attenuated Total Reflection (**ATR**) unit (Grasby Specac ATR 10500). The samples were placed on top of the ATR set and scanned from 4000 to 600 cm^{-1}. A total of 16 scans were collected for signal averaging.

Piezoresponse force microscopy (PFM). The surface topography and the PFM images were carried out on an atomic force microscope (Asylum Research MFP-3D), using a platinum/iridium-coated tip with a force constant of 2 N/m.

Polarization measurement. The fibrous thin films were sandwiched between a thin piece of aluminum plate and a copper strip covered with a glass slide. The assembly was clamped tightly together using Hoffman clamps. The polarization was then measured using a Radiant Technology RT6000HVS polarization tester. A total of 20 measurements were taken for signal averaging. Film thickness was measured using an Elcometer 456 equipped with probe T456F1S.

3.3 Results and discussions

3.3.1 The alignment process

During the electrospinning, it can be clearly observed that the modified rotating disk leads to fanning of the electrospun fibers as they approach the aluminum plates, as shown in Figure 3.3. This is because that the conductive aluminum electrodes on the disk effectively reduce the

strength of the electric field on the tip of the disk [71, 73] and hence foster the electrospun fibers to whip in the directions off the tip of the disk. The fanning process promotes solvent evaporation so that the electrospun fibers may subsequently be more effectively stretched at a high viscosity state when crossing the gap between the separate electrodes on the disk. The impact of this on crystalline structures and orientation of the polymers will be discussed later.

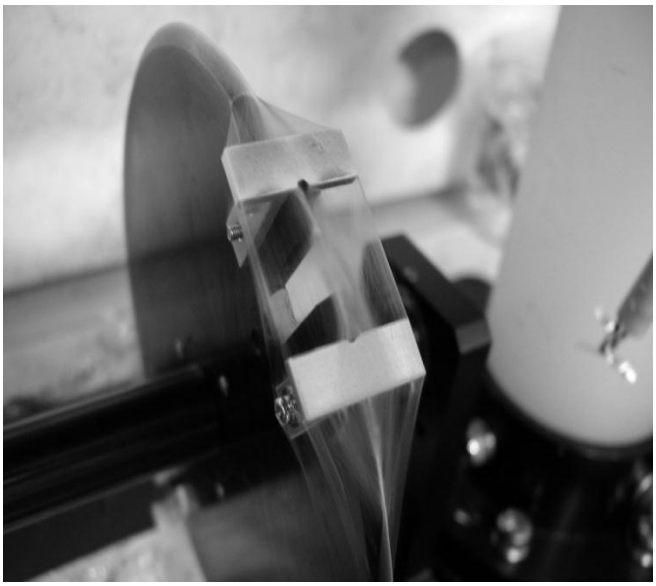

Figure 3.3 A picture showing the fanning of the electrospun fibers on the modified rotating disk collector. No substrates were placed between the two aluminum electrodes.

3.3.2 Morphology of the 2D nanofiber assemblies

It is found that the degree of alignment of the electrospun fibers collected using the modified and unmodified rotating disks are about the same (Figure 3.4a and 3.4b), the lateral distribution of the fibers on the substrates are however very different for these two methods (Figure 3.5a and 3.5b).

Static Separate Electrodes

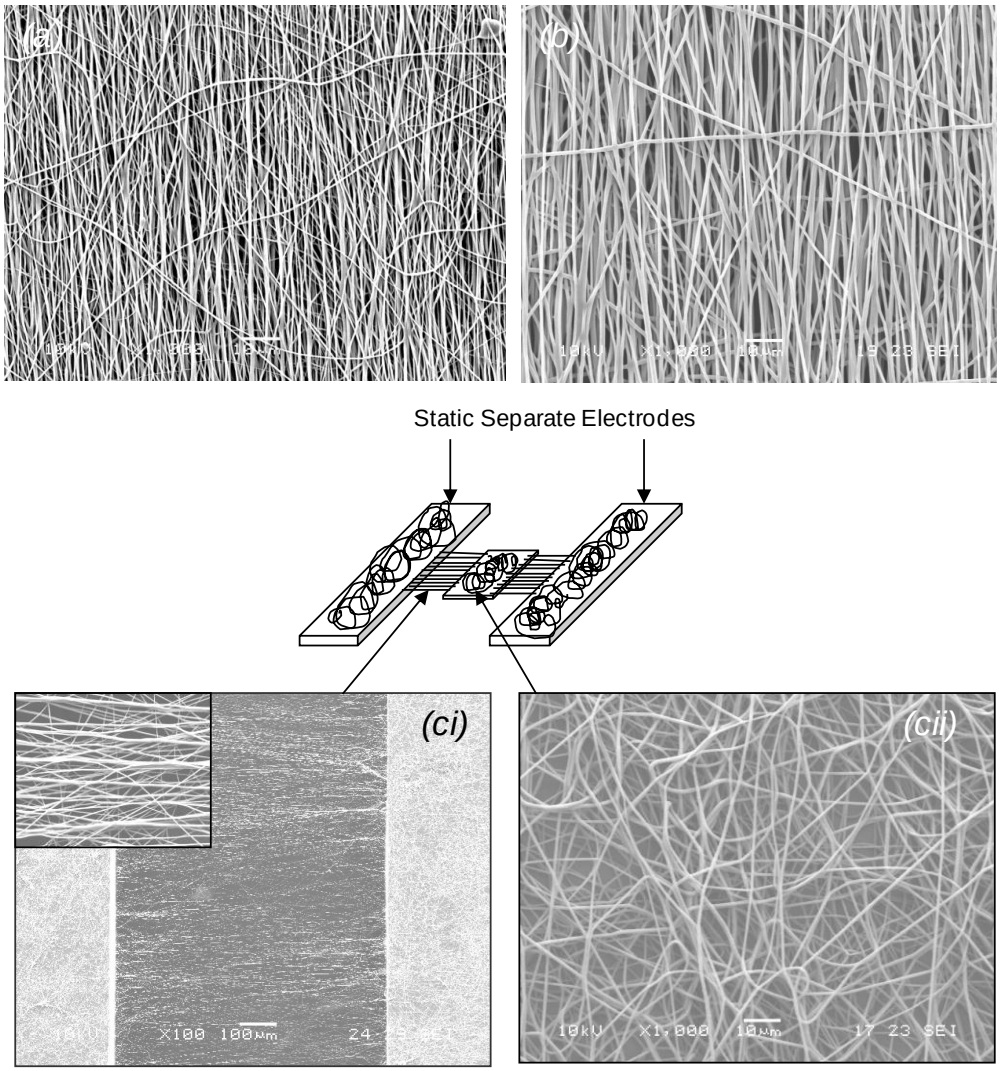

Figure 3.4 ***SEM micrographs showing the morphologies of the electrospun P(VDF-TrFE) fibrous thin films obtained using (a) the modified rotating disk collector, (b) the unmodified rotating disk collector and (c) static separate electrodes. The inset in (ci) shows the morphology of the aligned fibers after being transferred onto an ITO substrate and*** **was obtained by imaging on aligned fibers between the air gap after been transferred onto an ITO substrate while (cii) was obtained by imaging the collected nanofiber mat on the surface of the substrate**

For the modified rotating disk, the specific electric-field-distribution created by attaching the aluminum electrodes, coupled with the repelling force from the residual charges on the electrospun fibers, gives rise to an uniform deposition of the electrospun fibers on the flat substrates across a relatively large distance (25 mm) in the lateral direction (Figure 3.5a), while in the longitudinal direction the electric field between the two parallel electrodes, coupled with the mechanical force exerted by the rotating disk, ensures the good alignment of the electrospun fibers after the fanning, as shown in Figure 3.4a.

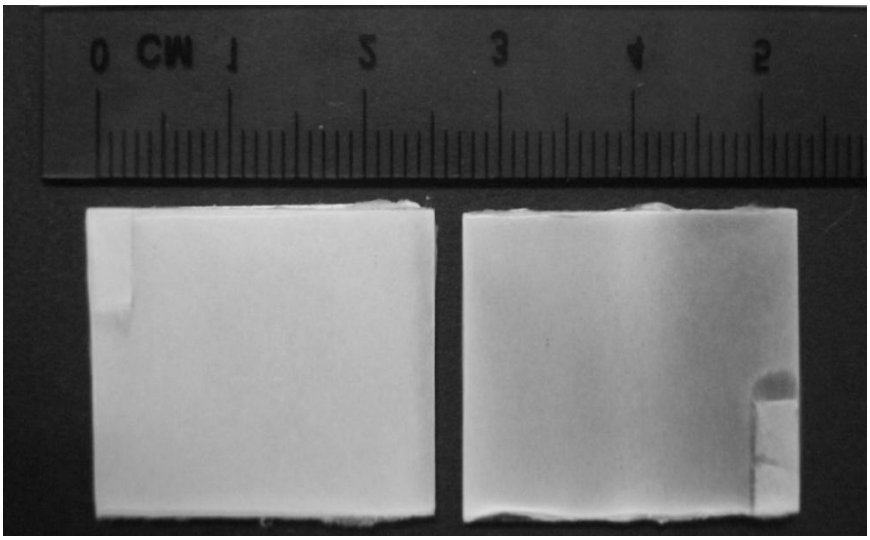

Figure 3.5 A picture showing electrospun P(VDF-TrFE) fibrous thin films collected on ITO substrates using (a) the modified rotating disk collector and (b) the unmodified rotating disk collector. In (b) the central area is whiter than the two sides because of the low density of the electrospun fibers on the two sides.

In contrast, a uniform lateral distribution of electrospun fibers cannot be achieved when ITO substrates are attached on the unmodified disk, as shown in Figure 3.5b. For the static separate

electrodes with a substrate in between, the alignment of the electrospun fibers can only be observed in the air gaps between the electrodes (Figure 3.4ci), while on the substrates the fibers form a random mat (Figure 3.4cii). Some misaligned thin fibers can also be observed in the aligned region due to the breakage of weak fibers during transferring the sample onto a substrate (inset in Figure 3.4ci). Obviously, static separate electrodes are unsuitable for the direct deposition of aligned electrospun fibers onto conductive substrates. Compared with the static separate electrodes, the modified rotating disk collector is also able to provide good alignment in a longer (in the fiber axis direction) and thicker sample, and improves the compactness of the fibrous thin films due to the mechanical force exerted by the rotating disk.

3.3.3 Crystal structures and orientation

P(VDF-HFP) fibrous thin films were fabricated via four different routes, namely collected (1) on an ITO substrate between the static separate electrodes, (2) in the air gap between the static separate electrodes, (3) using the unmodified rotating disk and (4) using the modified rotating disk. For convenience, the four types of fibrous thin films will be named as Sample A, B, C and D, respectively, in the rest of the paper. WAXD patterns and FTIR spectra of the four samples are shown in Figure 3.6A and Figure 3.7, respectively. For Sample A (a random mate), a strong diffraction peak at $2\theta = 20.6°$, which corresponds to the sum of the (021) reflection of the α-phase and (200)/(110) reflections of the β-phase, and distinctive peaks at around 18.5 and 27.4°2θ, which correspond to (020) and (111) reflections of the α-phase respectively, indicate the co-existence of the α- and β-□phases.[81] This is corroborated by its FTIR spectrum (curve a in Figure 3.7) where the α-phase related bands can be observed at 614, 765, 795 and 975 cm^{-1} and the β-phase related bands at 840 and 1278 cm^{-1} [82] Sample B and C, although being aligned ones,

show similar diffraction patterns and infrared spectra to those of Sample A, while for Sample D a shoulder peak appears at around 22° 2θ despite that the infrared spectrum of the sample remains similar to the others. The shoulder peak at 22° 2θ is an equatorial peak and can be assigned as the (200)/(110) reflections of the β-phase, which indicate that although the use of the modified rotating disk collector does not have a significant β-phase enhancement effect, it leads to the formation of the β-crystallites with slightly reduced inter-chain distance.

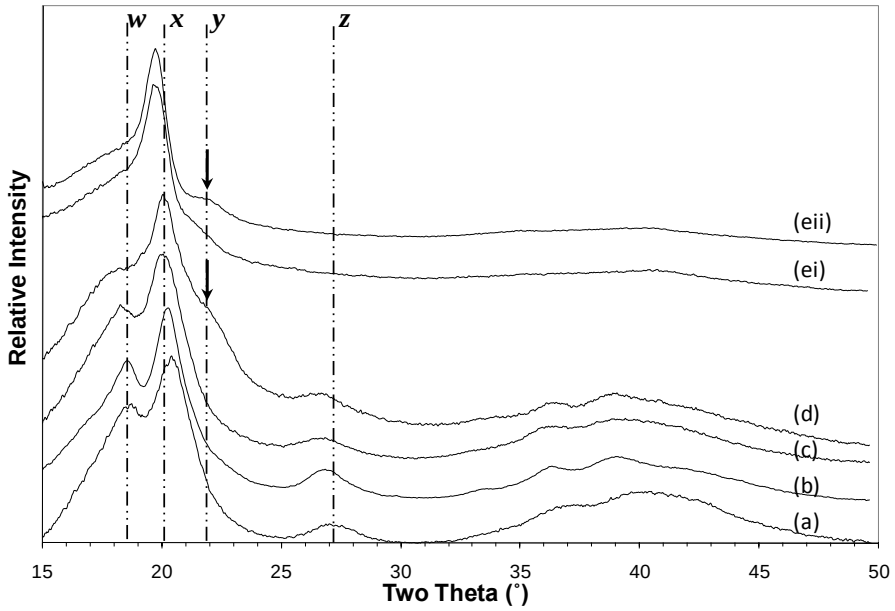

Figure 3.6 **WAXD patterns of electrospun P(VDF-HFP) fibrous thin films collected using (a) the static separate electrodes on an ITO substrate, (b) the static separate electrodes in the air gap (c) the unmodified rotating disk (d) the modified rotating disk and (e) P(VDF-TrFE) fibrous thin films collected using (i) the unmodified rotating disk and (ii) the modified rotating disk. w denotes the *(020) reflection of the α-phase, x denotes the sum of the (021) reflection of the α-phase and (200)/(110) reflections of the β-phase, y denotes (200)/(110) reflections of the β-phase with reduced interchain distance and z denotes* (111) *reflections of the α-phase.***

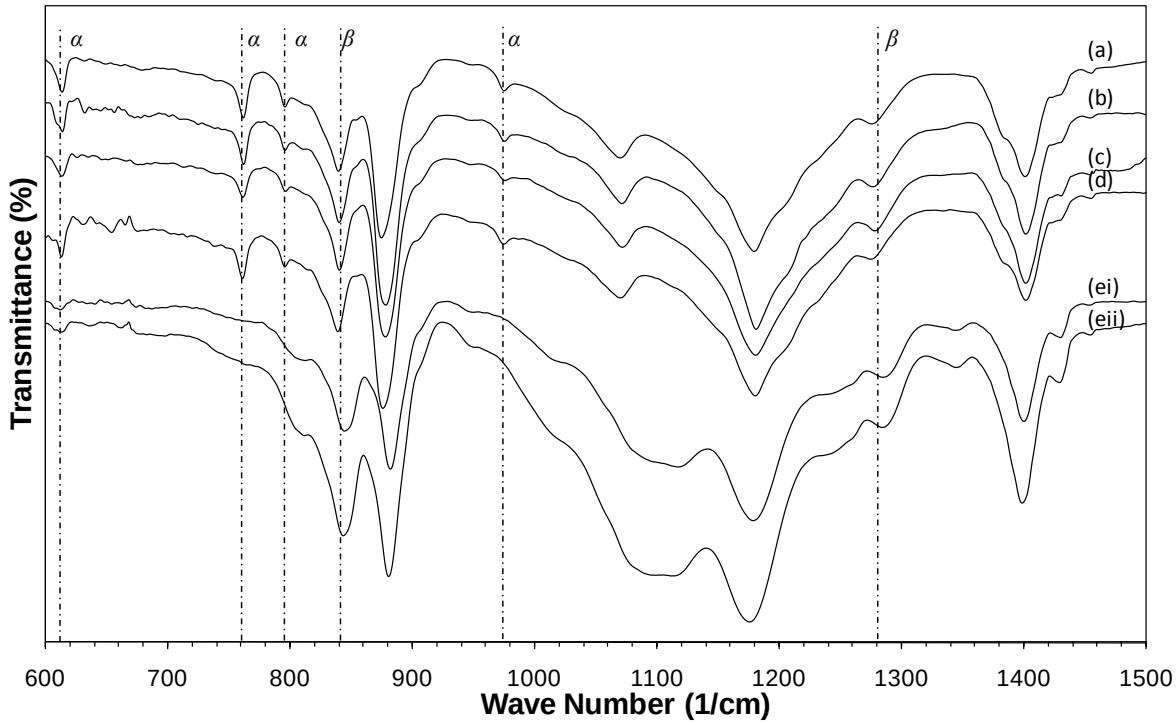

Figure 3.7 FTIR spectra of electrospun P(VDF-HFP) fibrous thin films collected using (a) the static separate electrodes on an ITO substrate, (b) the static separate electrodes in the air gap, (c) the unmodified rotating disk and (d) the modified rotating disk. (e) is the FTIR spectra of the electrospun P(VDF-TrFE) fibrous thin films, respectively, collected using (ei) the unmodified rotating disk and (eii) the modified rotating disk.

The crystal structure associated with the shoulder peak at 22° 2θ may somewhat resemble the β-form extended-chain crystals formed during high-pressure crystallization of PVDF, for which the (200)/(100) reflections also appear at a slightly higher angle than normal [93]. A hypothetic mechanism for the formation of such a structure via the use of the modified rotating disk collector is that the fast solvent evaporation during the fanning may create a specific high-viscosity environment where a tensile stress could be effectively loaded onto polymer chains

when the fibers are stretched between the two electrodes by the electric field and mechanical force, whereas the polymer chains could still pack to crystallize through "sliding diffusion" [94]. By tubular film extrusion and drawing, fibril crystals can be nucleated in PVDF [4] so that it is not surprised that they may also form in highly stressed electrospun fibers. In addition, the slightly twisted zigzag conformation based on energy minimization without stress [1,2] may become a more perfect planar-zigzag under the tensile stress, which may make slightly smaller lattice parameter(s) possible, as illustrated in Figure 3.8. The structure change could only be observed via WAXD probably because the conformational change is too small to be detected by FTIR.

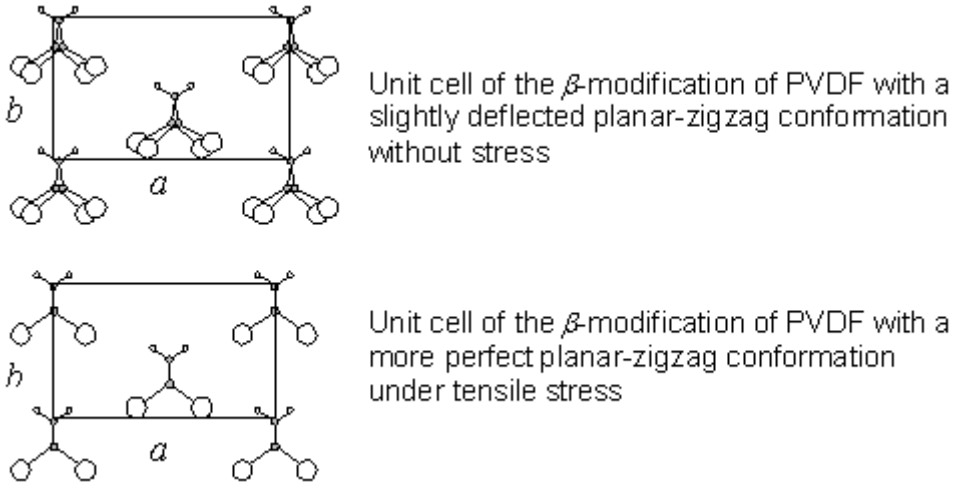

Figure 3.8 A qualitative scheme illustrating the proposed structural change for the β-form crystal.

To confirm that the diffraction peak at 22° 2θ is indeed from the β-form crystallites induced by the use of the modified rotating disk collector, the unmodified and modified rotating disk collectors are used to collect electrospun P(VDF-TrFE) nanofibers (Sample Ei and Eii). Almost

pure β-phase is obtained with both the unmodified and modified rotating disk collectors as no α-phase diffraction peak and infrared band are observed (Figure 3.6B(e) and Figure 3.7(e)). More importantly, the use of the modified rotating disk collector also leads to a distinct diffraction peak at around 22º 2θ for P(VDF-TrFE) (Figure 3.6B(e)(ii)). The consistent trend observed from P(VDF-HFP) and P(VDF-TrFE) confirms that the diffraction peak at 22º 2θ is a characteristic of the β-phase obtained in the specific environment created on the modified rotating disk collector. It is worth noting that in this work the WAXD patterns were obtained by placing highly aligned electrospun fibers perpendicular to the x-ray beam so that meridianal and some off-equator peaks are very weak. The verification of the proposed crystalline structure and superstructure requires further experimental studies and molecular simulation, which are beyond the scope of this work.

Table 3.1 shows that the use of the modified rotating disk also leads to a slight increase in peak melting temperature and heat of fusion, which signifies the slight increase in crystal size and crystallinity due to the stretching of the nanofibers. The increased crystallinity for P(VDF-HFP) and P(VDF-TrFE) may come from both the α- and β-phases as from the WAXD patterns and FTIR spectra of Sample D and Eii we can observe very slight enhancement of the *a*-phase as compared with Sample C and Ei. The melting temperatures of the fibrous thin films collected using the modified rotating disk are only marginally higher than that from the unmodified rotating disk but much lower than that of the β-form extended-chain crystals obtained under high pressure conditions [93], which is probably due to the much smaller crystal size in the nanofibers.

Figure 3.9 shows the 2D WAXD patterns of Sample C and D. Clearly, the equatorial peak at 22º 2θ for Sample D corresponds to the crystallites being more oriented along the fiber axis, which can be observed from the increased sharpness of the arc. This supports the hypothesis that this peak arises from the crystals which is induced by the tensile stress in the fiber direction.

Table 3.1 Heat of fusion and peak melting temperatures obtained from the 1st heating DSC curves of the aligned electrospun fibrous thin films using various types of collectors.

Material	Collector	Heat of fusion (J/g)	Melting Temperature (˚C)
P(VDF-HFP)	Static separate electrodes	46.0	156.4
P(VDF-HFP)	Unmodified rotating disk	46.1 (±0.12)	156.9 (±0.51)
P(VDF-HFP)	Modified rotating disk	48.0 (±0.60)	157.9 (±0.41)
P(VDF-TrFE)	Unmodified rotating disk	34.6 (±0.47)	153.2 (±0.19)
P(VDF-TrFE)	Modified rotating disk	35.6 (±0.44)	154.6 (±0.29)

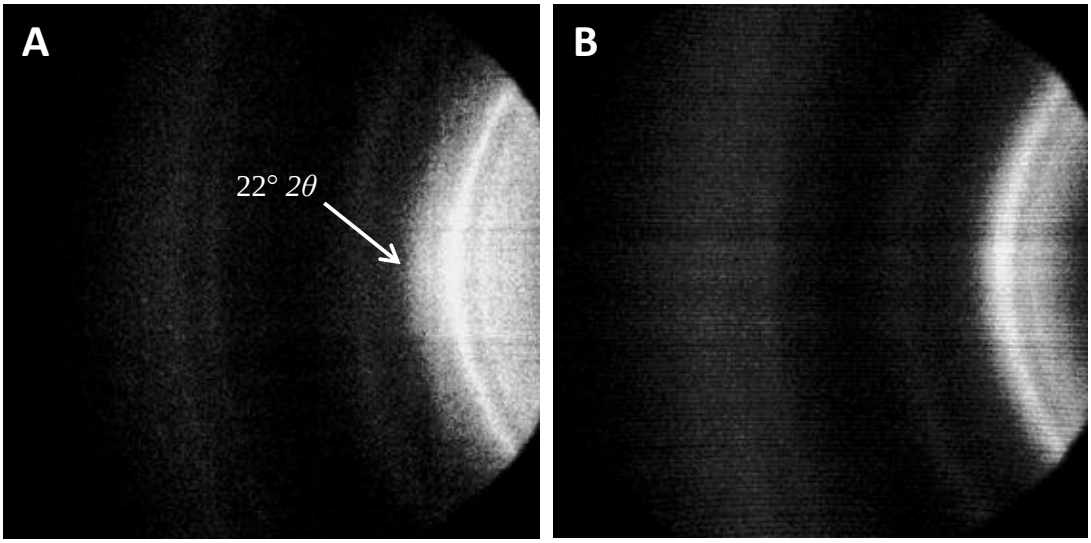

Figure 3.9 2D WAXD patterns of the electrospun P(VDF-HFP) fibrous thin films obtained using (a) the modified rotating disk and (b) unmodified rotating disk collector.

3.3.4 Ferroelectricity of the thin films

The electrospinning process involves the use of very high voltages to induce the formation of nanofibers. Such high voltages have been speculated to provide a poling effect on the PVDF nanofibers, allowing the alignment of the dipoles within, to the source of the electric field [77,78], enabling it to be utilized as actuators or nanogenerators. However, only the physical measurement of the piezoelectric response from a single electrospun PVDF nanofiber was attempted [77,78]. It was achieved by electrospinning either one or a few strands of PVDF nanofibers on a flexible substrate and allowing the substrate to bend, which in turn stretched the nanofibers. The stepped up electrical signal in response to the force generated on the nanofibers was then measured. One major offset in their technique is that the signal can only be picked up on the ends of the nanofiber being tested as electrodes could only be deposited on the ends. Although this gives us a clue that poling may have occurred during the electrospinning process, there is no direct evidence of the poling effect for the entire fiber. To verify the poling effect, we conducted PFM measurements on a single electrospun P(VDF-HFP) nanofiber (Figure 3.10). The topography of the single electrospun P(VDF-HFP) nanofiber can be clearly seen from the PFM scan (Figure 3.10A), where the diameter is approximately 600 nm. If the direction of polarization (direction of dipoles) is upwards from the origin of the *c*-axis along the fiber, the application of a positive voltage will give rise to a contraction. However, if the polarization is downwards, as shown in Figure 3.11, the application of a positive voltage will give rise to an expansion in the localized area. Thus, this allows the PFM to map the direction of the dipoles depending on the deflection, as well as the piezo-response that is detected by the conducting tip, which is shown in figure 3.10B and 3.10C. From the PFM image shown in Figure 3.10B(c), we can observe relatively uniform color shade along and across the single PVDF nanofiber, showing that the dipoles are generally aligned downwards. It is approximately 150° from the *c*-axis, as

illustrated in Figure 3.11. The PFM results provide some evidence that the electrospinning process can provide *in-situ* poling to the nanofibers, which is consistent to what has been reported in literatures. These results give us some encouragement to try to measure the ferroelectric response of the electrospun P(VDF-HFP).

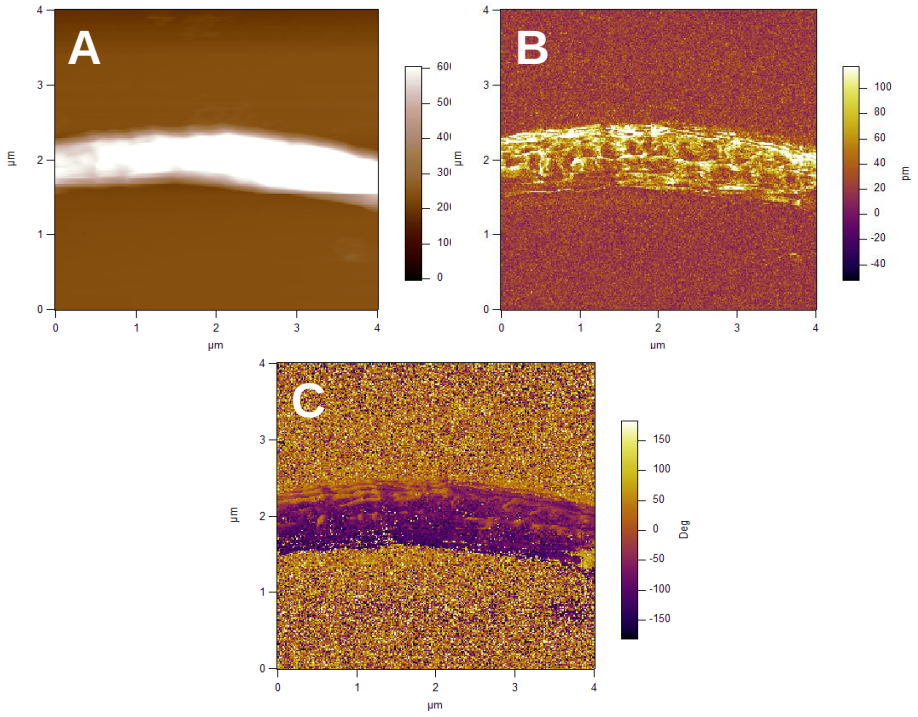

Figure 3.10 PFM image of a single electrospun P(VDF-HFP) fiber showing (A) the height, (B) the amplitude of the piezoelectric response and (C) the orientation of the dipoles within a single fiber.

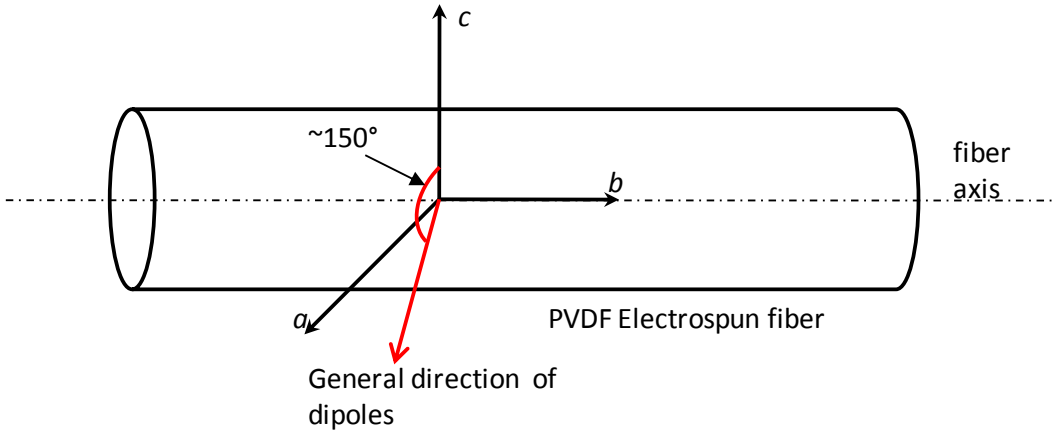

Figure 3.11 Schematic illustration of the general direction of the dipoles within a electrospun P(VDF-HFP), measured using the PFM.

To demonstrate ferroelectricity of the electrospun P(VDF-HFP) nanofibers, polarization of the P(VDF-HFP) fibrous thin film was measured, with the electrospun P(VDF-TrFE) and P(VDF-HFP)/P(VDF-TrFE) blends as references. In the measurements, polarization saturation could not be achieved due to short circuiting at high E values. Nevertheless, P-E hysteresis loops were obtained at relatively low voltages, as shown in Fig. 3.12. The polarization achieved at the maximum E clearly increases with the P(VDF-HFP) content in the blends. The P(VDF-HFP) exhibits higher polarizability than the P(VDF-TrFE) copolymer, which may be attributed to the much higher crystallinity of the P(VDF-HFP) nanofibers and the larger dipole moment of the β-phase of P(VDF-HFP) than that of the β-phase of P(VDF-TrFE) per unit cell. Since P(VDF-HFP) and P(VDF-TrFE) do not co-crystallize [84], the composition dependence of the polarization suggests that the macroscopic polarization observed at the maximum E could be partially caused by constituent dipoles of the blends rather than purely caused by the trapped charges. The charge trapping could be attributed to the fibrous nature of the films, which

inevitably resulted in some voids. This is also the main reason that polarization saturation could not be achieved. Due to the extensive leakages and charge trapping, more work has to be done to verify the P-E hysteresis loops observed, which is a subject for future research.

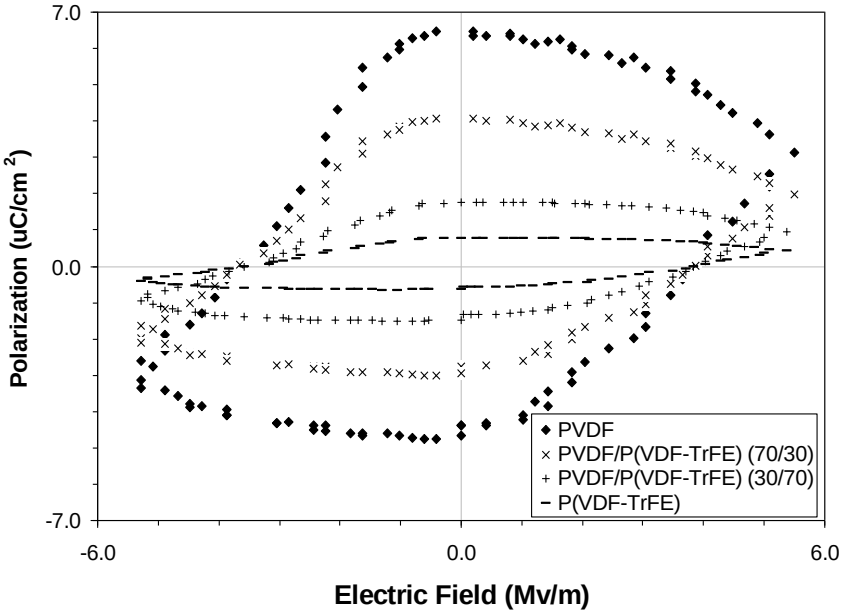

Figure 3.12 Hysteresis loops obtained from the aligned electrospun fibrous thin films of P(VDF-HFP), P(VDF-TrFE) and PVDF/P(VDF-TrFE) blends. All were collected using the modified rotating disk collector.

3.4 Conclusions

Using the modified rotating disk collector, the direct deposition of well aligned electrospun P(VDF-HFP) nanofibers with relatively good compactness and uniformity across a relatively large flat substrate is achieved. The modification alters the electric-field-distribution on the disk, which fosters the fanning of the nanofibers, while the electric field between the separate electrodes and the mechanical force exerted by the rotational disk facilitate the alignment. The specific environment and force fields created on the modified rotating disk cause the electrospun

fibers being effectively stretched to form highly oriented β-form crystallites with slightly reduced inter-chain distance. It also leads to slight increases in crystallinity and crystal size. A hypothetic mechanism for the structural alteration is proposed: it may be related to the formation of extended-chain crystals with a more perfect planar-zigzag conformation under a high tensile stress. The P-E hysteresis loops obtained from aligned P(VDF-HFP) fibrous thin films provides some evidence for the switching of the dipoles in the electrospun P(VDF-HFP) nanofibers.

4 Synergistic Effects of Extensional Force and Incorporation of Carbon Nanotubes on Polymorphism of the Electrospun Composite Nanofibers

4.1 Introduction

Since the discovery of multi-walled and single-walled carbon nanotubes, many research groups all over the world have incorporated these carbon based compounds into different materials and studied the interaction between the carbon nanotubes (CNTs) and the matrix, as well as the enhancement in physical/chemical properties of these composites. PVDF is of no exception. The enhancement of the β phase in solution-cast films of PVDF and PVDF-based copolymers through blending them with CNTs was first reported by Carroll's group [18]. They also demonstrated enhanced electroactive responses, especially the piezoelectric responses of the nanocomposites over that of the neat polymers. Electrospinning of PVDF/CNTs was also attempted but the work was focused on the electrical conductivity of the nanofibers without addressing their polymorphic behaviors [93].

As electrospinning as well as the incorporation of CNTs can both promote the enhancement of the β-phase in PVDF, it is worthwhile to study the crystallization behavior of such PVDF/CNT composite fibers. It is known that the electrospinning process can induce preferential alignment of CNTs in the electrospun fibers, as well as the molecular chains of

PVDF along the axis of the nanofibers [88]. Thus, it is important to clarify whether this cooperative orientation together with the resultant interfacial interactions would lead to a synergistic β-phase promoting effect or a significant change in the in the orientation of the various crystalline phases. Additionally, the surface chemistry of the SWCNT in junction with the interaction with PVDF molecular chains has also yet to be clarified. To address these issues, this work was undertaken to investigate the influences of CNTs on polymorphism and crystal orientation of electrospun P(VDF-HFP)/CNTs. In particular, the effects of CNTs, with different thickness and different surface chemistry are examined and compared to reveal the underlying mechanism.

4.2 Experimental procedures

Materials P(VDF-HFP) powder (Solef 11008, M_w = 115 000) was used as received. *N*,*N*-Dimethylformamide (DMF), acetone, triethylamine and acetyl chloride were supplied by Aldrich. Dry tetrahydrofuran was purchased from Acros Chemical Co. and freshly distilled utlizing sodium/benzophenone. Surface-oxidised SWCNTs and MWCNTs, both with about 3.5 wt.% hydroxyl groups were supplied by Chengdu Institute of Organic Chemistry, Chinese Academy of Sciences.

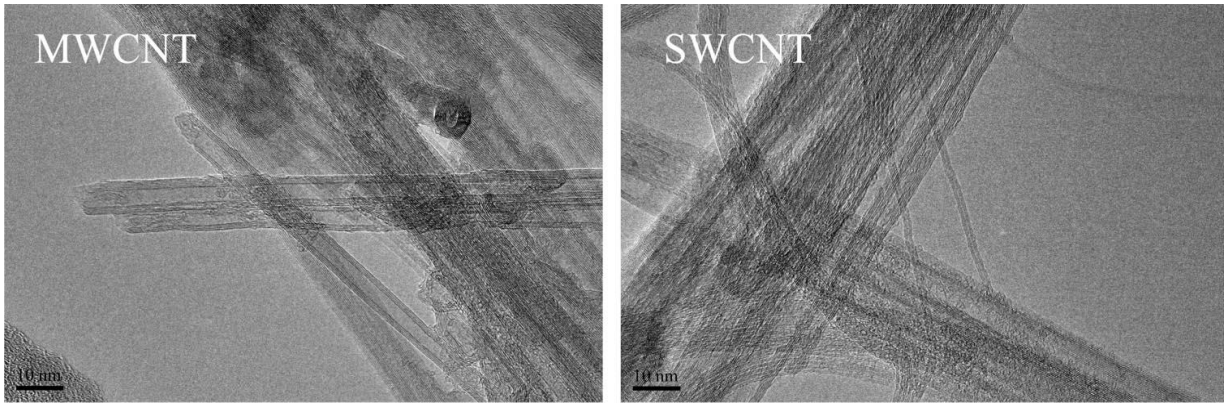

Figure 4.1 TEM images of the as-received CNTs as well as the SWCNTs.

SWCNT esterification treatment The reaction was conducted using the following reaction scheme shown in Figure 4.2. SWCNT-OH (60 mg), triethylamine (4.4 mL, 31 mmol), and dry THF (60 mL) were placed in a 150 mL round-bottomed flask and sonicated at for 30 minutes. After cooling to 0 °C, acetyl chloride (3.56 mL, 50 mmol) was added dropwise with vigorous stirring under a nitrogen atmosphere. The temperature was allowed to rise to 20 °C, and the reaction mixture was stirred overnight. Methanol was added into the suspension to remove the excess acetyl chloride, and esterified SWCNT-OH was precipitated in acetone. The solid was rinsed with ethanol and THF sufficiently and dried under vacuum at 40 °C.

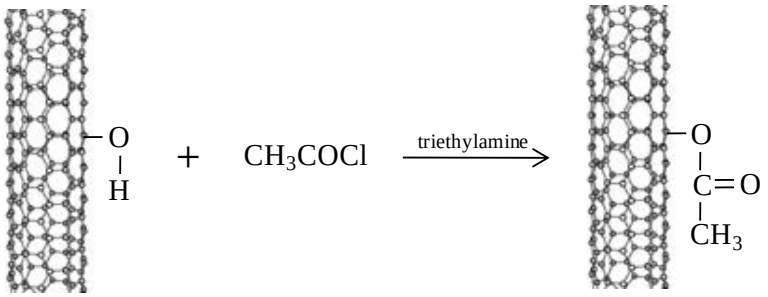

Figure 4.2 Reaction scheme to convert hydrolyzed CNTs to e-SWCNTs.

Electrospinning P(VDF-HFP) powder at the polymer/solvent ratio of 20/100 was dissolved in a DMF/acetone mixture at a DMF/acetone ration of 60/40. The different CNTs were dispersed in the P(VDF-HFP) solution respectively by sonication for half an hour and followed by continuous stirring for 2 days. The resulting P(VDF-HFP)/CNTs solutions were then drawn into a plastic syringe fitted with a needle with tip diameter of 200 μm and electrospun at a working voltage of 15 kV and a working distance of 15 cm. A syringe pump was used to provide a continuous feed of the polymer solution into the needle at a rate of 0.25 mL/hr. A modified rotating disk collector shown in Chapter 3 was utilized as the collector to collect the electrospun nanofibers due to the additional extension force it provides. Grounded indium tin oxide was fixed onto the collector to collect the electrospun fibers at a rotational speed of 1500 rpm for 4 hours. All thin films were dried in vacuo at room temperature prior to characterization.

Sample characterization Two-dimensional (2D) wide-angle X-ray diffraction (WAXD) patterns and Fourier transform infrared red (FTIR) spectra were collected using the instruments and conditions as reported in Chapter 3. To study the polymorphism of the nanofibers, the azimuthal average intensity was determined from the 2D WAXD patterns using the GADDS software package to obtain intensity versus 2θ plots. To assess the extent of orientation, the radial average intensities of the 2D WAXD patterns in the 2θ range of 18-19°, 19-20°, 20-21°, and 21-23°, respectively, were determined to obtain intensity versus azimuthal angle plots. The nanofibers prepared by electrospinning as well as the CNTs were examined using a Philips CM 300 FEG transmission microscope by electrospinning directly or casted onto a copper grid with a holey carbon film. Raman spectra were collected using a confocal Raman microscope (Witec CRM200) in back-scattering configuration (Olympus 100X objective lens) equipped with a charge-coupled device (CCD). The wavelength of the excitation laser was 488 nm. CNT

bundles; size distribution was obtained by zeta potential nanosizer (Malvern nanosizer). The thermogravimetric analysis (TGA) was performed on a TA Instrument TGA Q500 where the samples were heated at 10 °C/min from RT to 800 °C in nitrogen.

4.3 Results and discussions

4.3.1 Effect of CNTs with similar surface chemistry but different diameter

WAXD patterns and FTIR spectra of the electrospun fibrous thin films are shown in Figure 4.3. For the neat P(VDF-HFP) (curve i in Figure 4.3a), a strong diffraction peak at 2θ = 20.1°, which corresponds to (110) reflection of the α phase and (200)/(110) reflections of the β phase, and distinctive peaks at the 2θ values of 18.5° and 27.4°, which correspond to 020 and 021 reflections of the α phase, respectively, indicate the coexistence of the α and β phases. In addition, a shoulder peak appears on the equator at the 2θ value of about 22°, which also corresponds to the (200)/(110) reflections of the β phase. Its appearance at a slightly higher angle than usual may be attributed to the β-form extended-chain crystals formed under high tensile stress exerted by the rotating disk and separate electrodes, as the stress may lead to slightly reduced interchain distance. For the nanocomposite with 0.01 wt % MWCNTs (curve ii in Figure 4.3a), it is obvious that the strongest peak is broadened toward the high-angle side, while the peak at 2θ = 27.4° is weakened compared with that of the neat P(VDF-HFP), indicating that the α phase is suppressed while the β phase is slightly enhanced with the incorporation of the MWCNTs.

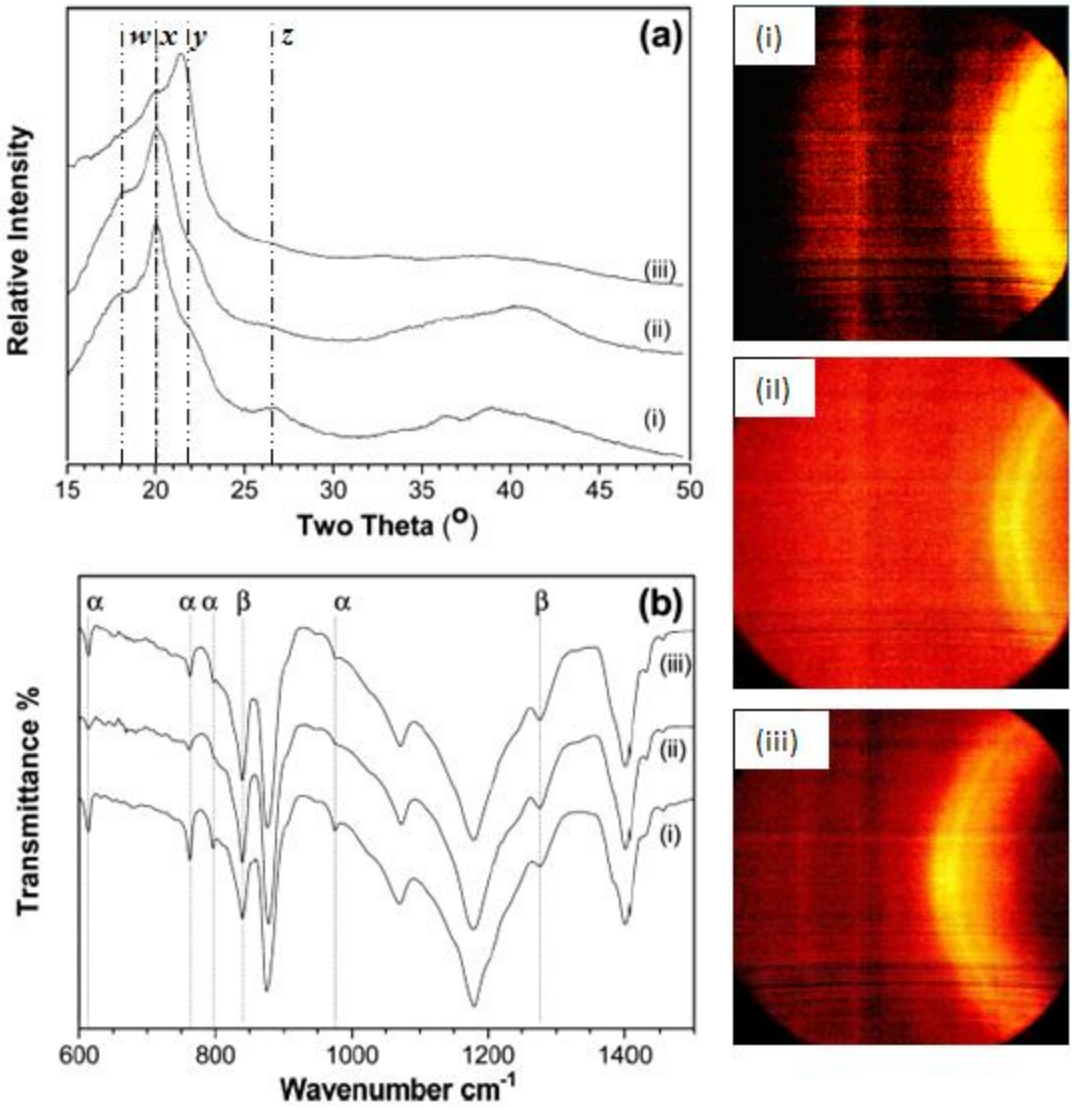

Figure 4.3 ***(a) WAXD patterns and (b) FTIR spectra of electrospun P(VDF-HFP)/ SWCNT thin films with CNT concentrations of (i)P(VDF-HFP), (ii) P(VDF-HFP)/MWCNT and (iii) P(VDF-HFP)/SWCNT. The CNT concentration is 0.01 wt.% for (ii) and (iii). The intensities of the FTIR bands have been normalized using the intensity of the band at 1070 cm^{-1} as a reference. w denotes the (020) reflection of the α-phase, x denotes the sum of the (021) reflection of the α-phase and (200)/(110) reflections of the β-phase, y denotes (200)/(110) reflections of the β-phase with reduced interchain distance and z denotes*** *(111)* ***reflections of the α-phase.***

This is corroborated by the FTIR spectrum of the P(VDF-HFP)/MWCNT (curve ii in Figure 4.3b) where the α-phase related bands at 614, 765, 795, and 975 cm^{-1} are weakened while the intensities of the β-phase related bands at 840 and 1278 cm^{-1} are increased over that of the neat P(VDF-HFP) [15]. However, the shoulder diffraction peak at $2\theta = 22°$ seems slightly weakened, which implies that the crystal orientation is slightly disturbed by the MWCNTs. It is striking to see that, for the nanocomposite with 0.01 wt% SWCNTs, the strongest diffraction peak appears at $2\theta = 21.5°$ (curve iii in Figure 4.3a), overriding the peak at 20.1°, which signifies that the β-form extended-chain crystals become dominant. It has been reported that SWCNTs can be better aligned along the fiber axis than MWCNTs in electrospun nanofibers due to the better regularity of the former and hence SWCNTs do not reduce the degree of orientation of polymer chains in electrospun nanofibers [95,96]. The unique crystalline structure of the P(VDF-HFP)/SWCNT thus may arise from the cooperative orientation of the SWCNTs and P(VDF-HFP) chains along the fiber axis, which facilitates the nucleation of highly oriented β-form extended-chain crystallites at the interface, as illustrated in Figure 4.4.

The FTIR spectrum of the P(VDF-HFP)/SWCNT (curve iii in Figure 4.3b) resembles that of the P(VDF-HFP)/MWCNT except that the α-phase bands are slightly stronger than that of the P(VDF-HFP)/MWCNT. As WAXD reflects the development of long-range order, whereas FTIR measures local conformational changes only [97], the conformational change brought by the formation of the extended-chain crystals is probably too small to be detected by FTIR. The slight α-phase enhancement is caused by the better chain orientation in the P(VDF-HFP)/SWCNT.

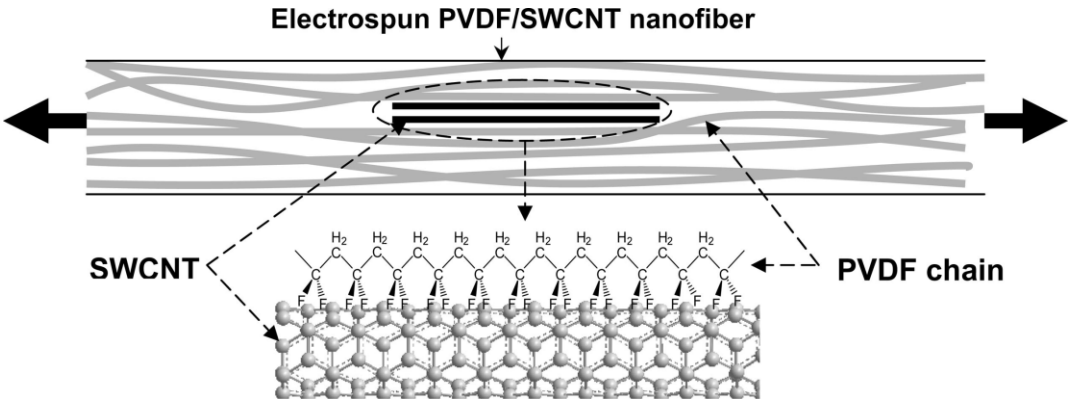

Figure 4.4 ***A schematic showing the proposed mechanism for the formation of β-form extended-chain crystallites in the electrospun P(VDF-HFP)/CNT composite fibers when both CNTs and P(VDF-HFP) chains are aligned along the fiber axis by the extensional forces resulting from the interaction between the π electrons on the CNTs' surface to the electron-withdrawing fluorine of P(VDF-HFP).***

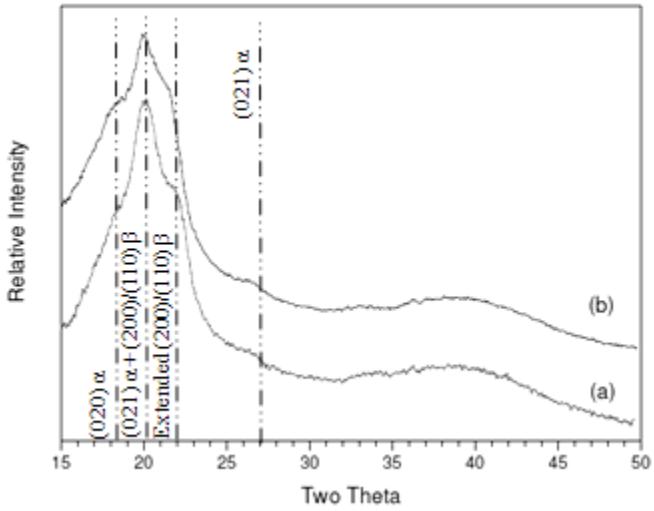

Figure 4.5 ***WAXD patterns of the aligned electrospun fibrous thin films of (a) P(VDF-HFP)/MWCNT and (b) P(VDF-HFP)/SWCNT. The CNT concentration is 0.1 wt.%.***

It is worth noting that the drastic change in crystalline structures of P(VDF-HFP) reported above is brought by the addition of 0.01 wt % SWCNT. When the CNT concentration is increased to 0.1 wt %, the trend is preserved, although the difference between the P(VDF-HFP)/SWCNT and P(VDF-HFP)/MWCNT nanofibers becomes smaller (Figure 4.5).

In contrast to the electrospun fibers, for the spin-coated P(VDF-HFP)/SWCNT thin films, the effect of SWCNT is insignificant in the whole range of concentrations studied. Figure 4.6 shows the WAXD patterns and FTIR spectra of the spin-coated P(VDF-HFP)/SWCNT thin films. As the SWCNT concentration increases, the α phase is increasingly suppressed. This can be seen from the weakening of the α-phase related diffraction peaks and infrared bands. The formation of the β phase is, however, only promoted slightly at relatively high SWCNT concentrations, as evidenced by the slight broadening of the strongest diffraction peak at 2θ = 20.5° towards the high angle side and the slightly enhanced β-phase infrared band at 1278 cm^{-1}.

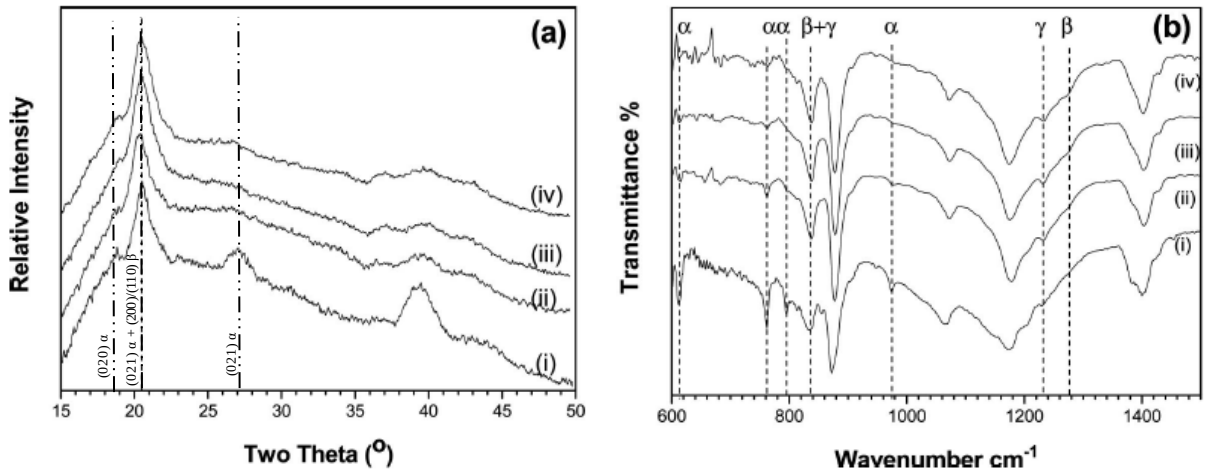

Figure 4.6 (a) WAXD patterns and (b) FTIR spectra of spin-coated P(VDF-HFP)/ SWCNT thin films with CNT concentrations of (i) 0 wt %, (ii) 0.01 wt %, (iii) 0.1 wt %, and (iv) 0.5 wt %. The intensities of the FTIR bands have been normalized using the intensity of the band at 1070 cm-1 as a reference.

The comparison between the spin-coated and electrospun samples thus reveals that the incorporation of SWCNT and the application of extensional forces indeed have a strong synergistic effect on crystalline structures of P(VDF-HFP). The WAXD patterns and FTIR spectra of the spin-coated P(VDF-HFP)/MWCNT thin films show a trend similar to that of the spin-coated P(VDF-HFP)/ SWCNT (Figure 4.7). This indicates that, without the extensional force, the role played by the SWCNTs and MWCNTs are the same; both of them interact with P(VDF-HFP), resulting in a slight β-phase enhancement at relatively high CNT concentrations.

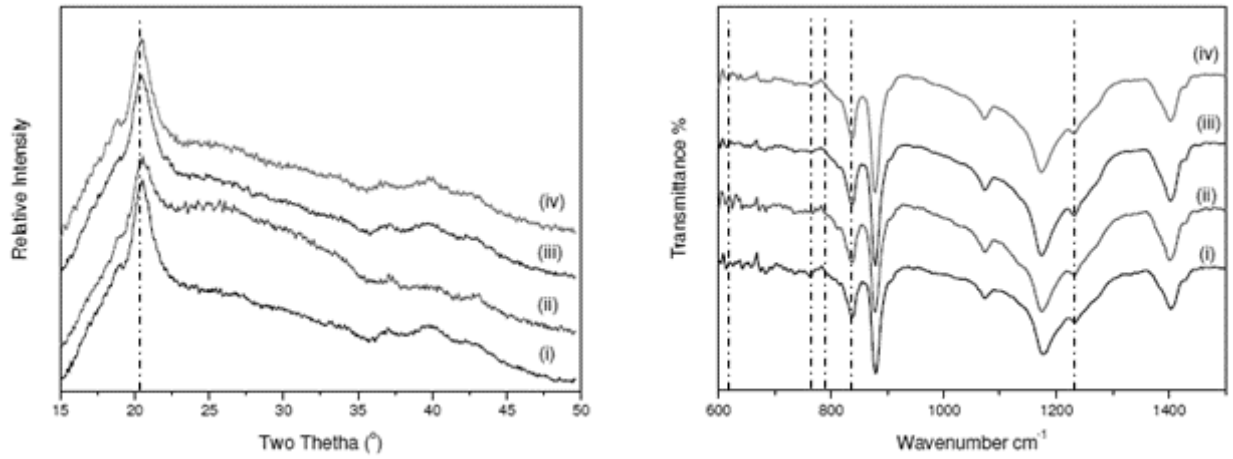

Figure 4.7 (a) WAXD patterns and (b) FTIR spectra of spin-coated P(VDF-HFP)/MWCNT thin films with CNT concentration of (i) 0.001 wt.%, (ii) 0.01 wt.%, (iii) 0.1 wt.% and (iv) 0.5 wt.%

A more detailed analysis of the orientation states of the crystallites in the P(VDF-HFP), P(VDF-HFP)/MWCNT, and P(VDF-HFP)/SWCNT electrospun fibers is presented in Figure 4.8, in which the radial average WAXD intensity versus azimuthal angle plots in four different 2θ regions, i.e., 18°-19° (I), 19°-20° (II), 20°-21° (III), and 21°-23° (IV), are compared.

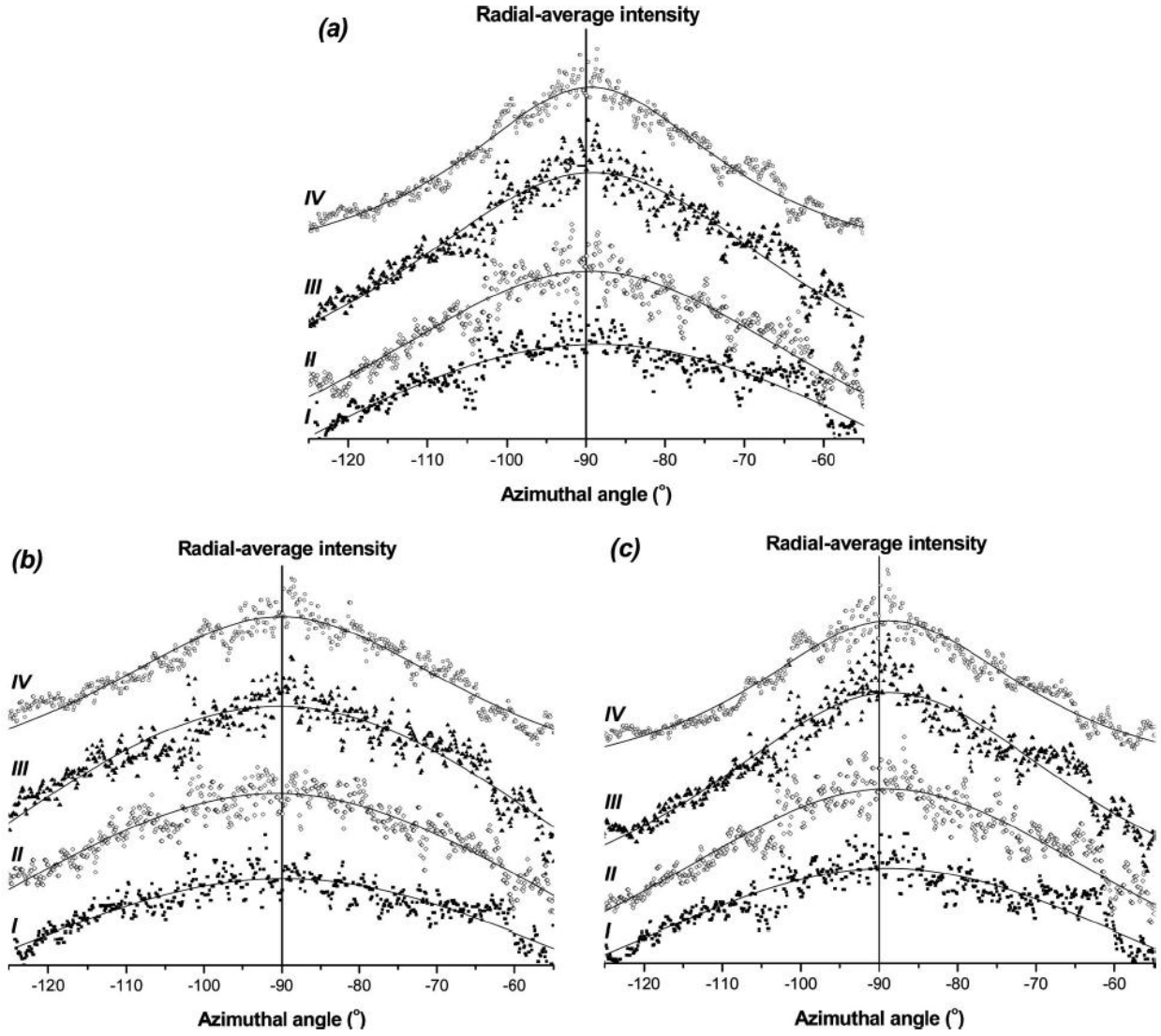

Figure 4.8 WAXD intensity versus azimuthal angle plots for the equatorial reflections of (a) P(VDF-HFP), (b) P(VDF-HFP)/MWCNT, and (c) P(VDF-HFP)/SWCNT. Curves I, II, III, and IV are radial-average intensities in the 2θ ranges of 18-19°, 19-20°, 20-21° and 21-23°, respectively. The solid lines are Lorentzian fitting curves. The CNT concentration is 0.01 wt % for (b) and (c).

The intensities in regions I and II are mainly from the R-form crystallites (reflections 100, 020, and 110), while the intensities in regions III and IV are mainly contributed by the β-form crystallites (reflections 110 and 200). For the neat PVDF (Figure 4.8a), it is obvious that the peaks in regions III and IV are sharper than those in regions I and II, indicating that the β phase has a higher degree of orientation than the α phase. This observation is consistent with our previous results [10]. Furthermore, the peak in region IV is sharper than that in region III, which supports the claim that region IV corresponds to the highly oriented β-form crystallites formed under extensional force.

From Figure 4.8, it is also clear that the degree of crystal orientation of the P(VDF-HFP)/MWCNT is generally lower than that of the neat P(VDF-HFP), which confirms the detrimental effect of the MWCNT on the preferred orientation of P(VDF-HFP) chains. Figure 4.9 shows a TEM image of an electrospun P(VDF-HFP)/MWCNT nanofiber with a CNT concentration of 0.1 wt %. It is evident that some MWCNTs are well aligned along the fiber axis while most MWCNTs form agglomerates or exhibit entangled conformation. Similar results have been reported for electrospun PEO/MWCNT nanofibers with a higher CNT concentration and the phenomenon been attributed to the irregularity of the MWCNTs [95]. Although we were unable to observe the MWCNTs in the nanofibers containing 0.01 wt % CNTs, it is reasonable to deduce that the irregularity of the MWCNTs would still lead to their entanglement, which justifies the poorer orientation of the P(VDF-HFP) crystals in the P(VDF-HFP)/MWCNT nanofibers detected at the extremely low CNT concentration of 0.01 wt %.

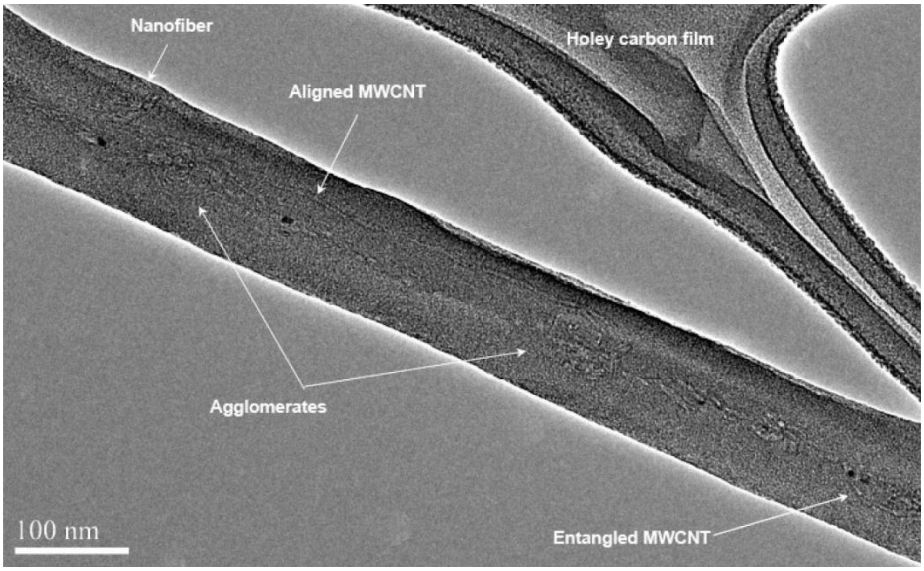

Figure 4.9 A TEM image showing both oriented and entangled MWCNT in a P(VDF-HFP)/MWCNT nanofiber. The CNT concentration is 0.1 wt %.

In contrast to the P(VDF-HFP)/MWCNT, the degree of crystal orientation of the P(VDF-HFP)/SWCNT nanofibers is close to that of the P(VDF-HFP) nanofibers, as shown in Figure 4.6. This is also consistent with the observation from electrospun PEO/SWCNT with a much higher CNT concentration [95]. Because of the small diameter of SWCNTs and the very low CNT concentrations of the samples, we were unable to observe SWCNTs in the nanofibers via TEM. Nevertheless, the higher degree of crystal orientation of the P(VDF-HFP)/SWCNT than that of the P(VDF-HFP)/MWCNT implies that the SWCNTs may be better aligned than the MWCNTs in the nanofibers. Furthermore, the degree of orientation of the P(VDF-HFP) crystals is quantitatively evaluated by measuring the full width at half-maximum (FWHM) of the Lorentzian fitting curves of the azimuthal plots. The data are presented in Table 4.1. It can be seen that, although the errors for broad peaks are fairly large because the data points only cover a small portion of the Lorentz peaks, the fwhm values obtained for the region IV are fairly reliable.

The fact that the degree of crystal orientation of the P(VDF-HFP)/SWCNT is slightly lower than that of the neat P(VDF-HFP) nanofibers in region IV implies that the formation of the highly oriented β-form crystals is not purely dependent on the overall chain orientation. Instead, the likely mechanism is that the corporative orientation of the SWCNT and P(VDF-HFP) chains facilitates the nucleation of the β-form crystals whose *c* axis is parallel to the SWCNT and nanofiber axis.

Table 4.1 FWHM of the Lorentzian Fitting Curves of the WAXD Azimuthal Plots

	FWHM (deg) (R^2)			
Electrospun Sample	region I (18 - 19°)	region II (19 - 20°)	region III (20 - 21°)	region IV (21 - 23°)
PVDF	100 ± 19 (0.67)	74 ± 5 (0.87)	50 ± 3 (0.89)	39 ± 1 (0.96)
PVDF/MWCNT	126 ± 34 (0.68)	101 ± 11 (0.84)	81 ± 7(0.81)	54 ± 2 (0.92)
PVDF/SWCNT	109 ± 6 (0.90)	84 ± 3 (0.94)	61 ± 2(0.94)	44 ± 1 (0.96)

The interfacial interactions between P(VDF-HFP) and CNTs are probed using Raman spectroscopy. When the concentration of the CNTs is 0.1 wt %, both the tangential mode (G band) and disorder-induced band (D band) can be clearly observed from the electrospun composite fibrous thin films, while only a very weak G band can be seen from the spin-coated P(VDF-HFP)/SWCNT sample (Figure 4.10). The much higher G band intensities of the electrospun samples than their spin-coated counterparts may be attributed to the better alignment of the CNTs along the surface of the electrospun fibrous thin films. The frequencies of the G band are shifted upward from 1577 cm^{-1} and 1581 cm^{-1} for the as-received MWCNTs and SWCNTs, respectively, to 1590 cm^{-1} for both the electrospun and spin-coated nanocomposite samples. This indicates that the interfacial interactions in the electrospun and spin-coated nanocomposite samples are essentially of the same nature, i.e., a charge-transfer type of

interaction between the CNTs and the electron-withdrawing fluorine atoms on the PVDF chains [98].

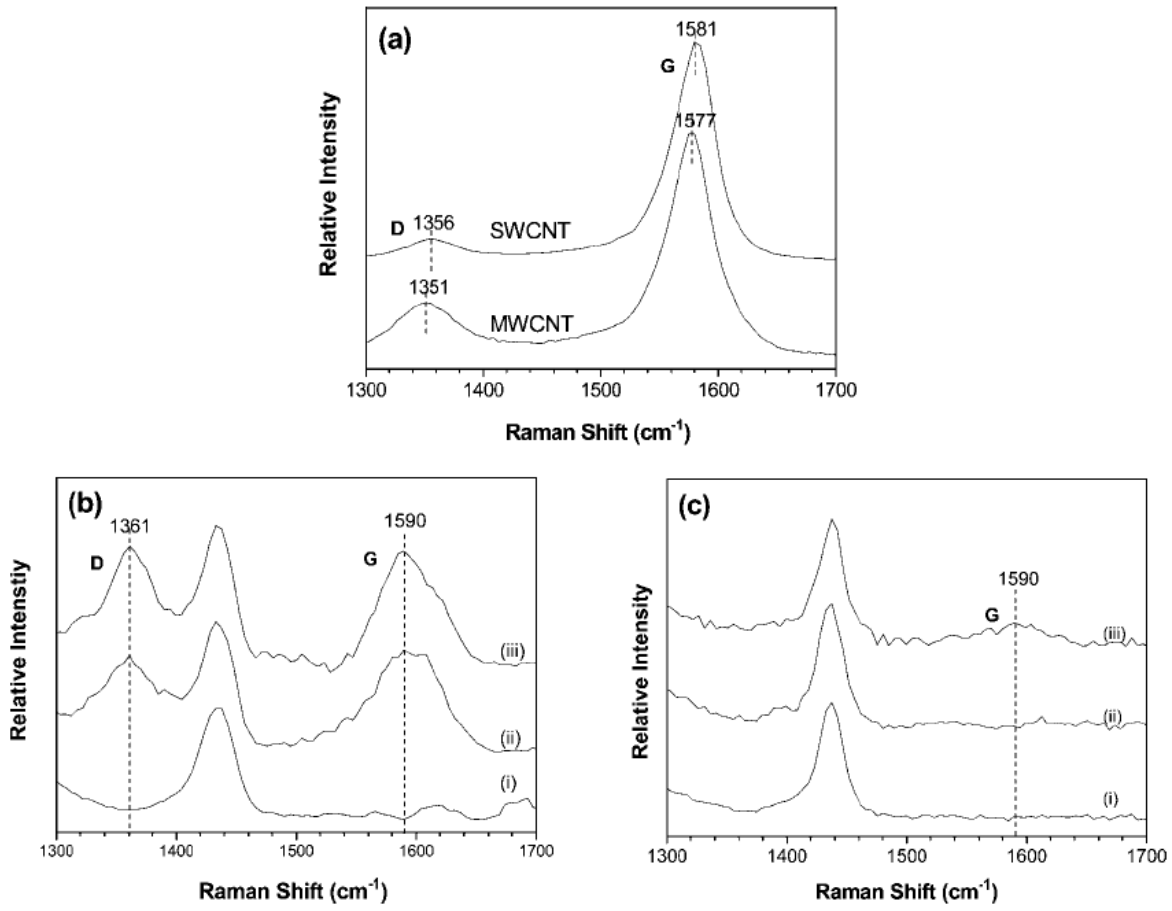

Figure 4.10 Raman spectra of (a) the CNTs, (b) the electrospun fibrous thin films, and (c) the spin-coated thin films of (i) P(VDF-HFP), (ii) P(VDF-HFP)/MWCNT, and (iii) P(VDF-HFP)/SWCNT. The CNT concentration is 0.1 wt % for (b) and (c).

It is also noticed that, accompanied by the upshifts, the intensity ratios of the G band to the D band (G/D ratios) for the electrospun samples are also greatly reduced as compared with the as-received CNTs. Furthermore, although the G/D ratio of the as-received SWCNTs is larger than that of the as-received MWCNTs, the G/D ratio of the electrospun P(VDF-HFP)/SWCNT is

slightly smaller than that of the electrospun P(VDF-HFP)/MWCNT. A few studies on electrospun polymer/CNT nanocomposites have shown that electrospinning process itself does not severely alter the G/D ratios [99,100]. The sonication process is also unlikely to be the major cause for the drastic change in the G/D ratio which is demonstrated in figure 4.11. When polystyrene grafted SWCNT was added into P(VDF-HFP) at the same concentration and undergoing through the sample preparation via sonication for extended periods of time prior to spin-coating and electrospinning, there is no drastic change in the G/D ratio when made into either thin films or the nanofiber form via electrospining. Thus, this shows that the drastic change in the G/D ratio for the electrospun sample is not caused by the sonication process as the spincoated sample has gone through the same process. The change in the G/D ratio may thus be associated with an intensity decrease of the Breit-Wigner-Fano (BWF) feature as a consequence of the decrease in electronic density of metallic CNTs caused by the strong donor-accepter interaction between the CNTs and fluorine at the interfaces [101]. The large drop in the G/D ratio for the electrospun P(VDF-HFP)/SWCNT may signify more extensive interfacial interactions. The phenomenon, however, needs to be further investigated to verify the hypothesis.

In addition to their difference in diameter and surface defects, the SWCNTs and MWCNTs may have different electrical conductivities that may also influence their alignment in the electrospun nanofibers. To address this issue, the electrical conductivities of the PVDF/CNT solutions were measured, and the results are presented in Table 4.2. It shows that the electrical conductivities of the PVDF/SWCNT solutions are only marginally higher than those of the PVDF/MWCNT solutions. Thus the higher electrical conductivity of the PVDF/SWCNT solution is unlikely to be responsible for the higher degree of crystal orientation found for the PVDF/SWCNT nanofibers. However, the possibility that the electrical conductivity may play a significant role in semisolid state cannot be excluded, which needs to be investigated further.

Additionally, the difference in the surface area of the SWCNTs and MWCNTs may also play a role in enhancing the interaction between CNTs and P(VDf-HFP) molecular chains. It is expected that the quality, aspect-ratio, and surface functionalization of SWCNTs as well as their dispersion method would also affect the induced crystalline structures significantly, which is a subject for further studies.

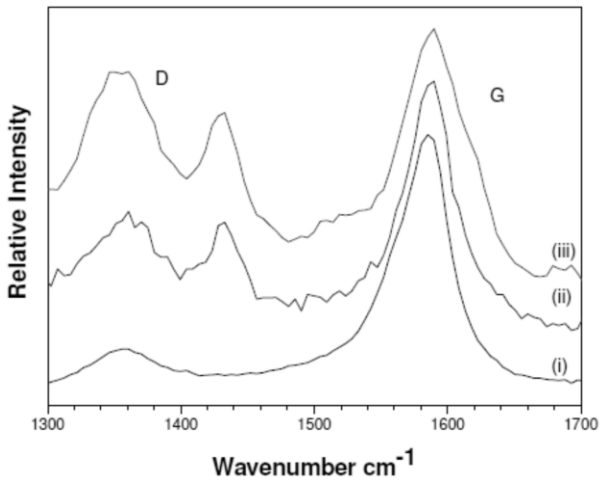

Figure 4.11 Raman spectra of (i) polystyrene-grafted SWCNT (SWCNT-PS; the content of the grafted PS is about 47 wt.%), (ii) spin-coated PVDF/SWCNT-PS thin film and (iii) electrospun PVDF/SWCNT-PS fibrous thin film. The concentration of the SWCNT-PS is 0.1 wt.% in (ii) and (iii).

Table 4.2 Electrical Conductivity of the P(VDF-HFP)/CNT Solutions

	electrical conductivity (μS/cm)		
sample	0.0 wt. % (neat PVDF)	0.01 wt. %	0.1wt.%
PVDF/SWCNT	2.60	7.02	6.00
PVDF/MWCNT		6.21	4.80

4.3.2 Effect of SWCNT surface chemistry on polymorphism of P(VDF-HFP)

In order to study the effect of surface chemistry of the SWCNTs' on the polymorphism of P(VDF-HFP), the same hydrolyzed SWCNTs' used in section 4.3.1 was used for the esterification process to cap the hydroxyl group and reduce the influence of the hydroxyl group on the molecular chains of P(VDF-HFP). The esterified SWCNTs (e-SWCNTs) was synthesized from the hydrolyzed SWCNTs (h-SWCNTs) using the following reaction (Figure 4.2).

The esterification process of the CNTs was performed successfully as verified by TGA and FTIR analysis (Figure 4.12). It can be clearly observed that when both types of SWCNTs undergo pyrolysis in an inert environment, the e-SWCNTs will lose more weight as compared to the h-SWCNTs due to the larger ester group than the hydroxyl group. The mass ratio of the ester group to hydroxyl group is about 3.47%. For h-SWCNTs, a sharper weight loss starts at about 685°C, which corresponds to the end of OH group degradation region and the onset of CNT degradation region. The corresponding weight loss of the h-SWCNTs at this point is about 3.5 wt%, which is consistent with the information provided by the supplier, whereas the corresponding weight loss for e-SWCNTs is about 6.0 wt%, which is roughly 0.68 times of that of h-SWCNTs. This shows that most hydroxyl groups have been partially converted to ester. In addition, a band at 1733 cm^{-1} related to the C = O stretching of the ester group can be detected from the FTIR spectrum of the e-SWCNT, whereas it is absent in the spectrum of the h-SWCNTs (Figure 4.2B). A band at 738 cm^{-1} can also be observed which can be attributed to the rocking vibrations of C-H. From these results, we can confirm that the esterification process conducted to the h-SWCNTs is successful.

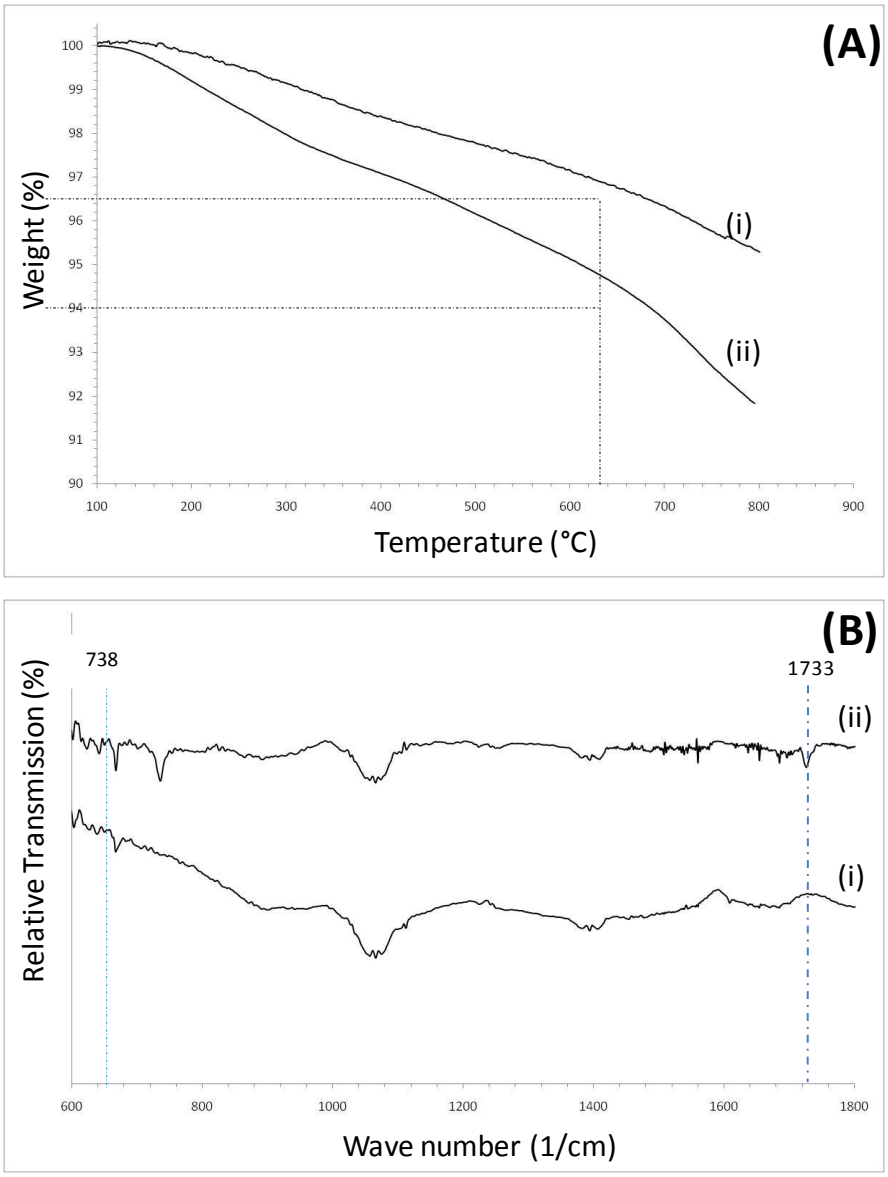

Figure 4.12 (A) TGA and (B) FTIR spectra of (i) h-SWCNTs and (ii) e-SWCNTs.

A very low concentration of the h-SWCNTs and e-SWCNT was added into P(VDF-HFP) with the resulting polymer solutions electrospun into nanofibrous mats. The WAXD patterns and FTIR spectra of the electrospun P(VDF-HFP) and P(VDF-HFP)/CNTs nanocomposites are shown in Figure 4.13. For electrospun P(VDF-HFP) (Figure 4.13A (i)), a dominant peak at 20.1°

two theta, corresponding to the (110) reflection of the α phase and (200)/(110) reflections of the β phase, as well as peaks at 18.5°, 27.4° two theta, corresponding to the (020) and (021) reflections of the α phase, indicates the co-existence of α and β phases. Additionally, a shoulder peak at about 22° two theta, corresponding to the (200)/(110) reflections of the β phase, can be attributed to the formation of highly extended β crystallites due to the use of the modified rotating disk collector [88,98]. For electrospun P(VDF-HFP)/e-SWCNTs nanocomposites (Figure 4.13A (ii)), it can be clearly observed that the dominant peak at 20.1° two theta is broadened towards the high angle side while distinctive peaks at 27.4° two theta become significantly weaker when compared with that of pure P(VDF-HFP). This indicates that by the addition of e-SWCNTs into P(VDF-HFP) and electrospinning, the α phase became suppressed while the β phase is enhanced. The result is corroborated by the FTIR spectrum for electrospun P(VDF-HFP)/e-SWCNTs (Figure 4.13B (ii)) where the α-related peaks at 614, 765 and 975 cm^{-1} are weakened whereas an increase in intensity of the β-related peak at 840 and 1278 cm^{-1} are observed when compared with that of the neat P(VDF-HFP). However, when h-SWCNTs was added into P(VDF-HFP), there is a further suppression of the α phase and increase in the β phase, evidenced by the further decrease of the α-related peaks and the increase in the β-related peaks in both WAXD pattern and FTIR spectra (Figure 4.13A and 4.13B (iii)). Furthermore, the shoulder peak at about 22° two theta has higher intensity, becoming the most prominent peak. This clearly indicates that by adding h-SWCNTs in P(VDF-HFP) and collecting using the modified rotating disk, the synergistic cooperation of the extra stretching force and the interfacial interactions between P(VDF-HFP) and the h-SWCNTs encourages the growth of these highly extended β crystallites while suppressing the growth of the α phase. However, it is important to note that WAXD reflects the long range order while FTIR measures the local conformations of the

molecular chain, rendering FTIR unable to differentiate between the normal and highly extended β-crystallites [12].

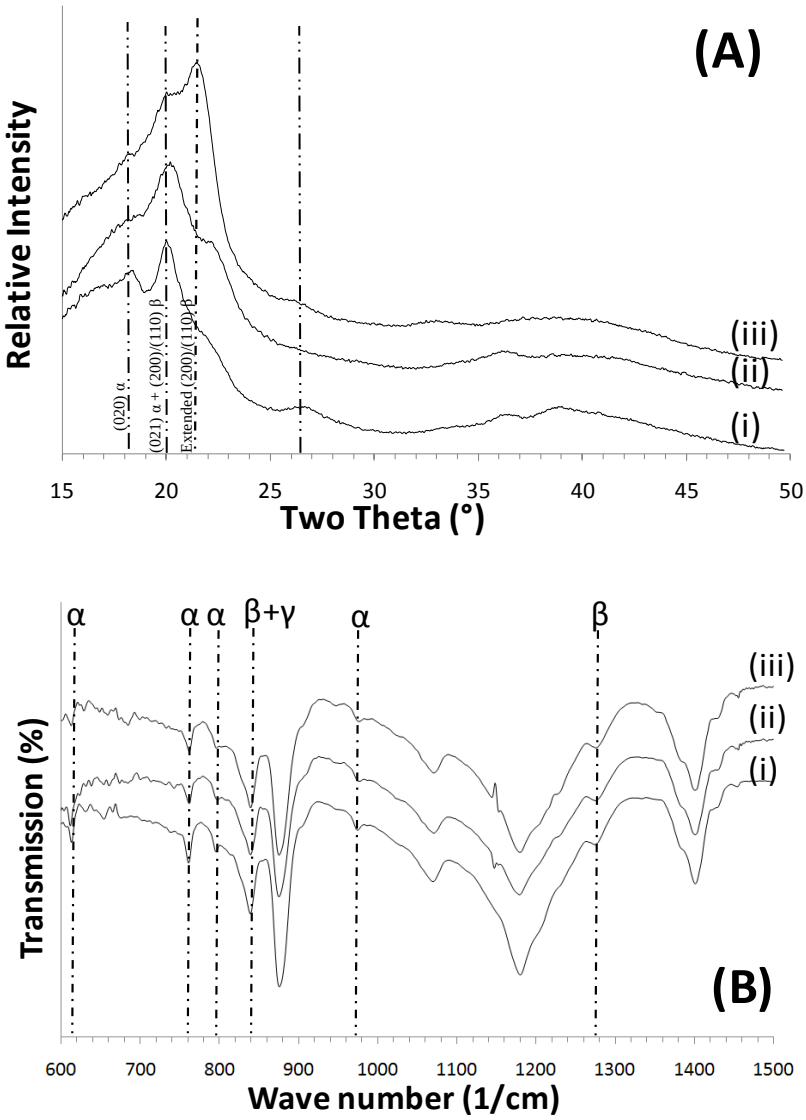

Figure 4.13 (A) WAXD patterns and (B) FTIR spectra of aligned electrospun fibrous films of (i) PVDF, (ii) PVDF/e-SWCNT and (iii) PVDF/h-SWCNT. The CNT concentration is 0.01 wt.% for (ii) and (iii).

The main difference between the two different CNT samples is in its functional groups. The hydroxyl groups may be able to form hydrogen bonds with P(VDF-HFP) while ester groups definitely do not. To study the effect of surface functional groups on hydrogen bonding capability, both types of SWCNTs were dispersed in water to observe the stability of the two different SWCNT suspensions. Based on the amount of CNTs that has settled, it can be clearly observed that the e-SWCNTs can be better dispersed in water as compared to its h-SWCNTs counterpart (Figure 4.14). This is most probably due to the formation of h-SWCNT bundles resulting from the strong hydrogen bonding forces available from the attached hydroxyl functional groups. Once these hydroxyl functional groups are esterified, the hydrogen bonding between CNTs is diminished, resulting in a more stable dispersion in water as water molecules can form hydrogen bonds with easter groups.

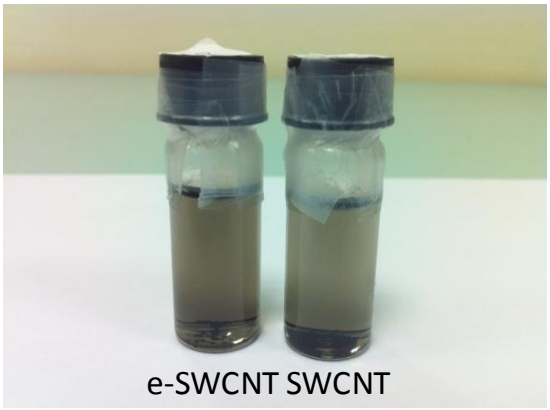

Figure 4.14 Dispersion of h-SWCNT and e-SWCNT in water.

CNTs were also dispersed in DMF, which is the main solvent used to dissolve P(VDF-HFP). When dispersed in DMF, it can be observed that the dispersion is fairly similar for both types of

CNTs. This is further corroborated from the light scattering result (Figure 4.15) where similar sized bundles of CNTs can be observed for both samples when dispersed in DMF.

As electrospinning is a process that helps to align CNTs in the nanofibers [95], the initial dispersion of the CNTs in the polymer solution is critical as the formation of the highly extended β phase and the resultant molecular alignment is both dependent on the quality of the CNT alignment in the nanofiber as well as the degree of dispersion of the CNTs in the polymer solution [103]. Since the dispersion states of both CNT samples in DMF are similar, the different crystallization behavior observed from the electrospun samples are unlikely to be caused the dispersion states of the CNTs in P(VDF-HFP).

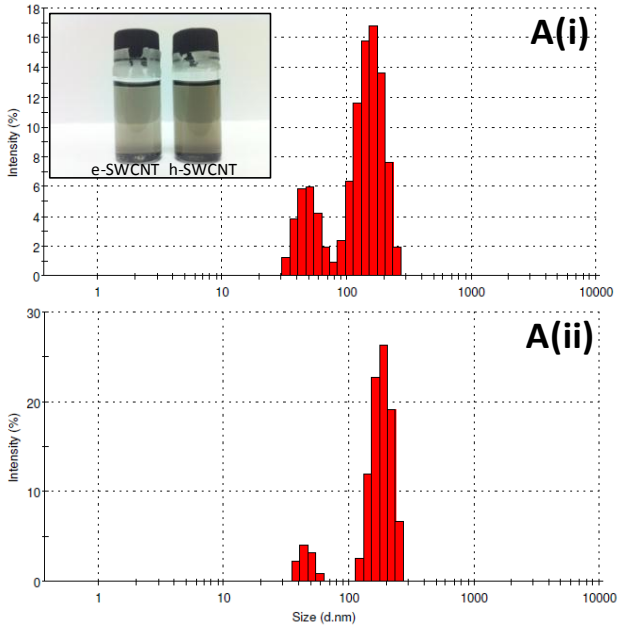

Figure 4.15 (A) shows the size distribution of the CNTs bundles form by (i) h-SWCNTs and (ii) e-SWCNTs in DMF. The concentration of CNTs used is 0.25 mg/ml. The insert shows the dispersion of the CNTs in DMF.

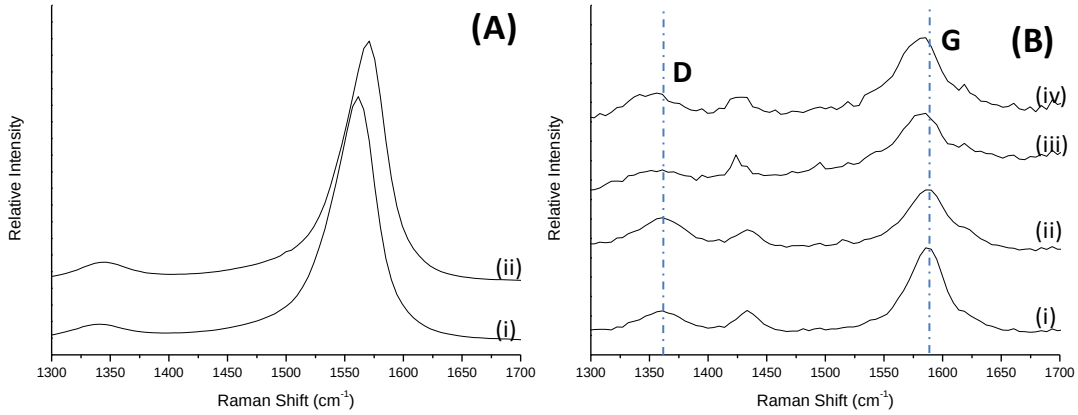

Figure 4.16 Raman spectra of (A) the CNTs, (i) e-SWCNT, (ii) h-SWCNT and (B) aligned membranes of electrospun (i) P(VDF-HFP)/e-SWCNT and (ii) P(VDF-HFP)/h-SWCNT nanofibers. Random electrospun non-woven mats of (iii) P(VDF-HFP)/e-SWCNT and (iv) P(VDF-HFP)/h-SWCNT are also presented in (B). The CNT concentration for electrospun P(VDF-HFP)/CNTS is 0.1 wt.%.

Raman spectroscopy (Figure 4.16) can help us to probe the interfacial interactions of the different SWCNTs with the P(VDF-HFP) matrix in electrospun nanofibers. To obtain reliable signals from the Raman spectroscopy, 0.1 wt.% of CNTs (both hydrolyzed and esterified SWCNTs) was added into P(VDF-HFP) and electrospun into aligned nanofibrous films utilizing the modified rotating disk [104] mentioned in chapter 3 as well as into random non-woven mats. When the concentration of the SWCNTs is at 0.1 wt.%, both the tangential mode (G band) and disorder-induced band (D band) can be clearly observed in both random and aligned mats of electrospun P(VDF-HFP)/CNT. The frequencies of the G band are shifted upward from 1570 cm^{-1} and 1560 cm^{-1} for the as-received h-SWCNTs and the e-SWCNTs, respectively, to 1576 cm^{-1} for random mats of both SWCNTs and the e-SWCNTs. The upshift to the same frequency for the

two samples with different surface chemistry implies that the G band position of the SWCNTs in electrospun nanofibers may be dominated by the strain experienced by the SWCNTs [105]. The effect of the additional tensile strain that is brought about by the modified rotating disk collector to the different CNTs can also be clearly seen by a up-shift in the raman spectra for both P(VDF-HFP)/e-SWCNT and P(VDF-HFP)/h-SWCNT nanofibers [105] as compared to their random non-woven mat counterparts (Figure 4.16B(i) and (ii)) .

Although for both the random and aligned electrospun mats, P(VDF-HFP)/h-SWCNTs and P(VDF-HFP)/e-SWCNTs show similar G band positions, their intensity ratios of the G band to the D band (G/D ratios) are different. It can be clearly observed that there is a decrease in the G/D ratio of both types of SWCNTs when electrospun but the G/D ratio is significantly smaller for the h-SWCNTs as compared to its e-SWCNT counterpart when the nanofibers are collected by the modified rotating disk collector. As discussed earlier, the lower G/D ratio could be attributed to the strong donor-acceptor interactions between the CNTs and the fluorine in PVDF [101] that could result in the decrease in electronic density of the metallic CNTs. The above results indicate that such interactions are more sensitive to surface chemistry of the CNTs under a higher extensional force. The likely reason is that the hydrogen bonds in electrospun P(VDF-HFP)/h-SWCNT system allow a more effective strain transfer between the matrix and the SWCNTs and thus promote the crystallization of P(VDF-HFP) into the highly extended β-crystal form on the h-SWCNTs' surface when the system is effectively stretched, whereas the e-SWCNTs are unable to form hydrogen bonds with the matrix. Thus, it is this additional strain that brought about the growth of the highly extended β phase, leading to the enhanced interactions between the h-SWCNT and P(VDF-HFP).

4.4 Conclusion

The effects of CNT diameter (multi-walled vs. single-walled) and surface chemistry (h-SWCNT vs. e-SWCNT) on the polymorphic behavior and crystal orientation of the electrospun PVDF/CNTs composite fibers have been studied using WAXD, FTIR, TEM, and Raman spectroscopy. The results reveal that the interfacial interaction between the SWCNTs and PVDF and the extensional force experienced by the nanofibers can work synergistically to induce highly oriented β-form crystallites extensively at a very low SWCNT concentration. In contrast, the effect of the MWCNTs on crystal orientation is insignificant at this very low CNT concentration as a result of the detrimental effect of the MWCNTs on the preferred orientation of PVDF chains. The results also reveal that hydrogen bonding between the functional groups on the CNTs and PVDF may play a critical role in providing the interfacial forces necessary to allow effective stress transfer to the CNTs during nanofiber collection, allowing the crystallization of the highly oriented β-form crystallites. In contrast, the addition of e-SWCNTs, which has no hydrogen bonding capability, does not have such a significant impact on the formation of highly oriented β-form crystallites, although still providing similar crystal orientation.

5 Supercritical Carbon Dioxide Treatment of Electrospun PVDF and its Effects on Morphology, Polymorphism and Properties of PVDF

5.1 Introduction

When a substance is above its critical temperature (T_c) and critical pressure (P_c), it can easily effuse through solid like a gas while dissolving materials like a liquid, hence termed as a supercritical fluid (SCF) [109]. This unique property allows SCFs to be utilized as solvents, anti-solvents, plasticizers and even in polymer processing for the formation of microcellular foams [110]. One of the most commonly used SCF is supercritical carbon dioxide ($SCCO_2$). This is because it has many advantages like chemically inertness, inexpensive, non-flammability and environmental friendliness. Additionally, it can used to substitute organic solvents during chemical synthesis. However, the solubility of most polymers in $SCCO_2$ is normally quite low due to a lack of interaction between the carbon dioxide (CO_2) with the polymer and the low entropy force of mixing high molecular weight polymers with CO_2 [111]. Polymers with carbonyl groups, ether linkages or C-F linkages can have specific interactions with CO_2, allowing CO_2 to rapidly diffuse into both the crystalline and amorphous regions of the polymer. This leads to partial dissolution in the bulk polymer. The process normally causes a depression in the glass transition temperature (T_g), as well as having a plasticizing effect in the amorphous regions, leading to a reduction in the melting temperature [111]. It has also been demonstrated that $SCCO_2$ can be utilized to alter the polymorphic state of polymers. In the case of poly(4-methyl-a-

pentane), by including CO_2 in the pentane solvent during crystallization at high pressures, the polymorphic behavior changes from Form II to Form I [112]. Polymorphic changes induced by the treatment with $SCCO_2$ can also be observed in a mixture of atactic and syndiotactic polystyrene (PS). Under $SCCO_2$ conditions, it was found that the helical conformation is more favored than the all *trans* conformation [113] due to the plasticizing effect of CO_2.

Electrospun P(VDF-HFP) nanofibers have been shown to exhibit enhanced β-phase in Chapter 3 and the β-phase can be further enhanced by adding in CNTs as described in Chapter 4. In Chapter 3, it has also been shown that electrospun P(VDF-HFP) membranes are porous in nature and are not suitable to be used in the bulk form as electroactive materials. One technique to overcome this porosity problem is to make use of pressure and temperature to compress the fibrous film [114] which can also improve the mechanical properties of such membranes simultaneously. However, the use of heat will convert some of the β-phase into the α-phase as the latter is the more thermodynamically stable phase. An alternative high-pressure thermal treatment is the treatment with supercritical carbon dioxide ($SCCO_2$). As PVDF-based polymers consist of a C-F linkage per monomer, the interaction between PVDF and CO_2 under the supercritical state should be significant. In this work, by adopting a reverse-barrier technique, electrospun nanofibrous membranes were successfully treated with $SCCO_2$ for the first time. Herein the effects of the SCCO2 treatment on structures and morphology of the electrospun P(VDF-HFP) membranes are reported. The $SCCO_2$ treatment also greatly enhances fiber-to-fiber interconnectivity, resulting in a remarkable improvement in mechanical properties of the membranes. This enabled us to characterize properties/functionality of the treated membranes.

5.2 Experimental procedure

Materials. Poly(vinylidene difluoride-co-hexafluoropropylene) powder (Solef 11008) was used as received. 1-Butyl-3-methylimidazolium hexafluorophosphate ([BMIM]PF_6), *N*,*N*-dimethylformamide (DMF) and acetone were supplied by Sigma-Aldrich and used as received. The same surface-oxidized SWCNT with about 3.5 wt.% hydroxyl groups used in chapter 4 were utilized.

Electrospinning. The solution preparation and electrospinning conditions were the same as those reported in chapter 3 except that the electrospinning was conducted at 18 kV. A grounded aluminum foil acting as a substrate was located at a fixed distance of 15 cm from the needle tip to collect the nanofibers in random-mat form. The solutions were also spin-coated at 2000 rpm to make reference samples. All samples were dried in vacuum overnight prior to further treatment.

$SCCO_2$ treatment. All samples were clamped between two glass slides prior to the $SCCO_2$ treatment. The treatment was conducted in a self-fabricated high-pressure chamber at the pressure of 4000 psi and temperatures of (A) 40ºC, (B) 60ºC, (C) 80ºC, (D) 100ºC, (E) 120ºC and (F) 140ºC, respectively, for 30 minutes. The chamber was then cooled to room temperature at 4000 psi prior to the release of the gas and removal of the sample. The treatment was also conducted at 3000 psi and 100ºC in $SCCO_2$ and N_2 media, respectively. All samples were left to dry in air at room temperature for 24 hrs prior to characterization.

Characterization of the as-spun membranes. All samples were characterized via scanning electron microscopy (SEM), wide angle x-ray diffraction (WAXD), attenuated Fourier transform infrared (FTIR) spectroscopy and differential scanning calorimetry (DSC). The instruments and conditions for the characterization were the same as that reported in chapter 3. Surface morphology of the nanofibers was examined using a JEOL JSM 6340F field-emission scanning electron microscope (FESEM). Tensile properties of the membranes were tested using an Instron 5848 Micro Tester with a 10-N load cell at the cross-head speed of 15 mm/min. Dumbbell-shaped specimen with an overall length of 63.5 mm and gauge width of 3.18 mm were used.

Characterization of the IL-loaded membranes. [BMIM]PF_6 was loaded into the electrospun membranes by immersing the membranes in the IL for 7 days. The IL-loaded membranes were then placed onto a piece of cellulose paper and pressed by a 20-g weight to absorb excess IL. The retention rate of the IL was calculated using the following equation:

$$\text{Retention Rate} = (\text{Wet weight} - \text{Dry weight})/\text{Density of the IL}/\text{Dry weight} \quad (1)$$

where the density of the IL is 1.38 g/cm^3.[108] PVDF/IL gel electrolyte was prepared by mixing PVDF and the IL in the DMF/acetone mixture and then evaporating out the solvents. The ionic conductivities of the IL-loaded electrospun PVDF membranes and PVDF/IL gel were obtained from its AC impedance spectra. The samples were sandwiched between two pieces of polished stainless steel to form stainless steel/electrolyte/stainless steel block-type cell. The spectra were obtained on the Autolab PGSTAT302N potentiostat from 1M Hz to 100 Hz with the amplitude of 5 mV. The complex plane graph is a sloping line. The intercept of high frequency curve

crossing with the horizontal axis (real part) was taken as the bulk resistance.[109] The ionic conductivity was calculated using the following equation:

$$\sigma = L/R \bullet S \quad (2)$$

where L is the thickness of the electrolyte, S the area of the electrolyte and R the bulk resistance.

Characterization of the electroactive response of the $SCCO_2$ treated membranes. The piezoelectric device was fabricated by 2 steps. Firstly, electrodes were fabricated by thermally evaporating aluminum, onto a mask (rectangular electrode of 1.5 cm by 0.5 cm) secured onto a spincoated film of PVDF (2 cm by 2 cm) which was prepared using PVDF powder at the polymer/solvent ratio of 20/100 being dissolved in a DMF/acetone mixture at a DMF/acetone ration of 60/40 at 2000 rpm and annealed at 120°C for 4 hours. Subsequently, 2 pieces of spincoated PVDF films with electrodes were used to sandwich the electrospun membranes and treated with $SCCO_2$ with the same conditions in ref [117]. Strain sensing was conducted using a Yokogawa DL1620 digital oscilloscope connected to the electrospun PVDF strains sensor which is cyclically stretched using an Instron 5848 under an extension of 1mm per 5 seconds, using a 50 N load cell.

5.3 Results and discussions

5.3.1 Effects of the $SCCO_2$ treatment on morphology of the electrospun membranes

SEM micrographs of the untreated and $SCCO_2$-treated electrospun P(VDF-HFP) membranes are shown in Figure 5.1. In comparison with the untreated membane (Figure 5.1a), the treated membranes are more compact due to the high pressure applied (Figure 5.1b). The compactness of the membranes increases with the treatment temperature, while the fibrous nature of the membranes can be well retained up to the treatment temperature of 120°C.

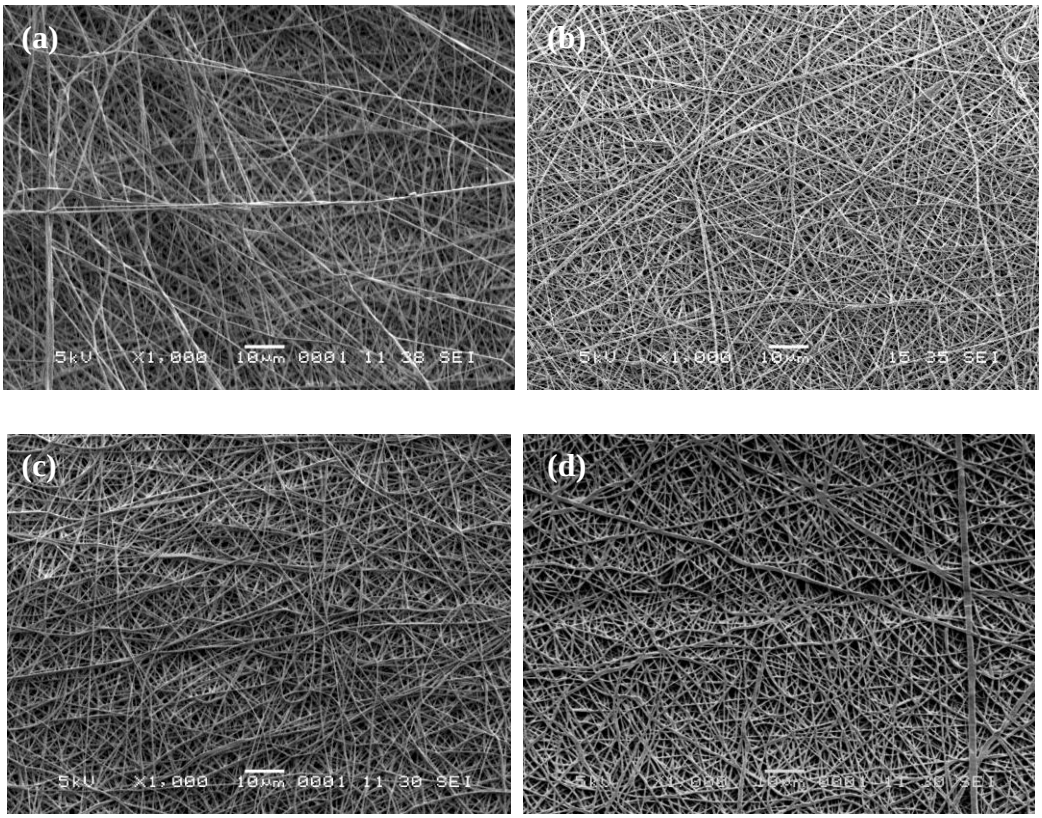

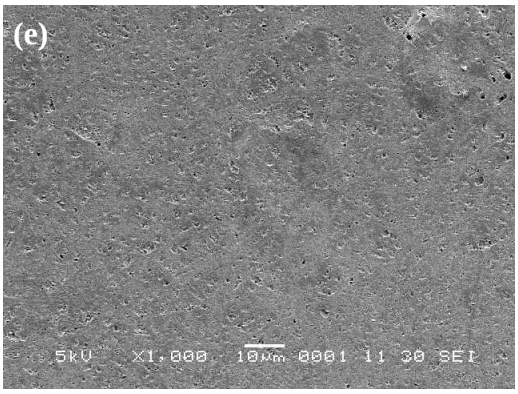

Figure 5.1 SEM micrographs of SCCO2-treated (a-e) electrospun P(VDF-HFP) nanofibrous membranes. The membranes were treated in SCCO2 at (a) 40°C, (b) 80°C (c) 100°C, (d) 120°C and (e) 140°C, respectively, under 4000 PSI pressure. All samples were electrospun from 60/40 DMF/acetone PVDF solutions at 18 kV. (Treatment at 60°C showed similar results to treatment at 40°C and thus not shown in this figure.)

SEM as well as FESEM micrographs of the untreated and $SCCO_2$-treated electrospun P(VDF-HFP) membranes at 100°C are shown Figure 5.2. In comparison with the untreated membane (Figure 5.2a), the treated membranes are more compact due to the high pressure applied (Figure 5.1b and 5.2d). After the treatment at 100°C, some nanofibers are significantly joined together forming junctions as a result of surface melting (Figure 5.2b), which greatly improves the dimensional stability of the nanofibrous membranes, as will be shown later.

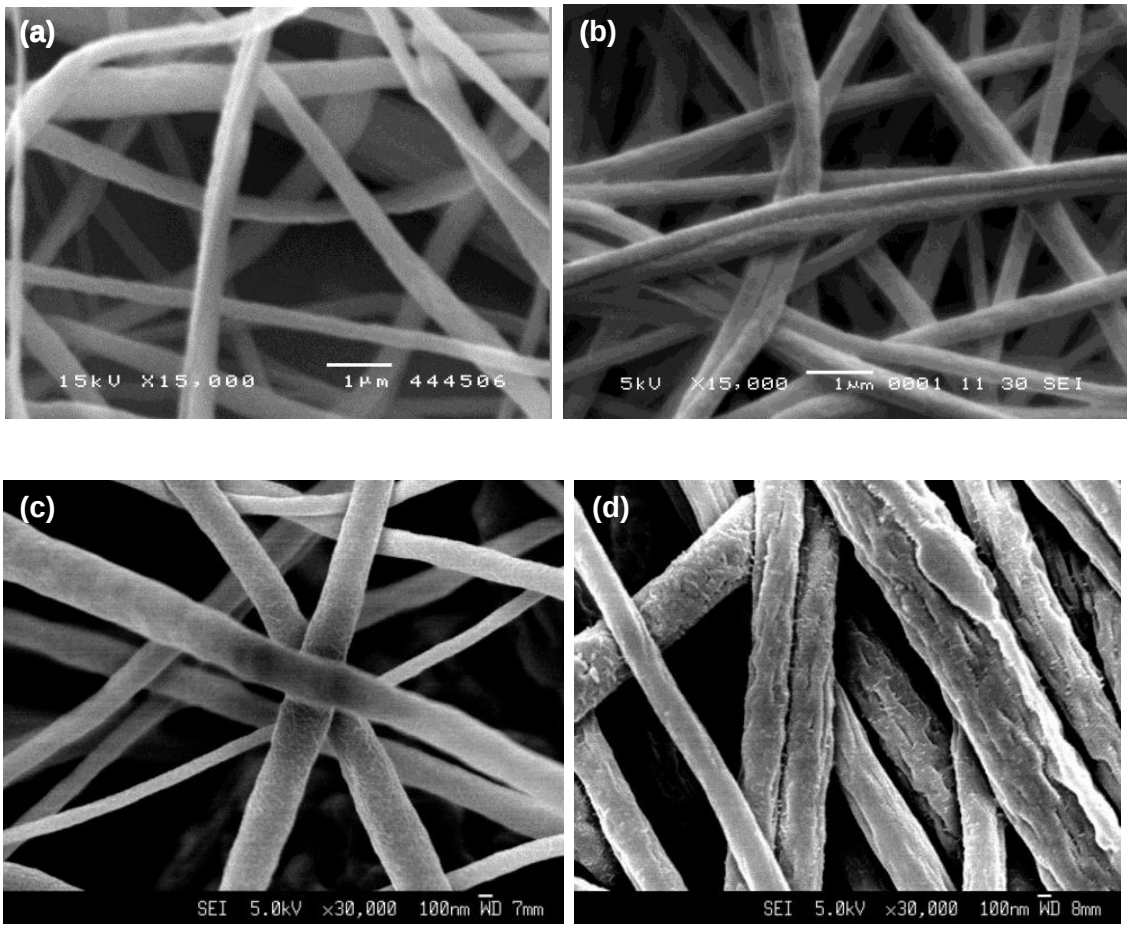

Figure 5.2 SEM (a and b) and FESEM (c and d) micrographs of the untreated (a and c) and SCCO2-treated (b and d) electrospun P(VDF-HFP) membranes. The treatment was conducted at 100°C and 4000 psi.

Based on the previous studies on the $SCCO_2$ treatment of bulk PVDF films,[105] foaming is able to occur under the treatment conditions used in this study. By adopting the reverse-barrier technique, CO_2 gas could, however, only diffuse in and out through the narrow gap between the two tightly clamped glass slides, as shown in figure 5.3. This effectively protects the electrospun membranes from the destructive forces of foaming while still induces porous morphology to

some extent, as evidenced by the unique rough and cracked surface of the treated nanofibers (Figure 5.2d) that are caused by the vigorous escape of the CO_2 absorbed in the amorphous regions of the nanofibers during the depressurizing process [50].

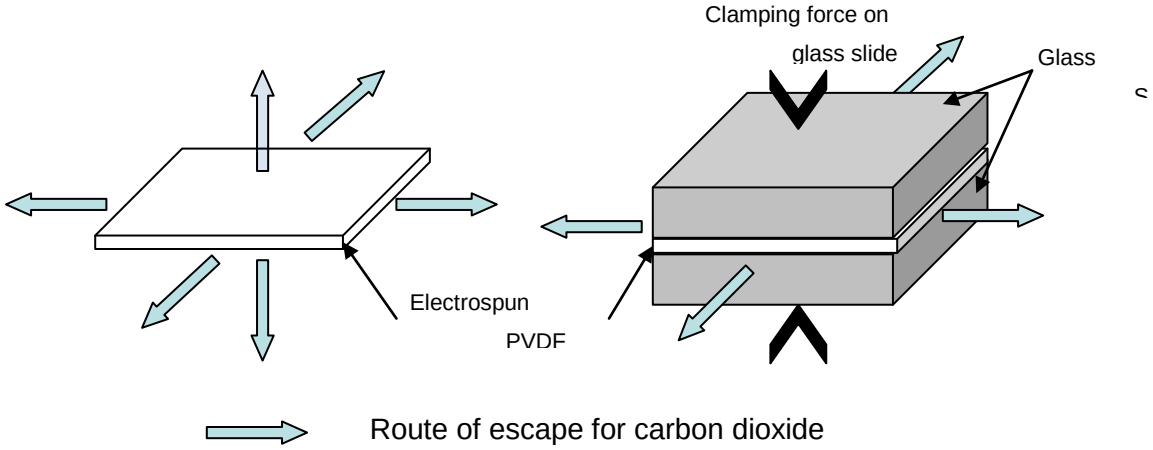

Figure 5.3 Route of escape for carbon dioxide (a) without and (b) with the reverse-barrier technique.

5.3.2 Effects of the $SCCO_2$ treatment on mechanical properties

When the electrospun P(VDF-HFP) membranes are subjected to $SCCO_2$ treatment at 100°C and 120° C, the fibrous morphology can still be maintained but melting can be observed at the fiber surface. This surface melting on the PVDF nanofibers will result in the formation of junctions (Figure 5.1d) at the intersecting regions of the nanofibers, under the applied temperature and pressure. The resulting morphology can improve the mechanical properties significantly, as demonstrated in Figure 5.4.

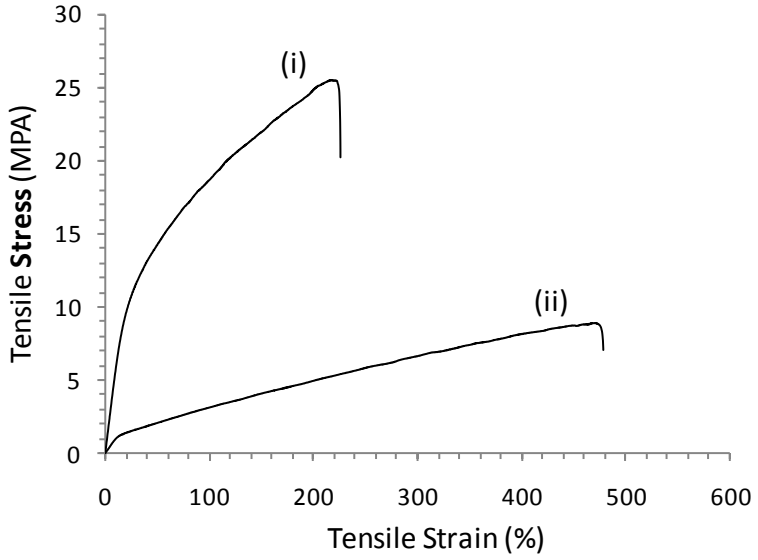

Figure 5.4 Mechanical Testing of (i) treated electrospun and (ii) untreated P(VDF-HFP) membranes by SCCO2 at 100°C under 4000 PSI pressure.

The resulting morphology is also beneficial for maintaining the structural integrity of the membrane. To demonstrate the structural integrity introduced by the $SCCO_2$ treatment, 1-butyl-3-methylimidazolium hexaflurophosphate ([BMIM]PF_6), an ionic liquid (IL), was dripped onto the substrate. Rapid diffusion of [BMIM]PF_6 could be observed due to the strong capillary forces exerted by the micro/nano channels in the membrane. As [BMIM]PF_6 can swell PVDF [116], the color changed from white to transparent. When the electrospun membranes are swollen by the IL, The untreated membrane could not retain its shape and eventually form a gelled mess. The membrane treated at 80°C could retain its shape but fiber pull-out was observed during manipulating the IL-loaded membrane. In contrast, the membrane treated at 100°C exhibits excellent dimensional stability after swelling in the IL for 7 days (Figure 5.5). Such $SCCO_2$ treated membranes is proven to be useful as a host for the IL in electrochemical devices, which will be discussed in the later sections.

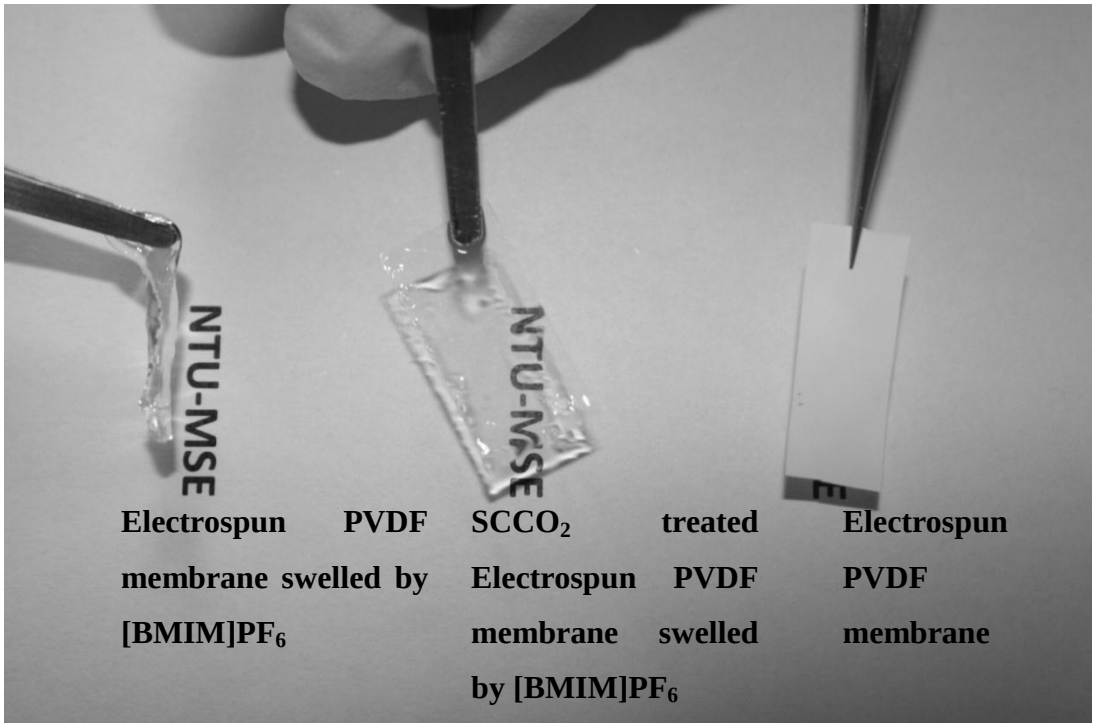

Figure 5.5 A picture showing the untreated and SCCO2-treated electrospun membranes after loading with the IL, with and without [BMIM]PF6.

5.3.3 Effects of $SCCO_2$ treatment on crystalline structures of electrospun PVDF

It is well known that PVDF can exhibit five different polymorphs, among which the α phase is the most thermodynamically stable phase while the β phase has the highest polarity. Different from the previous reports on the $SCCO_2$ treatment of PVDF bulk films,[111] we found that the $SCCO_2$ treatment of the electrospun membranes induces a drastic change in crystalline structures of the polymer, as indicated by the WAXD patterns shown in Figure 5.6A.

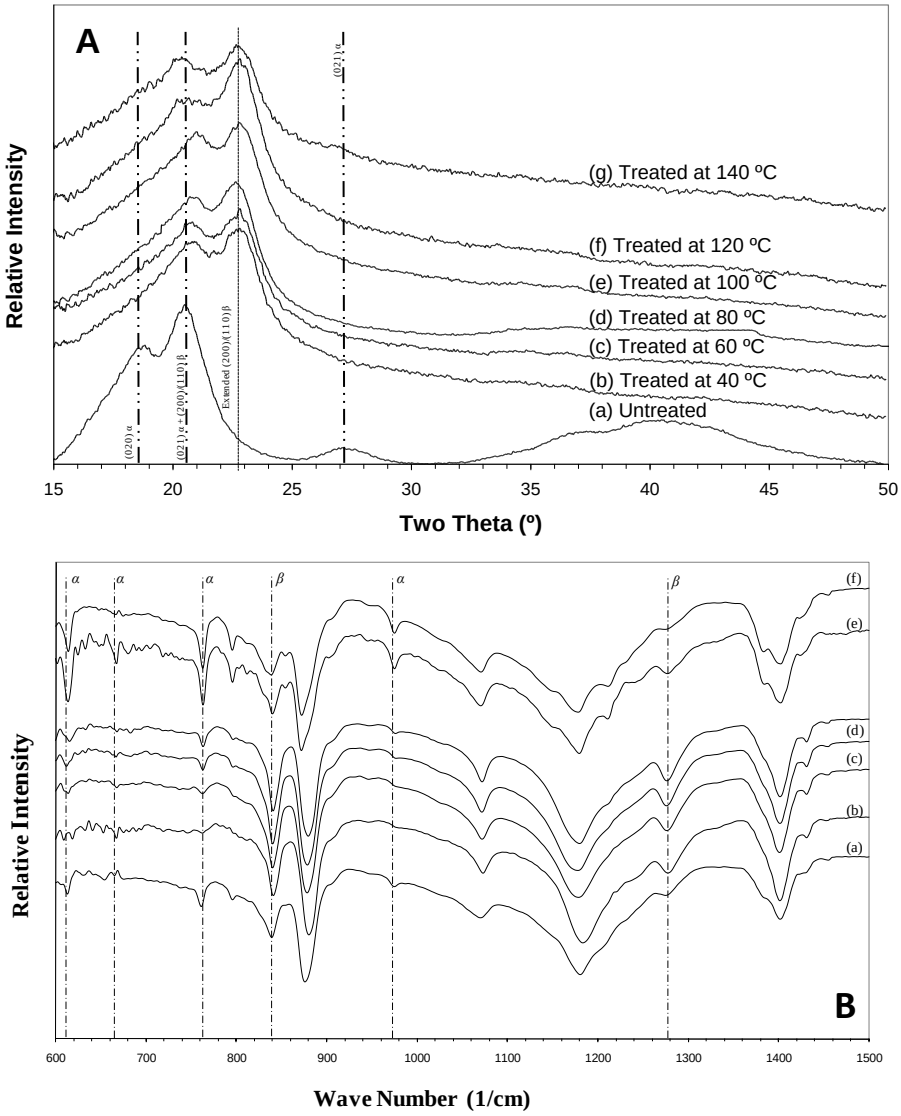

Figure 5.6 (A) WAXD patterns and (B) FTIR spectra of the as-spun P(VDF-HFP) membrane (a) and the membranes that have undergone SCCO2 treatment at 4000 psi and different temperatures (b-g).

For the untreated membrane (curve a), the presence of a strong peak at 2θ = 20.6º, which corresponds to (200)/(110) reflections of the β phase, and distinctive peaks at around 18.5º and

27.4º *2θ*, which correspond to (020) and (111) reflections of the *α* phase, respectively, indicates the co-existence of the *α* and *β* phases in the membrane [10].With the $SCCO_2$ treatment, a strong peak at 22.7º *2θ* appears, which can be assigned to *β*-phase extended-chain crystals (*β*-ECC) that has smaller interchain distance [104]. The formation of the *β*-ECC could not be detected by FTIR because FTIR measures local conformational changes [97], while the conformational difference between the normal *α* phase and the *β*-ECC may be too small. Nevertheless, FTIR spectra of the samples show the enhancement of the *β* phase up to the treatment temperature of 100ºC.

Previous reports have shown that the *β*-ECC can be induced by thermal treatments under very high pressure (a few hundred MPa) [50] or by high extensional force [4,104]. To understand the roles played by the electrospining and $SCCO_2$ treatment in the formation of the *β*-ECC, spin-coated P(VDF-HFP) films were subjected to the same treatment as their electrospun counterparts. Surprisingly, similar to that of the untreated sample (curve a in Figure 5.7), the diffraction peak corresponding to the *β*-ECC could not be observed in the $SCCO_2$-treated spin-coated film (curve b in Figure 5.6). To pinpoint the cause, spin-coated P(VDF-HFP) containing 0.1 wt.% h-SWCNT, which has been shown to promote the *β*-phase in PVDF [103], was also treated with $SCCO_2$. The WAXD pattern of the spin-coated P(VDF-HFP)/h-SWCNT shows only one major diffraction peak at $2\theta = 20.6°$ (curve c in Figure 5.7), which corresponds to normal *β* phase, while after the $SCCO_2$ treatment, the peak at $2\theta = 22.7°$ appears (curve d in Figure 5.7), signifying that the $SCCO_2$-treatment has induced the *β*-ECC. A major difference between the spin-coated P(VDF-HFP) and P(VDF-HFP)/h-SWCNT is that the *β* phase is dominant in the latter, which may act as nuclei for the *β*-ECC during the $SCCO_2$ treatment. Obviously, such nuclei also exist in the electrospun membranes [104]. Furthermore, an electrospun P(VDF-HFP) membrane was also subjected to high-pressure thermal treatment in nitrogen environment and no

β-ECC could be observed after the treatment, which implies that in addition to the *β*-phase nuclei and the pressure applied, the absorption of CO_2 into the amorphous region of the electrospun nanofibers also plays a pivotal role in the formation of the *β*-ECC. When CO_2 is absorbed into the electrospun P(VDF-HFP) nanofibers, it will allow the molecular chains to slide past one another more easily, and thus acting as a plasticizer to facilitate the growth of the *β*-ECC.

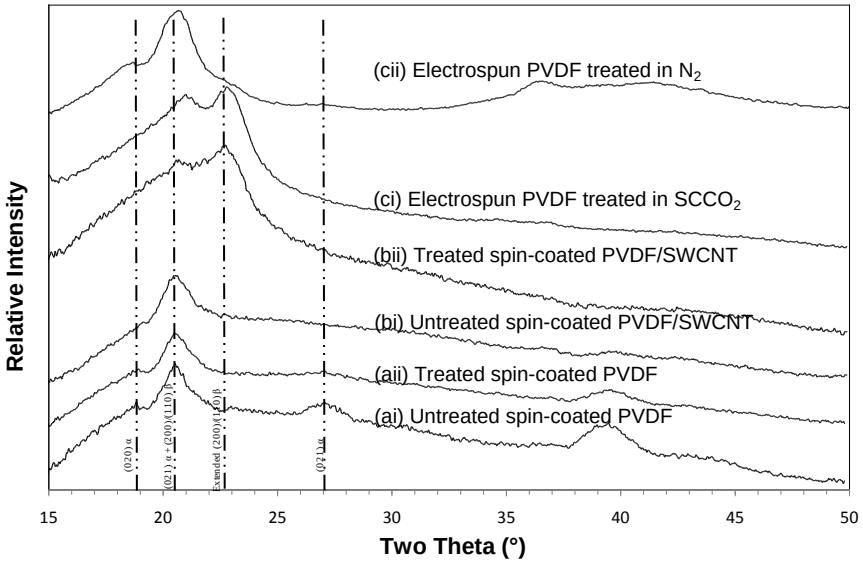

Figure 5.7 WAXD patterns of the untreated (ai) and SCCO2-treated (aii) spin-coated P(VDF-HFP) films, the untreated (bi) and SCCO2-treated (bii) spin-coated P(VDF-HFP)/h-SWCNT films, and the SCCO2-treated (ci) and high-pressure N2-treated (cii) electrospun P(VDF-HFP) membranes. For (aii) and (bii), the SCCO2 treatment was conducted at 100ºC and 4000 psi. For (ci) and (cii), the treatment was at 100ºC and 3000 psi.

The $SCCO_2$ treatment also influences crystallinity of the membranes. After the treatment at 40°C, the heat of fusion of the membrane is significantly reduced as compared with that of the

untreated one (Table 5.1), indicating that the swelling by CO_2 and the foaming effect could destroy some crystallites.

Table 5.1. Heat of fusion and peak melting temperatures of the untreated and $SSCO_2$-treated electrospun membranes obtained from the 1st heating DSC curves.

Treatment temperature (ºC)	Heat of fusion (J/g)	Melting Temperature (ºC)
Untreated	42.5	157.2
40	35.9	157.9
60	38.2	157.5
80	40.6	157.3
100	41.8	157.6
120	42.9	159.4
140	38.2	160.4

As the treatment temperature increases, the heat of fusion increases consistently until 120°C probably due to the increased extent of recrystallization. At the treatment temperature of 140°C, the nanofibers are completely melted (Figure 5.1e) and the re-solidification leads to a much lower heat of fusion. To achieve maximum β-ECCs enhancement, good morphology while balancing the need to have substantial crystallinity, the treatment temperature of 100°C at 4000 PSI was selected for the rest of the work in this chapter.

In chapter 4, it has been shown that by adding CNTs (both hydrolyzed and esterified) into PVDF prior to electrospinning and collected using the modified disk collector, β-ECCs can also been enhanced. Thus, it is worthwhile to explore how the $SCCO_2$ treatment can influence the polymorphism of such electrospun P(VDF-HFP)/CNTs composite nanofibers and study its effect on β-ECCs formation.

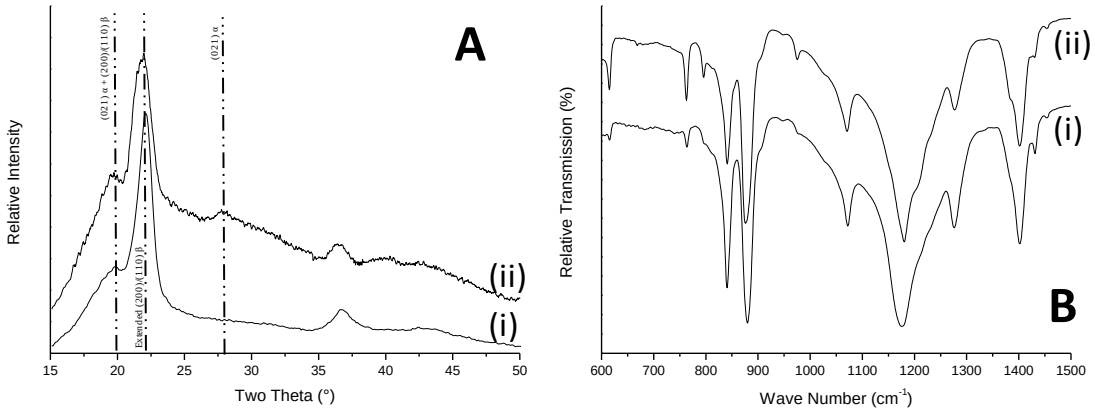

Figure 5.8 (A) WAXD patterns and (B) FTIR spectra of aligned electrospun fibrous films of (i) P(VDF-HFP)/h-SWCNT and (ii) P(VDF-HFP)/e-SWCNT after treated by SCCO2. The CNT concentration is 0.01 wt.% for (ii) and (iii).

The effects of $SCCO_2$ treatment on the electrospun P(VDF-HFP) with h-SWCNTs as well as e-SWCNTs' membranes can be clearly observed from the WAXD patterns in Figure 5.8. The $SCCO_2$ treatment has a significant influence in the formation of the highly extended β-phase for both electrospun P(VDF-HFP)/e-SWCNT and P(VDF-HFP)/h-SWCNT membranes. From the WAXD, the high angle peak at around 22° 2θ has become the most prominent peak, indicating

the extensive formation of the highly extended *β*-phase in both the electrospun P(VDF-HFP)/e-SWCNT and P(VDF-HFP)/h-SWCNT membranes. This indicates that the $SCCO_2$ treatment plays a significant role in enhancing this highly extended *β*-phase, which coincides with our previous results. However, it can be observed that the treatment did not fully suppress the *α*-phase in electrospun P(VDF-HFP)/e-SWCNT membranes as indicated by a peak at 27.4° *2θ*. This result is collaborated by the FTIR spectrum where peaks are the α-related peaks at 614, 765 and 975 cm^{-1} are observed. It can also be clearly observed that the overall *β*-phase content is much higher for the treated electrospun P(VDF-HFP)/h-SWCNT membrane as compared to its P(VDF-HFP)/e-SWCNT counterpart, as observed in the increase in intensity of the β-related peak at 840 and 1278 cm^{-1}. As compared to the as-spun P(VDF-HFP)/e-SWCNT nanofibrous membranes in chapter 4 (Figure 4.13), the treatment brought about the growth of the *β*- as well as the extended *β*-phase. However, due to the use of heat during the treatment, the growth of the *α*-phase was also encouraged as well (figure 5.8(Bii)). This phenomenon was not observed for electrospun P(VDF-HFP)/h-SWCNT membranes. The reason could be due to the stronger interaction between P(VDF-HFP) molecular chains and the hydrolyzed CNTs as compared to its esterified counterpart, as explained in chapter 4.

5.3.4 Functionality of $SCCO_2$ treated electropun PVDF membranes

5.3.4.1 Functionality as an ionic liquid (IL) host

ILs have been increasingly explored as the electrolyte in various electrochemical devices due to their excellent thermal, chemical and electrochemical stabilities, high ionic conductivity and good interfacial interactions with solid materials [114]. Although IL/PVDF gel electrolytes exhibit

good stabilities, the ion transportation in the gels is slower than that in neat ILs due to the highly viscous nature of the gels. By hosting ILs in porous polymer matrices, higher ionic conductivities could be achieved [115,116]. This provides the motivation of using our $SCCO_2$ electrospun P(VDF-HFP) membranes as an IL host. As shown in Figure 5.5, when infiltrated with the IL, [BMIM]PF_6, the untreated membrane could not retain its shape and eventually form a gelled mess, which is in clear contrast to the $SCCO_2$-treated membrane that exhibits excellent dimensional stability, even after swelling in the IL for 7 days. The good structural integrity of the IL-loaded membrane allows easily maintaining uniform thickness of the electrolyte across a large area, which greatly benefits practical device fabrication. More importantly, although the amounts of the IL retained in the treated membranes are smaller than that in the untreated one (Figure 5.9), the ionic conductivity of the treated membranes is very close to that of the neat IL[116] and is nearly one order higher than that of the corresponding IL/P(VDF-HFP) gel (Table 5.2). The high ionic conductivity is mainly contributed by the IL embedded in the micron-sized interpenetrating pores of the treated membranes. We are the first group to utilize such electrospun P(VDF-HFP) nanofibrous membranes and post-treated it to allow the membrane to retain its shape even after IL loading, which is not possible for untreated membranes. These results shows that $SCCO_2$ treated electrospun P(VDF-HFP) membranes are suitable candidates to used as a host for ILs and deployed in the use of electrochemistry.

Table 5.2. Ionic conductivities of the neat IL, IL/P(VDF-HFP) gel and IL-loaded electrospun membrane

	Neat IL	IL/PVDF gel	IL-loaded electrospun membrane*
Ionic conductivity (S/cm)	1.90×10^{-3} [22]	3.12×10^{-4}	1.75×10^{-3}

* *The membrane was $SCCO_2$-treated at 100ºC and 4000 psi.*

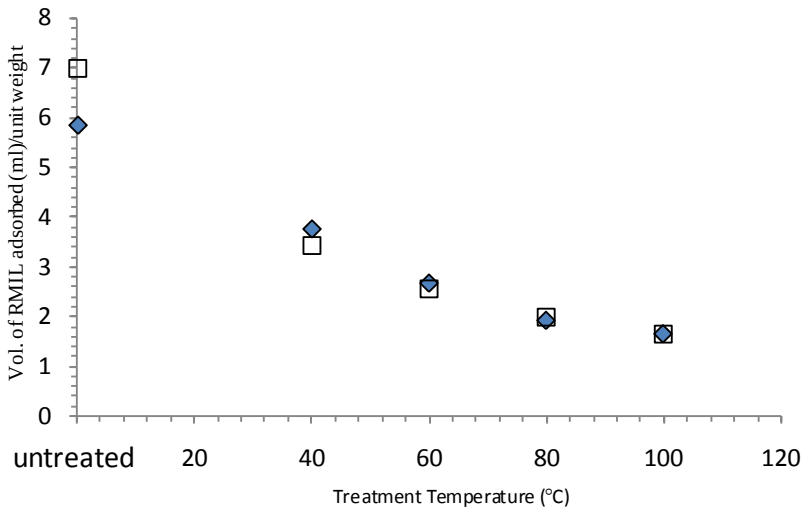

Figure 5.9 Plot of volume of IL adsorbed per unit weight versus the different SCCO2 treatment temperatures of the electrospun P(VDF-HFP) membranes where □ – denotes soaking time of 1 day and ♦ - denotes soaking time of 1 week.

5.3.4.2 Functionality as a strain sensor

The electrospinning process involves the use of very high voltages to induce the formation of nanofibers. Such high voltages have been found to provide a poling effect on the P(VDF-HFP) nanofibers. This in turn will allow the alignment of the dipoles within to the source of the electric field [77,78], enabling it to be utilized as actuators or nanogenerators. From chapter 3, it is known that the addition of h-SWCNTs into P(VDF-HFP) can enhance the β-phase in P(VDF-HFP) and it has been demonstrated in section 5.3.3 that $SCCO_2$ treatment of spin-coated films with h-SWCNTs can promote the highest growth of the β-ECC. Thus, it is worthwhile to explore the use of $SCCO_2$ to treat aligned electrospun P(VDF-HFP)/h-SWCNTs for the fabrication of a simple capacitive strain sensing device. Due to the preferential alignment of the nanofibers, the *in*-situ poling effect during electrospinning as well as effective stress transfer throughout the aligned nanofibrous membrane when mechanically stimulted, aligned electrospun P(VDF-HFP)/h-SWCNT membranes should perform more efficiently as compared to the random non-woven mat and was selected for use to test the functionality. The device configuration and assembly method are illustrated in Figure 5.10. A simple capacitive design was adopted as the electrodes on both sides of the piezoelectric layer can harness the electrical response effectively when mechanically stimulated and the simple design allows the different layers to bond effectively due to the surface melting of the electrospun P(VDF-HFP) fibers as well as the spin-coated films during the $SCCO_2$ treatment. A reference device was also fabricated, in which the aligned electrospun P(VDF-HFP)/h-SWCNTs was replaced by the aligned electrospun pristine P(VDF-HFP) membranes. It is important to take note that the spincoated P(VDF-HFP) layers, which has been pre-annealed to convert all other polar phases to the α phase has no contribution to the electrical response of the device. Additionally, this methodology allows the spin-coated films to protect the sandwiched

layer of aligned electrospun P(VDF-HFP) membrane which is weaker in nature. Through the $SCCO_2$ treatment, surface melting of the electrospun fibers was initiated to allow all the layers to physically bond together and ensure a good contact of the active layer to the electrodes. Additionally, as the construction of the device is exactly the same, all contributions from other sources (including the contribution of the amorphous phase in the spin-coated PVDF) can be excluded and the different performance of the devices should be attributed to the properties of the piezoelectric electrospun layer. The primary purpose for the spincoated P(VDF-HFP) is to provide a platform to deposit the electrodes as well as to form a protective barrier to house the aligned electrospun fibrous mat.

It can be clearly observed that under an extension of 1 mm, the P(VDF-HFP)/h-SWCNT device can register approximately 200 mV in response as compared with approximately 20 mV for the P(VDF-HFP) device (Figure 5.11A). To the best of our knowledge, this is the first example of an electrospun PVDF mat-based piezoelectric device. It demonstrated that with only 0.01 wt% h-SWCNTs, the pieozoelectric effect of P(VDF-HFP) is enhanced significantly. The underlying mechanisms for such a drastic enhancement have yet to be clarified. The high content of □-form ECCs in the aligned electrospun PVDF/h-SWCNT mat would certainly contribute to the high response. However, it is expected that the presence of electrically conductive nanotubes, the confinement of the PVDF electrets on the nanotube surface, the effective load transfer from the PVDF molecular chains to nanotubes and the contribution from the amorphous phase may also influence the piezoelectric effect, which will be a subject for future studies.

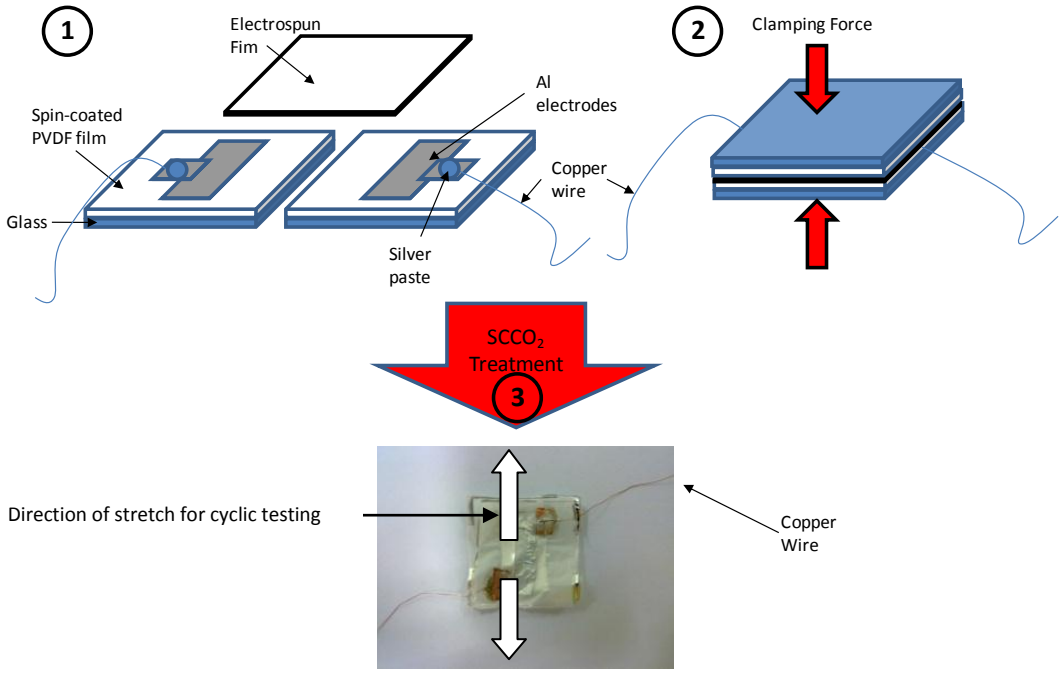

Figure 5.10 Methodology to produce the strain sensor by sandwiching all components together and subject to SCCO2 treatment at 100°C at 4000 PSI.

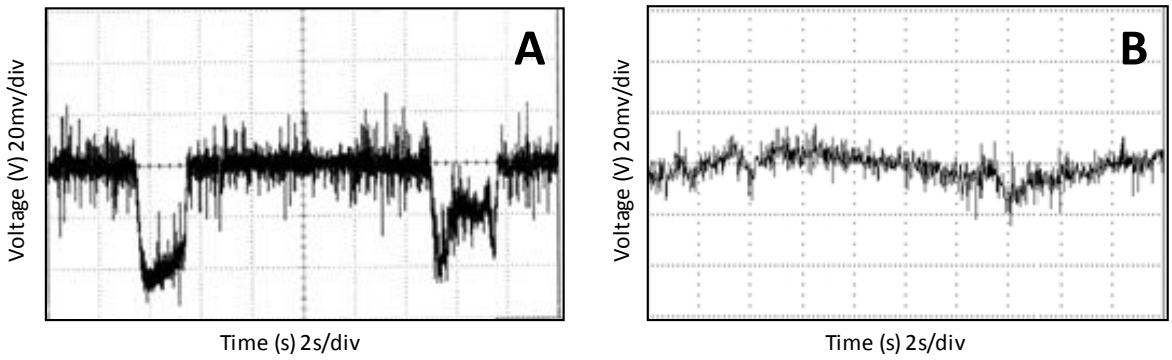

Figure 5.11 Voltage response under a tensile strain of the electrospun (A) P(VDF-HFP)/h-SWCNT and (B) P(VDF-HFP) strain sensor under a 1mm extension.

5.4 Conclusions

The $SCCO_2$ treatment of electrospun PVDF nanofibrous membranes has been successfully accomplished with the aid of reverse-barrier technique. The surface melting of the nanofibers during the treatment induces inter-fiber junctions that greatly enhance the mechanical properties of the as-spun membranes and the dimensional stability of the IL-loaded membranes. The treatment also leads to porous morphology and reduced crystallinity of the nanofibers due to the foaming effect, and the formation of the β-ECC due to the presence of β-phase nuclei, the pressure applied and the plasticizing effect of $SCCO_2$. The IL-loaded PVDF membranes exhibit an ionic conductivity value close to that of the neat IL; they thus have great potential to be used in various electrochemical devices. The fabricated electrospun PVDF/CNTs simple strain sensor by $SCCO_2$ also showed a significant increase in response under an applied strain as compared to its electrospun PVDF counterpart. Furthermore, we believe that $SCCO_2$ treatment may be applied to modify structures and morphologies of other electrospun polymer membranes and thus has significant impact on the applications of polymer nanofibrous membranes in various fields.

6 Conclusions

Based on the analysis of the experimental results, it can be concluded that:

(1) Using the modified rotating disk collector, the direct deposition of well aligned electrospun P(VDF-HFP) nanofibers with relatively good compactness and uniformity across a relatively large flat substrate is achieved. The modification alters the electric-field-distribution on the disk, which fosters the fanning of the nanofibers, while the electric field between the separate electrodes and the mechanical force exerted by the rotational disk facilitate the alignment.

(2) The specific environment and force fields created on the modified rotating disk cause the electrospun fibers being effectively stretched to form highly oriented *β*-form crystallites with slightly reduced inter-chain distance. It also leads to slight increases in crystallinity and crystal size. A mechanism for the structural alteration is proposed: it may be related to the formation of extended-chain β-phase crystals with a more perfect planar-zigzag conformation under a high tensile stress. The P-E hysteresis loops obtained from aligned P(VDF-HFP) fibrous thin films provides some evidence for the switching of the dipoles in the electrospun P(VDF-HFP) nanofibers.

(3) The interfacial interaction between the surface hydroxylated SWCNTS and P(VDF-HFP) and the extensional force experienced by the nanofibers collected by the modified rotating disk collector can work synergistically to induce highly oriented *β*-form crystallites extensively at a very low SWCNT concentration. In contrast, the effect of the

MWCNTs on crystal orientation is insignificant at this very low CNT concentration as a result of the detrimental effect of the MWCNTs on the preferred orientation of P(VDF-HFP) chains.

(4) Hydrogen bonding between the functional groups on the CNTs and P(VDF-HFP) chains play a critical role in providing effective interfacial stress transfer, allowing the extensive formation of the extended-chain β-form crystallites. In contrast, the addition of e-SWCNTs, which has a reduced hydrogen bonding capability as most hydroxyl groups are caped, does not promote the formation of the extended-chain β-form crystallites significantly, although still providing similar crystal orientation.

(5) The surface melting of the nanofibers during the $SCCO_2$ treatment induces inter-fiber junctions that greatly enhance the mechanical properties of the as-spun membranes and the dimensional stability of the IL-loaded membranes. The treatment also leads to porous morphology and reduced crystallinity of the nanofibers slightly due to the foaming effect, while it promotes the formation of the β-ECC due to the presence of β-phase nuclei, the pressure applied and the plasticizing effect of $SCCO_2$.

(6) Overall, the results suggest that the additional stretching force provided by the modified rotation disk collector, the incorporation of surface-hydroxylated SWCNTs and post $SCCO_2$ treatment can work synergistically to promote the formation of well oriented extended-chain β-phase crystallites in P(VDF-HFP).

(7) The alignment and $SCCO_2$ treatment can also make the nanofibrous mats more compact, enabling the demonstration of functionalities of the electrospun nanofibers. The IL-loaded P(VDF-HFP) membranes exhibit an ionic conductivity value close to that of the neat IL; they thus have great potential to be used in various electrochemical devices. The

electrospun P(VDF-HFP)/h-SWCNT mat-based piezoelectric device shows a significant increase in piezoelectric response as compared with its electrospun P(VDF-HFP) counterpart. However, the underlying mechanisms for the observed piezoelectric effect need to be further studied.

7 Recommendations for Future Work

Based on the results and discussions, the following recommendations are suggested for future investigations.

7.1 Further Investigation on the piezoelectric properties of the $SCCO_2$ treated electrospun membranes

From Chapter 5, it is proven that the $SCCO_2$ treatment can enhance the β-ECCs as well as making the membrane more compact while simultaneously increase its mechanical strength. Using the same technique, a piezoelectric device can be fabricated *in-situ* and was proven to be piezoelectric via its converse-piezoelectricity. Although our test proves that such a technique is suitable for making piezoelectric devices, more can be done to probe the change in structure in relation to its piezoelectric properties. Recently, a unique method to test the piezoelectric response as well as characterizing its piezoelectric constants of a single electrospun PVDF fiber (Figure 7.1) was reported [116,117]. The testing technique can provide a platform for us to compare the difference in piezoelectric response due to the change in the polymorphism as well as the role of CNTs in enhancing the piezoelectric properties of PVDF. Additionally, the piezoelectric constants of our $SCCO_2$ treated fibers can also be determined.

7.2 Fabrication of single layer array of electrospun PVDF fiber for sensing/actuator applications.

Near-field electrospinning (NFS) [118], a relatively new reincarnation of the traditional electrospinning process allows the user to deposit fibers in an easy, continuous and controlled manner. NFS also allows the user to deposit patterned arrays on a substrate easily [116]. Using our developed $SCCO_2$ post-treatment, we can easily bond such arrays on to pre-patterned electrodes deposited on a thin spin-coated film, as well as bond the intersections of the electrospun fibers. A combination of both techniques will allow the fabrication of a single pattern array of electrospun PVDF and with the correct patterned electrodes, a sensitive yet powerful force sensor across a large array that is sensitive to a very small force due to their small dimensions can be produced. Sensitivity can be further tuned by the addition of CNTs into the system prior to electrospinning. Such patterned devices can also be utilized for actuator applications in the form of smart woven fabrics, allowing the harvesting of electricity from the device due to the day-to-day activities of man.

7.3 Investigations on the addition of graphene and its impact of polymorphism and piezoelectric properties in electrospun PVDF.

CNTs has been shown to enhance the polymorphism of PVDF in chapter 4 and also enhance the piezoelectric response of electrospun PVDF in chapter 5. Graphene, which is a form of "unrolled" CNTs, may also strongly influence the polymorphism of PVDF. Similar to CNTs, grapheme sheets can be easily functionalized with surface groups. However, the change in the physical shape, as well as the PVDF molecular chain interaction with graphene has not been studied. It will be worthwhile to understand the impact of using grapheme as an additive and

study its impact on the polymorphism and electroactive properties of PVDF. Additionally, if electrospinning can align the graphene sheets with the nanofibers, such a morphology may prove useful in piezoelectric applications. .

7.4 Investigations on the crystal phase evolution of electrospun P(VDF-HFP) collected using the modified rotating disk.

To understand more of crystal phase evolution of electrospun P(VDF-HFP) collected using the modified rotating disk collector, further investigations can be carried out using Synchrotron X-ray (high intensity, simultaneous SAXS and WAXS).

References

1. Tahiro K. (1995). Crystal Structure and Phase Transistion of PVDF and Related Copolymers. In *Ferroelectric Polymers: Chemistry, Physics and Applications,* Nalwa, H. S. (Eds.), Marcel Dekker Inc: New York.
2. Wang Z. Y., Fan H. Q., Su K. H., Wen Z. Y. (2006). Structure and piezoelectric properties of poly(vinylidene fluoride) studied by density functional theory. *Polym.*, 47, 7988-7996.
3. Samon J. M., Schultz J. M., Hsiao B. S. (2002). Structure development in the early stages of crystallization during melt spinning. *Polym.*, 43, 1873-1875.
4. Xu J. N., Johnson M., Wilkes G. L. (2004). A tubular film extrusion of poly(vinylidene fluoride): structure/process/property behavior as a function of molecular weight. *Polym.*, 45, 5327-5340.
5. Branciforti M. C., Sencadas V., Lanceros-Mendez S., Gregorio R. (2007). New technique of processing highly oriented poly(vinylidene fluoride) films exclusively in the β-phase. *J. Polym. Sci. : Part B : Polym. Phys.*, 45, 2793-2801.
6. Bune A. V., Fridkin V. M., Ducharme S., Blinov L. M., Palto S. P., Sorokin A. V., Yudin S. G., Zlatkin A. (1998). Two-dimensional ferroelectric films. *Nature*, 391, 874-877.
7. Zhang H., Ren P., Zhang G. F., Xiao C. F. (2006). Effects of Electrostatic Field Intensity on Crystal Structure and Morphology of PVDF fibers and Films. *High Perform. Polym.*, 18, 305-312.
8. Nguyen A. C., Lee P. S., Yee W. A., Lu X., Srinivasan M., Mhaisalkar S. G. (2007). Enhanced functional and structural characteristics of poly(vinylidene-trifluoroethylene) copolymer thin films by corona poling. *J. Electrochem. Soc.*, 154, G224-G228.

9. Nasir M., Matsumoto H., Minagawa M., Tanioka A., Danno T., Horibe H. (2007). Preparation of Porous PVDF nanofiber from PVDF/PVP Blend by Electrospray Depostion. *Polym. J*., 39, 1060-1064.
10. Yee W. A., Kotaki M., Liu Y., Lu X. (2007). Morphology, polymorphism behavior and molecular orientation of electrospun poly(vinylidene fluoride) fibers. *Polym.*, 48, 512-521.
11. Zheng J., He A. (2007). Polymorphism Control of Poly(vinylidene fluoride) through Electrospinning. *Macromol. Rapid. Commun.*, 28, 2159-2162.
12. Teo W. E., Ramakrishna S. (2006). A review on electrospinning design and nanofibre assemblies. *Nanotechnology*, 17, R89.
13. Inai R., Kokaki M., Ramakrishna S. (2005). Structures and properties of electrospun PLLA single nanofibres. *Nantechnology*, 16, 208.
14. Matthews J. A., Wnek G. E., Simpson D. G., Bowlin G. L. (2002). Electrospinning of Collagen Nanofibers. *Biomacromolecules*, 3, 232-238.
15. Li D., Wang Y., Xia Y. (2003). Electrospinning of polymeric and ceramic nanofibers as uniaxially aligned arrays. *Nano. Lett.*, 3, 1167-1171.
16. Pawlowski K. J., Belvin H. L., Raney D. L., Su J., Harrison J. S., Siochi E. J. (2003). Electrospinning of a micro-air vehicle wing skin. *Polym.*, 44, 1309-1314.
17. Ramaratham A., Jalili N. (2006). Reinforcement of Piezoelectric Polymers with Carbon Nanotubes: Pathways to Next-generation Sensors. *J. Intelligent Mat. Systems and Structures*, 17, 199-208.
18. Levi N., Czerw R., Xing S., Iyer P., Carrol D. L. (2004). Properties of Polyvinylidene Difluoride-Carbon Nanotube Blends, *Nano. Lett.*, 4, 1297-1272.
19. Halwa, H. S. (2002). Handbook of Thin Filmed Materials Volume 3: Ferroelectric and Dielectric Thin Films. Academic Press: San Diego.
20. Wang, T. T., Herbert, J. M., Glass, A. M. (1988). The Applications of Ferroelectric Polymers. Blackie & Son Ltd: USA.
21. Guy, I. L., Unsworth, J. (1987). Conformational and Crystallographic changes occurring in Poly(vinylidene Fluoride) during the production of D-E field Hysteresis Loops. *J. Appl. Phys.*, 61, 5374-5378.

22. Newman, B. A., Scheinbeim, J. I., Wee, J. W., Takase, Y. (1992). A new class of Ferroelectric polymers, the odd-numbered nylons. *Ferroelectrics*, 127, 229-234.

23. Katz, D., Gelfandbein, V. (1982), Ferroelectric behavior of α-nylon 11. *J. Phys. D Appl. Phys*., 15, L115-L118.

24. Bharti, V., Nath, R. (2001).Piezo-, Pyro-, and Ferroelectric Properties of simultaneously stretched and corona poled extruded poly(vinyl chloride) films. *J. Phys. D Appl. Phys.*, 34, L667-L672.

25. Yun, G. Y., Kim, J. H., Kim, J. (2009). Dielectric and Polarization behavior of Cellulose Electro-active paper (EAPap). *J. Phys. D Appl. Phys.*, 42, 082003.

26. Helfrich, W. (1971). A simple method to observe the piezoelectricity of liquid crystals. *Phys. Lett. A*, 35, 393-394.

27. Guy, I. L., Unsworth, J. (1987). Conformational and Crystallographic changes occurring in Poly(vinylidene Fluoride) during the production of D-E field Hysteresis Loops. *J. Appl. Phys.*, 61, 5374-5378.

28. Egorov, E. A., Tshmel, A. E., Zhizhenkov, V. V. (1998). Structure of the tie chains in oriented polyethylene: dependence of all-trans stem lengths on draw ratio. *Polym.*, 39, 497-499.

29. Furukawa, T. (1997). Structural and Functional Properties of Ferroelectric Polymers. *Adv. Colloid Interfaces Sci.*, 71-72, 183-208.

30. Davis, G. T., Mckinney, J. E., Boardhurst, M. G., Roth, S. C. (1978). Piezoelectricity and pyroelectricity in Polyvinylidene fluoride. *J. Appl. Phys.*, 49, 4992-4997.

31. Takashi, Y., Tadokoro, H. (1980). Crystal Structure of Form III of Poly(vinylidene fluoride). *Macromolecules*, 13, 1317-1318.

32. Lovinger, A. J. (1980). Unit Cell of the γ-phase of Poly(vinylidene fluoride). *Macromolecules*, 14, 322-325.

33. Tamura, M., Ogasawa, K., Ono, N., Hagiwara, S. (1974). Piezoelectricity in uniaxially stretched Poly(vinylidene fluoride). *J. Appl. Phys.*, 45, 3768-3771.

34. Sathanon, U., Fukada, S., Sekiguchi, A., Ogina, K., Miyata, S. (2004). Piezoelectricity of vinylidene fluoride-trifluoroethylene copolymer films in various poling conditions. *J. Appl. Polym. Sci.*, 92, 856-860.

35. Matsushige, K., Nagata, K., Takemura, T. (1978). Direct Observation of Crystal Transformation Process of Poly(vinylidene fluoride) under High Pressure by PSPC X-ray System. *Jpn. J. Appl. Phys.*, 17, 467-472.

36. Salimi, A., Yousefi, A. A. (2004). Conformational Changes and Phase Transformation Mechanisms in PVDF Solution Casted films. *J. Polym. Sci. Part B: Polym. Phys*., 42, 3487-3495.

37. Park, Y. J., Kang, Y. S., Park, C. (2005). Micropatterning of semicrystalline poly(vinylidene fluoride) (PVDF) films. *Euro. Polym. J.*, 41, 1002-1012.

38. Tian, X., Jiang, X. (2008). Poly(vinylidene fluoride-co-hexafluropropene) (PVDF-HFP) membranes for ethyl acetate removal from water. *J. Hazard Mater.*, 153, 128-135.

39. Herman, Umemoto, S., Kikutani, T., Okui, N. (1998). Chain Length Effects on Crystal Formation in Vinylidene Fluoride Oligomers. *Polym. J.*, 30, 659-663.

40. Hsu, C. C., Geil, P. H. (1984). Morphology-Structure-Property Relationships in Ultraquenched Poly(vinylidene fluoride). *J. Appl. Phys*., 56, 2404-2411.

41. Schaffner, R., Jungnickel, B. J. (1994). The electric moment contribution to the piezoelectric coefficient of PVDF/PMMA blends. *IEEE Trans. Dielectr. Elect. Insul.*, 1, 553-562.

42. Gerliczy, G., Betz, R. (1987). Solef PVDF Biaxially Oriented Piezo- and Pyro-Electric Films for Transducers. *Sensors and Actuators*, 12, 207-223.

43. Benz, M., Euler, W. B., Gregory, O. (2002). The Role of Solution Phase Water on the Deposition of Thin Films of Poly(vinylidene fluoride). *Macromolecules*, 35, 2682-2688.

44. Priya, L., Jog, J. P. (2002). Poly(vinylidene fluoride)/Clay Nanocomposites Prepared by Melt Intercalation: Crystallization and Dynamic Mechanical Behaviour Studies. *J. Polym. Sci. Part B: Polym. Phys.*, 40, 1682-1689.

45. He X., Yao K. (2006). Crystallization mechanism and piezoelectric properties of solution-derived ferroelectric poly(vinylidene fluoride) thin films. *Appl. Phys. Lett.*, 89, 112909-112909-3.

46. Yu W., Zhao Z., Zheng W., Song Y., Li B., Long B., Jiang Q. (2008). Structural characteristics of poly(vinylidene fluoride)/clay nanocomposites. *Mater. Lett.*, 62, 747-750.

47. Peng Q. Y., Cong P. H., Liu X. J., Liu T. X.,Huang S., Li T. S. (2009). The preparation of PVDF/Clay nanocomposites and the investigation of their tribological properties. *Wear*, 266, 713-720.

48. Mago G., Kaylon D. M., Fisher F. T. (2008). Membranes of polyvinylidene fluoride and PVDF nanocomposites with carbon nanotubes via immersion precipitation. *J. Nanomaterials*, 1-7.

49. Laud A., Gustafsson C., Bertilsson H., Rychwalski R. W. (2011). Enhancement of β phase crystals with the use of nanofillers in PVDF films and fibers. *Composite Sci. Technol.*, 71, 222-229.

50. Hattori T., Hikosaka M., Ohigashi H. (1996). The crystallization behavior and phase diagram of extended-chain crystals of poly(vinylidene fluoride) under high pressure. *Polym.*, 37, 85-91.

51. Ohigashi H., Hattori T. (1995). Improvement of piezoelectric properties of poly(vinylidene fluoride) and its copolymers by crystallization at high pressures. *Ferroelectrics*, 171, 11-32.

52. Davis G. T., Mckinney J. E., Broadhurst M. G., Roth S. C. (1978). Electric-field-induced phase changes in poly(vinylidene fluoride). *J. Appl. Phys*., 49, 4998-5002.

53. Kaura T., Nath R., Periman M. M. (1991). Simultaneous stretching and corona poling of PVDF films. *J. Phys. D: Appl. Phys.*, 24, 1848-1852.

54. Kuma A., Periman M. M. (1993). Simultaneous stretching and corona poling of PVDF and P(VDF-TrFE) films. II. *J. Phys. D: Appl. Phys.*, 26, 469-473.

55. Xia Y., Yang P. (2003). Chemistry and Physics of Nanowires. *Adv. Mater*., 15, 351-456.

56. Papenburg B. J., Versteeg L. A. M. B., Grijpma D. W., Feijen J., Wessling M., Stamatialis D. (2010). A facile method to fabricate poly(L-lactide) nano-fibrous morphologies by phase inversion. *Acta Biomaterialia*, 6, 2477-2483.

57. Xia Y., Li D. (2004). Electrospinning of Nanofibres: Reinventing the Wheel? *Adv. Mater*., 16, 1151-1170.

58. Huang Z. M., Zhang Y. Z., Kotaki M., Ramakrishna S. (2003). A review on polymer nanocomposites by electrospinning and their applications in nanocomposites. *Composites Sci. and Technol.*, 63, 2223-2253.

59. Kessick R., Reneker D. H. (2004). The use of AC potentials in electrospraying and electrospinning processes. *Polym.*, 45, 2981-2984.

60. Doshi J., Reneker D. H. (1995). Electrospinning Process and Applications of Electrospun Fibers. *J. of Electrostatics*, 35, 151-160.

61. Chan K. H., Wong S. Y., Li X., Zhang Y. Z., Lim P. C., Kotaki M., He C. B. (2009). Effect of molecular orientation on mechanical property of single electrospun fiber of poly[(R)-3-hyroxybutyrate-co-(R)-3-hydroxyvalerate]. *J. Phys. Chem. B.*, 113, 13179-13185.

62. Catalani L. H., Collins G., Jaffe M. (2006). Evidence for Molecular Orientation and Residual Charge in the Electrospinning of Poly(butylene terephthalate) Nanofibers. *Macromolecules*, 40, 1693-1697.

63. Won S. W., Jo S. M., Lee W. S., Kim Y. R. (2003). An Electrospun Poly(vinylidene fluoride) Nanofibrous Membrane and Its Battery Applications. *Adv. Mat.*, 15, 2027-2032.

64. Tong H. W., Wang M. (2010). An investigation into the influence of electrospinning parameters on the diameter and alignment of poly(hydoxybutyrate-co-hydroxyvalerate) fibers. *J Appl. Polym. Sci.*, DOI: 10.1002/app.33302.

65. Cui W., Li X., Zhou S., Weng J. (2007). Investigation on Process Parameters of Electrospinning System through Orthogonal Experimental Design. *J Appl. Polym. Sci.*, 103, 3105-3112.

66. Costa L. M. M., Bretas R. E. S., Gregorio R. (2010). Effect of Solution Concentration on the Electrospray/Electrospinning Transition and on the Crystalline Phase of PVDF. *Mater. Sci. and Appl.*, 1, 247-252.

67. Kim J. S., Reneker D. H. (1999). Polybenzimidazole Nanofiber Produced by Electrospinning. *Polym. Eng. Sci.*, 39, 849-854.

68. Edwards M. D., Mitchell G. R., Mohan S. D., Olley R. H. (2010). Development of orientation during electrospinning of fibers of poly(ε-caprolactone). *European Polym. J.*, 46, 1175-1183.

69. Lee K. H., Kim K. W., Pesapane A., Kim H. K., Rabolt J. F. (2008). Polarized FT-IR Study of Macroscopically Oriented Electrospun Nylon-6 Nanofibers. *Macromolecules*, 41, 1494-1498.

70. Kameoka J., Craighead H. G. (2003). Fabrication of oriented polymeric nanofibers on planar surfaces by electrospinning. *Appl. Phys. Lett.*, 83, 371-373.

71. Sundaray B., Subramanian V., Natarajan T. S., Xiang R. Z., Chang C. C., Fann W. S. (2004). Electrospinning of continuous aligned polymer fibers. *Appl. Phys. Lett.*, 84, 1222-1224.

72. Kimura N., Kim H. K., Kim B. S., Lee K. H., Kim I. S. (2010). Molecular Orientation and Crystalline Structure of Aligned Electrospun Nylon-6 Nanofibers: Effect of Gap Size. *Macromolecular Mater. Eng.*, 295, 1090-1096.

73. Theron A., Zussman E., Yarin A. L. (2001). Electrostatic field-assisted alignment of electrospun nanofibers. *Nanotechnology*,12, 384-390.

74. Zussman E., Theron A., Yarin A. L. (2003). Formation of nanofiber crossbars in electrospinning. *Appl. Phys. Lett.*, 82, 973-975.

75. Konghklang T., Tashiro K., Kotaki M., Chirachanchai S. (2008). Electrospinning as a New Technique to Control the Crystal Morphology and Molecular Orientation of Polyoxymethylene Nanofibers. *J. Am. Chem. Soc.*, 130, 15460-15466.

76. Liu, S. T., Long, D. (1992). Pyroelectric Detectors and Materials. In *Key Papers in Physics*, Rosen C. Z., Hiremath B. V., Newnham R. (Eds.), American Institute of Physics: New York.

77. Tashiro, K., Kobayashi, M. (1986). Structural Study of the Ferroelectric Phase Transition of vinylidene fluoride-trifluoroethylene copolymers: 4. Poling Effect on Structural and Phase Transition. *Polym.*, 27, 667-676.

78. Gerliczy, G., Betz, R. (1987). Solef PVDF Biaxially Oriented Piezo- and Pyro-Electric Films for Transducers. *Sensors and Actuators*, 12, 207-223.

79. Yoon S., Prabu A. A., Ramasundaram S., Kim K. J. (2008). PVDF nanoweb touch sensors prepared using electrospinning process for smart apparels applications. *Adv. Sci. Technol.*, 60, 52-57.

80. Chang C., Tran V. H., Wang J., Fuh Y., Lin L. (2010). Direct-write piezoelectric polymeric nanogenerator with high energy conversion efficiency. *Nano Lett.*, 10, 726-731.

81. Pu J., Yan X., Jiang Y., Chang C., Lin L. (2010). Piezoelectric actuation of direct-write electrospun fibers. *Sensors and Actuators A*, 164, 131-136.

82. Weber N., Lee Y. S., Shammugasundaram S., Jaffe M., Arinzeh T. L. (2010). Characterization and in vitro cytocompatiliblity of piezoelectric electrospun scaffolds. *Acta Biomater.*, 6, 3550-3556.

83. Chen H. C., Tsai C. H., Yang M. C. (2010). Mechanical properties and biocompatibility of electrospun polylactide/poly(vinylidene fluoride) mats. *J. Polym. Res.*, DOI: 10.1007/s10965-010-9421-5.

84. Park S. H., Kim J. U., Lee S. Y., Lee J. K., Kim M. R. (2008). Dye-sensitized solar cells using polymer electrolytes based on poly(vinylidene fluoride-hexafluoro propylene) nanofibers by electrospinning method. *J. Nanosci. Nanotechnol.*, 8, 4889-4894.

85. Priya A. R. S., Subramania A., Jung Y. S., Kim K. J. (2008). High performance quasi-solid-state dye-sensitized solar cell based on electrospun PVDF-HFP membrane electrolyte. *Langmuir*, 24, 9816-9819.

86. Choi S. S., Lee Y. S., Joo C. W., Lee S. G. Park J. K., Han K. S. (2004). Electrospun PVDF nanofiber web as polymer electrolyte or separator. *Electrochemica Acta*, 50, 339-343.

87. Kim, J. R., Choi S. W., Jo S. M., Lee W. S. Kim B. C. (2004). Electrospun PVDF-based fibrous polymer electrolytes for lithium ion polymer batteries. *Electrochemica Acta*, 50, 69-75.

88. Ding Y., Zhang P., Long Z., Jiang Y., Xu F., Di W. (2008). Preparation of PVDF-based electrospun membranes and their applications as separators. *Sci. Technol. Adv. Mater.*, 9, 1-4.

89. Park S. H., Lee S. M., Lim H. S., Han J. T., Lee D. R., Shin H. S., Jeong Y. Kim J., Cho J. H. (2010). Robust Superhydrophobic Mats based on electrospun Crystalline Nanofibers Combined with a Silane Precursor. *ACS Appl. Mater. Interfaces*, 2, 658-662.

90. Chen Y., Kim H. (2009). Preparation of superhydrophobic membranes by electrospinning of fluorinated silane functionalized poly(vinylidene fluoride). *Appl. Surface Sci.*, 255, 7073-7077.

91. Gopal R., Kaur S., Ma Z., Chan C., Ramakrishna S., Matsuura T. (2006). Electrospun nanofibrous filtration membrane. *Appl. Surface Sci.*, 281, 1, 581-586.

92. Yuan J., Geng J., Xing Z., Shen J., Kan I. K., Byun H. (2010). Electrospinning of antibacterial poly(vinylidene fluoride) nanofibers containing silver particles. *J. Appl. Polym. Sci.*, 116, 668-672.

93. Hattori T., Watanabe T., Akama S., Hikosaka M., Ohigashi H. (1997). The high-pressure crystallization behaviors and piezoelectricity of extended chain lamellar crystals of vinylidene fluoride trifluoroethylene copolymers with high molar content of vinylidene fluoride. *Polym.*, 38, 3505-3511.

94. Hikosaka M. (1990). Unified theory of nucleation of folded-chain crystals (FCC) and extended-chain crystal s (ECC) of linear polymers: 2. Origin of FCC and ECC. *Polym*., 31, 458-468.

95. Salalha W., Dror Y., Khalfin R. L., Cohen Y., Yarin A. L., Zussman E. (2004). Single-Walled Carbon Nanotubes Embedded in Oriented Polymeric Nanofibers by Electrospinning. *Langmuir*, 20, 9852-9855.

96. Dror Y., Salalha W., Khalfin R. L., Cohen Y., Yarin A. L., Zussman E. (2003). Carbon Nanotubes Embedded in Oriented Polymer Nanofibers by Electrospinning. *Langmuir*, 19, 7012-7020.

97. Chua Y. C., Lu X. (2007). Polymorphism Behavior of Poly(ethylene naphthalate)/Clay Nanocomposites: The Role of Clay Surface Modification", *Langmuir*, 23, 1701-1710.

98. Owens F. J., Jayakody J. P. R., Greenbaum S. G. (2006). Characterization of single walled carbon nanotubes: Polyvinylidene difluoride composites, *Compos. Sci. Technol.*, 66, 1280-1284.

99. Pan C., Ge L.Q., Gu Z. Z. (2007). Fabrication of multi-walled carbon nanotube reinforced polyelectrolyte hollow nanofibers by electrospinning, *Compos. Sci. Technol.*, 67, 3271-3277.

100. Feng W., Wu Z., Li Y., Feng Y., Yuan X. (2008). The fabrication and electrochemical properties of electrospun nanofibers of a multiwalled carbon nanotube grafted by chitosan. *Nanotechnology*, 19, 105707.

101. Corio P., Jorio A., Demir N., Dresselhaus M. S. (2004). Spectro-electrochemical studies of single wall carbon nanotubes films. *Chem. Phys. Lett.*, 392, 396-402.

102. Mcgriffin, G. L. (2004). In: Heffman, E. Editor. Chromatography 6th Edition. Netherlands. Elsevier B. V.; [Chapter 1].

103. Huang S., Yee W. A., Tjiu W. C., Liu Y., Kotaki M., Boey Y. C., Ma J., Liu T., Lu X. (2008). Electrospinning of Polyvinylidene Difluoride with Carbon Nanotubes: Synergistic Effects of Extensional Force and Interfacial Interaction on Crystalline Structures. *Langmuir*, 24, 13621-13626.

104. Yee W. A., Nguyen A. C., Lee P. S., Kotaki M., Liu Y., Tan B. T., Mhaisalkar S., Lu X. (2008). Stress-induced structural changes in electrospun polyvinylidene difluoride nanofibers collected using a modified rotating disk. *Polym.*, 49, 4196-4203.

105. Chen G. X., Li Y., Shimizu H. (2007). Ultrahigh-shear processing for the preparation of polymer/carbon nanotube composites. *Carbon*, 45, 2334-2340.

106. Yu S., Zheng W., Yu W., Zhang Y., Jiang Q., Zhao Z. (2009). Formation Mechanism of β-phase in PVDF/CNT Composite Prepared by the Sonication Method. *Macromolecules*, 42, 8870-8874.

107. Xie J., Xue Q., Chen H., Keller A., Dong M. (2010). Different factors' effect on the SWT-fluorocarbon resin interaction: A MD simulation study. *Computational Mater. Sci.*, 49, 148-157.

108. Pulikkathara M. X., Kuznetsov O. V., Peratla I. R. G., Wei X., Khanashesku V. N. (2010). Medium density polyethylene composites with functionalized carbon nanotubes. *Nanotechnology*, 19, 195603.

109. Noyori R. (1999). Supercritical fluids: Introduction. *Chem. Rev.*, 99, 353-354.

110. Nalawade S. P., Picchioni F., Janssen L. P. B. M. (2006). Supercritical carbon dioxide as a green solvent for processing of polymer melts: processing aspects and applications. *Prog. Mater. Sci.*, 31, 19-43.

111. Shieh Y. T., Hsiao T. Y., Chang S. K. (2006). CO_2 pressure effects on melting, crystallization, and morphology of poly(vinylidene fluoride). *Polym.*, 47, 5929-5937.

112. Kiran E. Polymer miscibility, phase separation, morphological modifications and polymorphic transformation in dense fluids. *J Supercritical Fluids*, 47, 466-483.

113. Ma W. M., Yu J., He J. S. Competitive influence of atactic polystyrene and supercritical carbon dioxide on the conformation of syndiotactic polystyrene. *J. Polym. Sci*: *Part B*:*Polym., Phys.*, 45, 1755-1764.

114. Na H., Zhao Y., Zhao C., Zhao C., Yuan X. (2008). Effect of hot-press on electrospun poly(vinylidene fluoride) membranes. *Polym. Eng. Sci.*, 48, 934-940.

115. Siripurapu, S., DeSimone, J. M., Khan, S. A., & Spontak, R. J. (2004). Low temperature, surface-mediated foaming of polymer films. *Adv. Mater.*, 16, 989-994.

116. Tokuda H., Tsuzuki S., Susan M. A. B. H., Hayamizu K., Watanabe M. (2006). How Ionic are Room-Temperature Ionic Liquids? An Indicator of the Physiochemical Properties. *J. Phys. Chem.*, 110, 19593-19600.

117. Yee W. A., Xiong S., Ding G., Nguyen A. C., Lee P. S., Ma J., Kotaki M., Liu Y., Lu X. (2010). Super Critical Carbon Dioxide-Treated Electrospun Poly(vinylidene fluoride) Nanofibrous Membranes: Morphology, Structures and Properties as an Ionic Liquid Host. *Macromol. Rapid Commun.*, 31, 1779-1784.

Appendix

A. List of publications resulting from this work

1. Yee W. A., Nguyen A. C., Lee P.S., Kotaki M., Liu Y., Tan B. T., Mhaisalkar S., Lu X. (2008). Stress-induced structural changes in electrospun polyvinylidene difluoride nanofibers collected using a modified rotating disk. *Polym.*, 49, 4196-4203.
2. Huang S.[*], Yee W. A.[*], Tjiu W. C., Liu Y., Kotaki M., Boey Y. C. F., Ma J., Liu T., Lu X. (2008). Electrospinning of Polyvinylidene Difluoride with Carbon Nanotubes: Synergistic Effects of Extensional Force and Interfacial Interaction on Crystalline Structures. *Langmuir.*, 24, 13621-13626.
3. Yee W. A., Xiong S., Ding G., Nguyen A. C., Lee P. S., Ma J., Kotaki M., Liu Y., Lu X. (2010). Supercritical Carbon Dioxide-Treated Electrospun Poly(vinylidene fluoride) Nanofibrous Membranes: Morphology, Structures and Properties as an Ionic-Liquid Host. *Macromol. Rapid Commun.*, 31, 1779-1784. [This work was accepted as the cover page of the journal. DOI: 10.1002/marc.201000201].
4. Tao P., Yee W. A., Xu J., Toh C. L., Ma J., Lu X. (2011). Thermal Stability of Ionic-Liquid/Poly(vinylidene fluoride) Electrolytes and their Influence on the Performance of Electrochromic Devices. *J. Membrane Sci.*, 376, 283-289.
5. Yee W. A., Tao P., Zhang C., Kong J., Kotaki M., Liu Y., Liu T., Lu X. (2011). Effects of Functional Groups in Electrospinning of Poly(vinylidene fluoride) with Carbon Nanotubes on Intefacial Interaction affecting Crystalline Structures. [In preparation for submission].
6. Yee W.A. (2010). Supercritical Carbon Dioxide Treatment of Electrospun PVDF Nano-fibrous Membranes for Electrochemical Applications. In: *Proceedings of the 43rd IUPAC World Polymer Congress (MACRO2010)*, Glasgow, UK, 11-16 July 2010.

** denotes equal contribution to this work.*